GDAŃSK UNIVERSITY OF TECHNOLOGY

FACULTY OF APPLIED PHYSICS AND MATHEMATICS

Student's name and surname: Akash Ghosal
ID: 191925
Cycle of studies: postgraduate
Mode of study: Full-time studies
Field of study: Nanotechnology
Specialization: Nanostructures and computer simulations in material science

MASTER'S THESIS

Title of thesis: Tailoring the exsolution of Fe-containing nanoparticles from the La and Ce co-doped strontium titanates

Title of thesis (in Polish): Optymalizacja procesu wydzielania nanocząstek zawierających Fe z tytanianów strontudomieszkowanych La i Ce

Supervisor: dr hab. inż. Beata Bochentyn

GDAŃSK UNIVERSITY OF TECHNOLOGY | FACULTY OF APPLIED PHYSICS AND MATHEMATICS

DECLARATION regarding the diploma thesis titled:
Tailoring the exsolution of Fe-containing nanoparticles from the La and Ce co-doped strontium titanates

First name and surname of student: Akash Ghosal
Date and place of birth: 09.02.1996, Kalyani
ID: 191925
Faculty: Faculty of Applied Physics and Mathematics
Field of study: nanotechnology
Cycle of studies: postgraduate
Mode of study: Full-time studies
Type of the diploma thesis: master's thesis

Aware of criminal liability for violations of the Act of 4th February 1994 on Copyright and Related Rights (Journal of Laws 2021, item 1062 with later amendments) and disciplinary actions set out in the Act of 20th July 2018 on the Law on Higher Education and Science (Journal of Laws 2022 item 574 with later amendments),[1] as well as civil liability, I hereby declare that the submitted diploma thesis is my own work.

This diploma thesis has never before been the basis of an official procedure associated with the awarding of a professional title.

All the information contained in the above diploma thesis which is derived from written and electronic sources is documented in a list of relevant literature in accordance with art. 34 of the Copyright and Related Rights Act.

31.10.2023, Akash Ghosal

Date and signature of the student or authentication on the university portal My GUT

**) The document was drawn up in the IT system, on the basis of paragraph 15 clause 3b of the Decree of the Ministry of Science and Higher Education of 12 May 2020, amending the decree concerning university studies (Journal of Laws of 2020, item 853). No signature or stamp required.*

[1] The Act of 20th July 2018 on the Law on Higher Education and Science:

Art. 312, section 3. Should a student be suspected of committing an act referred to in Art. 287 section 2 items 1–5, the rector shall forthwith order an enquiry.

Art. 312, section 4. If the evidence collected during an enquiry confirms that the act referred to in section 5 has been committed, the rector shall suspend the procedure for the awarding of a professional title pending a judgement of the disciplinary committee and submit formal notification on suspicion of committing a criminal offence.

Streszczenie

Eksolucja jest jedną z metod wytwarzania nanocząstek metali bądź stopów na powierzchni ziaren materiałów ceramicznych w celu zwiększania ich aktywności katalitycznej. Polega ona na migracji atomów z sieci krystalicznej na powierzchnię ziarna dzięki odpowiednim warunkom procesu (np. temperatura, atmosfera redukująca, pole elektryczne lub naprężenia).

W pracy podjęto próbę wytworzenia drogą eksolucji nanocząstek żelaza lub stopów zawierających żelazo ze zdefektowanej struktury domieszkowanego tytanianiu strontu. O ile w literaturze dobrze opisana jest eksolucja takich metali jak Ni, Co, Cu, Pt czy Pt, o tyle brakuje doniesień o eksolucji żelaza. Głównym celem pracy magisterskiej było wytworzenie nowych, aktywnych katalitycznie materiałów z grupy tytanianów strontu domieszkowanych La i Ce z wydzielonymi nanocząstkami żelaza lub jego stopów. Materiały te mogłyby znaleźć potencjalne zastosowanie jako anody w tlenkowych ogniwach paliwowych typu SOFC. Wytworzone związki zostały zbadane pod kątem stabilności strukturalnej w celu określenia optymalnej ilości domieszki Fe do podsieci B perowskitu. Następnie wytworzono serię materiałów, w których oprócz ustalonej zawartości Fe wprowadzano również drugą domieszkę - Ni lub Co.

Na koniec przeprowadzono krytyczną analizę wyników XRD i SEM dla wszystkich zredukowanych proszków, aby zbadać mechanizm wydzielania w tych materiałach, ich stabilność strukturalną i charakterystykę uwolnionych nanocząstek.

Słowa kluczowe: Ekskstruzja, Ogniwa paliwowe o stałym elektrolicie, Materiały katalizatorowe, Materiały anodowe, Elektrokataliza, Nanocząstki metalu

Abstract

Exsolution is one of the methods of producing metal or alloy nanoparticles on the surface of grains of ceramic materials in order to increase their catalytic activity. It involves the migration of atoms from the crystal lattice to the grain surface and formation of nanoparticles thanks to appropriate process conditions (e.g. temperature, reducing atmosphere, electric field or stress).

In this work, an attempt was made to produce iron nanoparticles or iron-containing alloys from a defective structure of doped strontium titanate via exsolution process. While the exsolution of metals such as Ni, Co, Cu, Pt and Pt is well described in the literature, there is lack of reports on the exsolution of iron. The main goal of the master's thesis was to fabricate new, catalytically active materials from the group of strontium titanates doped with La and Ce decorated with nanoparticles of iron or its alloys. These materials could be potentially used as anodes in Solid Oxide Fuel Cells. The produced compounds were examined for structural stability in order to determine the optimal amount of Fe doping into the B sublattice of the perovskite. Then, a series of materials was produced in which, in addition to the fixed Fe content, a second admixture - Ni or Co - was also introduced.

Finally, a critical analysis of the XRD and SEM results was performed for all reduced powders to investigate the exsolution mechanism in these materials, their structural stability, and the characteristics of the formed nanoparticles.

Keywords : Exsolution, Solid oxide fuel cells, Catalyst Materials, Anode Materials, Electro-catalysis, Metal Nanoparticles

Acknowledgments

I would like to express my heartfelt gratitude to my dedicated supervisor, Dr. hab. Beata Bochentyn, for her unwavering support, guidance, and expertise throughout the research work and writing of my master's thesis. Her invaluable mentorship and insightful feedback have been instrumental in shaping the direction and quality of this work.

I would also like to extend my appreciation to the faculty members and staff of the Gdansk University of Technology, specifically within the Faculty of Applied Physics and Mathematics. The academic environment and resources provided by the university have been crucial in facilitating my research endeavors.

Furthermore, I would like to acknowledge the encouragement and understanding I received from my family and friends during the course of my studies. Their support and belief in my abilities have been a constant source of motivation.

Finally, I am grateful for the opportunity to pursue my master's degree in Nanotechnology and for the knowledge and experiences gained during this academic journey.

Akash Ghosal

CONTENTS

List of Abbreviations……..……..... 8

List of Figures ……...……..…… 9

List of Tables ……..…… 10

1. Introduction ……..……..…… 12

1.1. Overview ……..……..…… 12

1.2. Background ……..……..…… 13

1.2.1. Solid Oxide Fuel Cell ……..……..… 13

1.2.2. Exsolution ……..……..…….. 14

1.3. Purpose and Research Question ……..……..…….. 15

2. Theoretical Background ……..……..……..…. 18

2.1. Growth mechanism of exsolution ……..……..…… 18

2.2. Strategies for highly efficient exsolution ……..……..…… 18

2.3. Important features associated with metal exsolution ……..…… 20

2.4. Properties of exsolved particles ……..……..…… 24

3. Experimental ……..……..…… 26

3.1. Synthesis of Powders ……..…… 26

3.2. Materials Characterisation ……..……. 28

3.3. Experimental Characterisation Techniques ……..…..…… 28

3.3.1. X-Ray Diffraction……..……..… 28

a) Rietveld Refinement ……..……. 30

b) Scherrer Equation ……..……..…….. 31

3.3.2. Scanning Electron Microscope ……..…… 31

4. Results and Discussion …….… …… 34

4.1. Exsolution of Fe metallic NPs ……..……. …….. 34

4.1.1. XRD …….. 34

4.1.2. SEM …….. 43

4.2. Exsolution of Alloy nanoparticles ..……..…….. 47

4.2.1. Tailoring the catalytic activity of exsolved Fe NPs with Ni/Co ……...… 47

4.2.2. Synthesis of Powders …..……..…… 48

4.2.3. Phase evolution of perovskite oxides……..….. 49

4.2.4. Morphology of the exsolved nanoparticles……..…. 53

5. Current challenges faced today in research of exsolution …….…… 56
5.1. Effective methods for exsolution …….…….. 56
5.2. Preferred site for exsolution …….…….. 57
5.3. Exsolution product complexity …….……. 57
5.4. Investigation of the exsolution process …….……. 57
6. Conclusion …….……..….. 58
7. References …….…… 59
8. Appendix I …….……..……..… 64
9. Appendix II …….……..…..……..….. 65

List of Abbreviations

A-LSC	A-site deficiency Lanthanum Strontium Cerium
BSE	Backscattered electrons
DI	Deionised
DFT	Density Functional Theory
DIR-SOFCs	Direct Internal Reforming Solid Oxide Fuel Cells
EDS	Energy Dispersive X-Ray Spectroscopy
EIS	Electrochemical Impedance Spectroscopy
LSCFeT	$La_{0.27}Sr_{0.54}Ce_{0.09}Fe_xTi_{1-x}O_{3-\delta}$ (Lanthanum Strontium Cerium Iron Titanium with Oxygen deficiency)
LSCFeNiT	$La_{0.27}Sr_{0.54}Ce_{0.09}Fe_xNi_yTi_{1-x-y}O_{3-\delta}$ (Lanthanum Strontium Cerium Iron Nickel Titanium with Oxygen deficiency)
LSCFeCoT	$La_{0.27}Sr_{0.54}Ce_{0.09}Fe_xCo_yTi_{1-x-y}O_{3-\delta}$ (Lanthanum Strontium Cerium Iron Cobalt Titanium with Oxygen deficiency)
LSCF	Lanthanum Strontium Cerium Iron
LSCT	Lanthanum Strontium Cerium Titanium
NC	Nano-catalyst
NPs	Nano-particles
SD	Standard deviation
SE	Secondary electrons
SEM	Scanning electron microscopy
SMSI	Strong metal support interaction
SOECs	Solid oxide electrolysis cells
STEM	Scanning transmission electron microscopy
TEM	Transmission electron microscopy
TGA	Thermogravimetric analysis
TPB	Triple phase boundary
XPS	X-Ray photoelectron spectroscopy
XRD	X-Ray diffraction

List of Figures

1. *Fig 1.1.1 : Atmospheric CO_2 concentration (ppm) over year …… 12*
2. *Fig 1.2.1 : Concept diagram of SOFC based on oxygen ion conductor …… 13*
3. *Fig 1.2.2 : Schematic of exsolution process …… 15*
4. *Fig 1.2.3 : Schematic of self-regeneration feasibility of exsolved metal NPs …… 16*
5. *Fig 1.2.4 : (Above) Growing number of papers and citations that were searched in the Web of Science with exsolution-related keywords; (Below) Statistical analysis of the papers published for bimetallic exsolution …… 17*
6. *Fig 2.3.1 : Unit cells of perovskites…… 20*
7. *Fig 3.1.1 : Schematic plot of calcination temperature profile …… 27*
8. *Fig 3.1.2. : Schematic of Pechini type sol-gel method of material preparation …… 27*
9. *Fig 3.1.3 : Material after calcination (solid network like structure) …… 27*
10. *Fig 3.1.4 : $LSCFe_xT_{1-x}O_{3-\delta}$ powders after sintering, (Left) x=0.1 (Middle) x=0.18 (Right) x=0.25 …… 28*
11. *Fig 3.3.1 : Geometrical condition for diffraction from lattice planes …… 29*
12. *Fig 3.3.2 : Diffraction peak and information content that can be extracted …… 30*
13. *Fig 3.3.3 : Schematic of Scanning Electron Microscope (SEM) …… 31*
14. *Fig 3.3.4 : Different types of signals generated depending on the electrons' penetration depth …… 32*
15. *Fig 4.1.1 : XRD patterns of the as-prepared LSCFeT powders …… 34*
16. *Fig 4.1.2 : Phase composition from XRD measurement before reduction …… 35*
17. *Fig 4.1.3 : Crystal structure of (left) $SrTiO_3$ and (right) $Sr_{0.9}La_{0.1}TiO_3$, - model generated in Vesta software … 35*
18. *Fig 4.1.4 : XRD patterns of the reduced LSCFeT powders …… 36*
19. *Fig 4.1.5 : Phase composition from XRD measurement after reduction …… 36*
20. *Fig 4.1.6 : Comparison of the most intensive XRD peak in results of as-prepared materials …… 37*
21. *Fig 4.1.7 : Comparison of the most intensive XRD peak in results of materials after reduction …… 37*
22. *Fig 4.1.8 : Lattice parameter of main $SrTiO_3$-like dominant phases present in LSCFeT materials, before and after the reduction …… 40*
23. *Fig 4.1.9 : Crystallographic structure of $LSCFe_xT_{1-x}O_{3-\delta}$, (left) before reduction and (right) after reduction … 41*
24. *Fig 4.1.10 : SEM images of LSCFeT powders reduced at 900 °C in dry H_2 for 10hours …… 43*
25. *Fig 4.1.11. : Exsolved Fe NPs sizes in LSCFeT powders reduced at 900 °C in dry H_2 for 10hours …… 44*
26. *Fig 4.1.12 : Agglomeration of exsolved Fe NPs in $LSCFe_{0.25}T_{0.75}O_{3-\delta}$ …… 45*
27. *Fig 4.1.13 : Particle size distribution of exsolved Fe NPs of $LSCFe_xT_{1-x}O_{3-\delta}$ …… 45*
28. *Fig 4.2.1 : Photos of as-prepared LSCFeT-based powders containing Ni (left) and Co (right) as a second metal dopant …… 48*
29. *Fig 4.2.2 : XRD patterns of the as-prepared LSCFeT-based powders with additional metal dopants …… 49*
30. *Fig 4.2.3 : XRD patterns of the reduced LSCFeT-based powders with additional metal dopants …… 50*
31. *Fig 4.2.4 : Comparison of the most intensive XRD peaks in results of materials after reduction, (left) LSCFeNiT, (right) LSCFeCoT …… 51*
32. *Fig 4.2.5 : SEM images of LSCFeNiT anode powders reduced at 900 °C in dry H_2 for 10hours …… 53*
33. *Fig 4.2.6 : SEM images of LSCFeCoT anode powders reduced at 900 °C in dry H_2 for 10hours …… 54*
34. *Fig 5.0.1 : Current challenges for exsolution …… 56*

List of Tables

1. *Table 3.1.1 : Stoichiometric composition of $La_{0.27}Sr_{0.54}Ce_{0.09}Fe_xT_{1-x}O_{3-\delta}$ ($LSCFe_xT_{1-x}O_{3-\delta}$) …… 26*
2. *Table 4.1.1 : Unit cell parameters of LSCFeT …… 39*
3. *Table 4.1.2 : Crystallite size and lattice strain values calculated using the Scherrer Equation for LSCFeT …… 42*
4. *Table 4.2.1 : Series of Anode Powders composition …… 47*
5. *Table 4.2.2 : Unit cell parameters of LSCFeT-based powders with additional metal dopants with Rietveld refinement parameters …… 51*

This page is intentionally kept blank

1. Introduction

1.1 Overview

Over the past 50 years, the world's energy consumption and environmental impact have significantly increased due to population expansion, urbanisation, and a rise in living standards. Future predictions also assume a rise in energy consumption, which would exacerbate already severe environmental issues. In fact, a sharp increase of atmospheric CO_2 levels (Fig. 1.1.1) influences global warming, endangering human life with significant climate change, including a decline in glaciers, sea ice, and permanent soil layers and an increase in extreme weather events including heat waves, droughts, storms, and typhoons. During the past century, global surface temperatures have increased at a rate near 0.6°C/century [1]. Our society is in need of a rapid sustainable clean energy transition. As one of the most efficient and practical answers to the environmental issues that we now face, fuel cells are a hot topic in the news today. The fact that CO_2 emissions from sewage are to blame for global warming is now well accepted. In addition to global warming, issues with energy supply and consumption also affect other environmental issues such air pollution, acid rain, ozone depletion, forest loss, and radioactive material emissions. For changing the world's energy supply towards sustainable resources, storage capabilities are required to buffer the irregular occurrence of renewable energy. Storing energy chemically as hydrocarbons is a very attractive option, since it could make use of large parts of the existing distribution infrastructure [2]. The world has reached alarming levels of greenhouse gases, the main contributors to climate change. In 2015, the world's top countries gathered in the city of Paris to sign the Climate Agreement. It was agreed that the global response to the growing threat of climate change should shift to sustainable energy use to limit the increase in global average temperature to well below 2°C above pre-industrial levels [3]. The main causes of the increase in greenhouse gases include power generation and transportation. There is a rapid shift to renewable energy generation and use as it helps address the global problem of climate change.

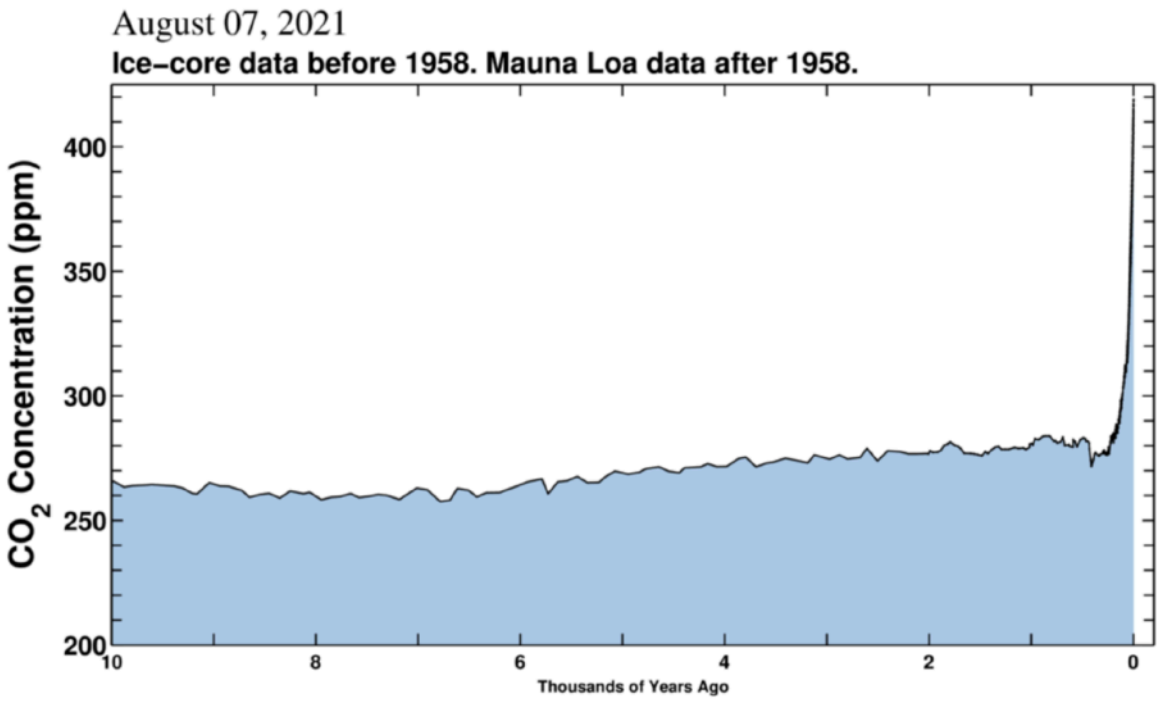

Fig. 1.1.1 Atmospheric CO_2 concentration (ppm) over year [4]

Nowadays, more and more effort is being put into environmentally friendly and sustainable energy sources. Widely examined Direct Internal Reforming Solid Oxide Fuel Cells (DIR-SOFCs) are promising candidates when it comes to harvesting electricity for industry, public buildings, and private housing [5]. Heterogeneous catalysis can be crucial in building an effective and suitable system to maximise the exploitation of existing resources, even though the basic answer for many energy and environmental concerns remains elusive [6]. The temperature of transformation and waste may be decreased, and the reaction's selectivity can be raised, by utilising catalytic reagents. In this context, supported metal nano-catalysts (NC) have been highlighted for their significance in a number of catalyst applications due to the special qualities derived from their size, shape, and composition [6]. By immobilising high-surface-area particles with supporting materials during design, it is crucial to ensure stability and catalytic activity. Many preparation processes, including thermal evaporation, pulsed laser deposition, chemical vapour deposition, electrochemical deposition, sol-gel/colloidal procedures, and impregnation methods, have been widely employed to create supported metal nano-catalysts. However, under working circumstances, the deposition of metal nanoparticles may result in agglomeration and coarsening, impairing performance fatally. As a possible alternative, an exsolution process has drawn a lot of interest.

1.2 Background

1.2.1 Solid Oxide Fuel Cell (SOFC)

A fuel cell (Fig. 1.2.1) is a device that converts chemical energy into electrical energy and heat through the electrochemical reaction of a fuel and an oxidant, without the need for direct combustion as an intermediate step, thus giving much higher conversion efficiencies than conventional thermo-mechanical methods. Since it is operated electrochemically and is not limited by the Carnot cycle, lower emissions such as NO_X or CO_2 are produced from fuel cells compared to the cleanest combustion process [7]. One of the most effective and environmentally beneficial technologies for producing electricity from hydrogen, natural gas, and other renewable fuels is the Solid Oxide Fuel Cell (SOFC). The application of fuel cell technologies to advanced power generation systems signifies the advancement in energy conservation and environmental protection for the next decade [8]. However, high operating temperatures of SOFC (800−1000 °C) results in high degradation and manufacturing costs, preventing large-scale commercialisation of this technology [9]. The operating principles of fuel cells are similar to those of batteries, i.e. electrochemical combination of reactants to generate electricity. The working principle is that, it can operate as long as both fuel and oxidant are supplied to the electrodes. The outcome of such working principle led by SOFCs exerts negligible influence on surrounding environment.

Fuel cells are generally classified according to the chemical characteristics of the electrolyte that is being used as the ionic conductor inside the cell. They are able to produce electricity and heat as byproduct as long as fuel is supplied to it. The system consists of two electrodes - a negative electrode i.e anode, and a positive electrode i.e cathode, sandwiched together around a gas-tight ceramic electrolyte, such as the remarkable ceramic material stabilised zirconia.

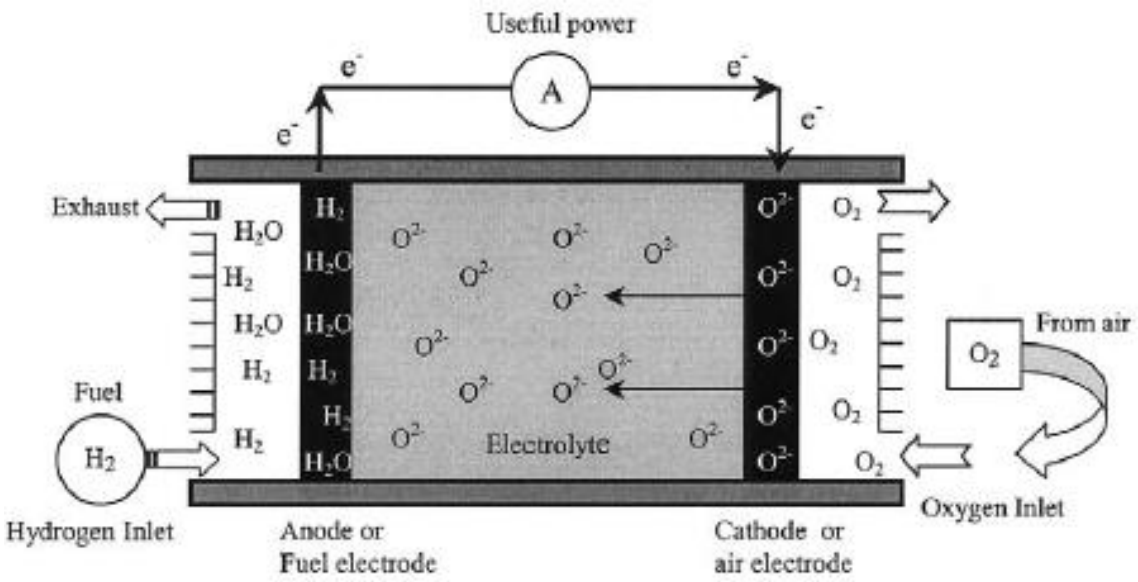

Fig. 1.2.1 Concept diagram of SOFC based on oxygen ion conductor [10]

A fuel such as hydrogen or methane is fed on to the anode of the cell and oxygen from air is fed on to the cathode. On the anode side, an electrochemical oxidation of fuel takes place, whereas on the cathode side the oxidant is reduced to the oxygen ions form. When there is an electrical connection between the cathode and the anode, electrons can flow from the anode to the cathode, ensuring a continuous supply of oxygen ions (O^{2-}) to the electrolyte and a supply of oxygen ions from the cathode to the anode is maintained. The overall charge balance is adjusted so that usable electrical energy is produced from the combustion of fuel. This process results to a byproduct of pure water molecule (H_2O) and heat.

Reaction on the Anode side : $H_2 \longrightarrow 2H^+ + 2e^-$ ……. Eq. 1.2.1

Reaction on the Cathode side : $O_2 + 4e^- \longrightarrow 2O^{2-}$ ……. Eq. 1.2.2

The catalytic performance of these electrodes can be improved by adding a small amount of catalytic metal, or by decorating the ceramic electrodes with metals. This process can by done by solution-phase impregnation, where sintering of the metal catalyst is problematic, thus resulting to loss of catalytic activity. A potential solution to this problem is to grow metal catalyst from an oxide host, usually a perovskite type of oxide, which is done via ex-solution process.

1.2.2 EXSOLUTION

Exsolution is a novel technology (Fig. 1.2.2) for decorating metal catalyst particles onto ceramic materials, e.g anodes in the Solid Oxide Fuel Cells (SOFCs), to increase their catalytic activity in the cell [11]. The produced nanoparticles have a strong metal-support interaction (SMSI) owing to their well dispersed and “embedded” properties on the support oxide surface, which provides an advantageous feature for catalyst stability compared to the existing wet impregnation or vapour deposition method [12]. There is evidence that supported metal catalysts formed in this way exhibit high stability, which could help address

the sintering issue, and may also be less prone to forming carbon filaments when operating in fuels with lower H_2O:C ratios [13]. Madsen et al. appear to have been the first to apply this concept to an SOFC and to demonstrate that metal exsolution can lead to enhanced electrode performance. These researchers incorporated Ru into the lattice of Sr-doped $LaCrO_3$ ($La_{0.8}Sr_{0.2}Cr_{0.82}Ru_{0.18}O_{3-\delta}$) and used this material as an SOFC anode [14].

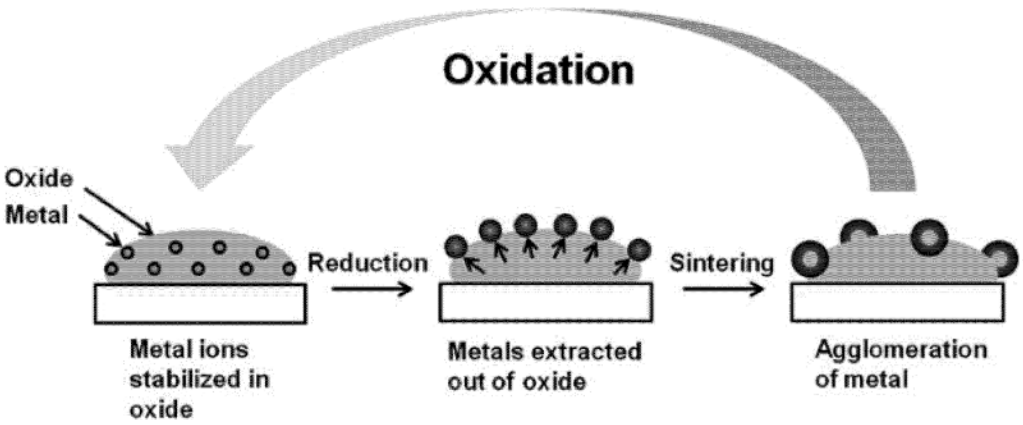

Fig. 1.2.2 Schematic of exsolution process [15]

In particular, nanoparticles produced by exsolution are entrenched on the oxide surface, thus even when carbon growth takes place in an operating environment including carbon species as a reactant, it happens as base growth as opposed to tip development. In base growth, more than a certain amount of carbon is no longer produced because the catalyst is settled on the supporting material as it is, whereas in tip growth, the catalyst is separated from the supporting material and agglomeration takes place, leading to deactivation. Since the exsolution takes place in a reducing environment, an oxygen vacancy generation in the perovskite oxides is thought to be the exsolution's primary driving factor. The segregation of B-site cations is necessary to preserve structural stability because the creation of oxygen vacancies disturbs the lattice stoichiometry. The formation of the oxygen vacancy has been influenced by a number of factors, including temperature, non-stoichiometry caused by an A-site defect, voltage biasing, strain, phase transition, and topotactic ion exchange [14].

Metal salts can be dissolved in a solution to add metallic catalyst particles, although these metal particles often become unstable. For instance, Lawrence Adijanto et al. [16] reported that, when Pd particles were added to LSCM-YSZ composites, the performance was initially excellent. However, the treatment was at 1173 K (900 °C), which is optimum for SOFC standards, and it significantly reduced the performance as a result of poor metal particles adhesion, which is why resulting in the loss of active surface area. In order to bring metals to the surface of these exsolution catalysts, strongly reducing conditions are frequently needed (for example, 1073 K in somewhat dry H_2 [13]). Given that treating the catalyst so severely might have an impact on other features, such as loss of support surface area, this need poses a possible barrier for many catalytic applications. Since the first study on emissions-control catalysis, there has been a significant amount of subsequent research, including work on using these exsolution systems to SOFCs and hydrocarbon-reforming catalysis. Numerous of those studies were exsolution process-focused, making them applicable to all applications.

Catalytically active metal particles are formed by the reduction of the perovskite-type oxides which is doped with reducible transition metals, such as Ni, Cu, Pt, Ag, Fe. After undergoing reduction, the transition metal exsolves out from the perovskite lattice and forms metallic deposits on the surface. This approach anchors the nanoparticles to the oxide, making them less prone to particle growth at elevated temperatures. Some studies even claim that such catalysts offer reversibility by re-dissolving the catalytically active material into the host-oxide upon an oxidative heat treatment [17]. The reversibility of the nanoparticle generation (Fig. 1.2.3) endows the catalyst redox-cycling stability and free from agglomeration through re-oxidation [6]. Since the release of catalytically active metals can also be triggered by an applied voltage, the use of release catalysts as electrodes in Solid Oxide Electrolysis cells (SOECs) adds another level of flexibility. By reducing the oxygen chemical potential inside the oxide electrode as a result of this electrochemical polarisation, the cathode material is reduced, which results in metal exsolution. Exsolution catalysts can be used in the subsequent stages of storing renewable energy, such as providing electricity to fuel processes, and they also present exciting potential for heterogeneous catalysis. The possibility of electro-chemically switching the activity or selectivity of the catalysts is extremely attractive, since it may offer fundamentally novel possibilities in fuel synthesis by simply adjusting the applied voltage [19].

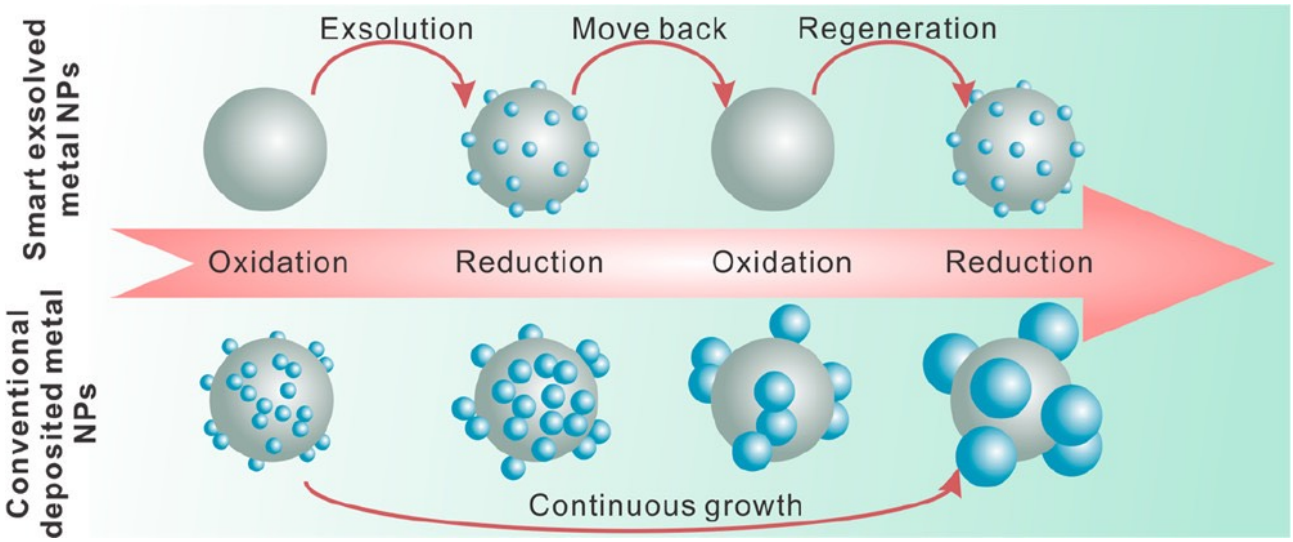

Fig. 1.2.3 Schematic of self-regeneration feasibility of exsolved metal NPs [18]

1.3 Purpose and Research Questions

The aim and purpose of this master's thesis is to evaluate a novel catalytic material as anode candidate for biogas fuelled DIR-SOFCs. A perovskite-type compound $SrTiO_3$ doped with La, Ce, and Fe of general formula $La_{0.27}Sr_{0.54}Ce_{0.09}Fe_xTi_{1-x}O_{3-\delta}$ (LSCFeT), where x equal to 0.1, 0.18 and 0.25, was synthesised using solid-state reaction method and reduced in H_2 for 10 hours to generate Fe NPs over the grain surface. These exsolved metallic NPs dispersed over the lattice surface should increase the electro-chemical activity of the ceramic anode materials. Such an improvement seems to be very beneficial, because many perovskite-type materials suffer from low electrical conductivity and/or poor electrochemical activity for oxidation of fuels, especially at intermediate temperature range (600–800 °C) [20]. Many of the previous research papers presented investigations of stoichiometrically simple perovskite with embedded

alloy nanoparticles of Ni, Cu, Co, cations since they can be easily exsolved. In this case, the focus is on Fe cation for exsolution, since it's problematic to do so. Therefore here, a perovskite with A-site deficiency (A/B<1) was developed, because the cations that are challenging to reduce under the same circumstances may be readily exsolved, as the A-site deficient perovskites can avoid A-site segregation by having a defect-free perovskite as exsolution moves forward [11]. There is special interest in oxide anodes, which are able to undergo the exsolution process of B-site cations, producing highly stable and electro-catalytically active NPs embedded in the perovskite [21]. Exsolution has further advantages for use in electrochemical devices due to its straightforward production technique and material adaptability to other metal oxides. The number of articles and citations linked to "exsolution" have grown significantly as a result of the recent interest in its use in these many applications (Fig. 1.2.4). This novel technology results in the increased performance of the exsolved particles while retaining the overall structural characteristics of the original support oxide because the majority of the doped metal cation is exsolved to the surface without leaving cation defects in the parent oxide lattice. Using the exsolution phenomena, the primary research goal of this master's thesis work is to fabricate reliable and stable compounds for energy conversion devices. This led to the investigation of a unique perovskite-type material (LSCFeT), which is a strong contender to serve as an extra anodic layer in SOFCs.

After successful determination of the best stable content of Fe in the material LSCFeT after reduction, new materials will be sintered with Ni and Co as the added dopants on the B - sub lattice with Fe_x respectively. The following materials are - $La_{0.27}Sr_{0.54}Ce_{0.09}Fe_xNi_yTi_{1-x-y}O_{3-\delta}$ (LSCFeNiT) , and $La_{0.27}Sr_{0.54}Ce_{0.09}Fe_xCo_yTi_{1-x-y}O_{3-\delta}$ (LSCFeCoT). Based on these ceramic materials, the feasibility and effectiveness of nanoparticle exsolution, both in the form of single metal and in the form of alloys, will be examined.

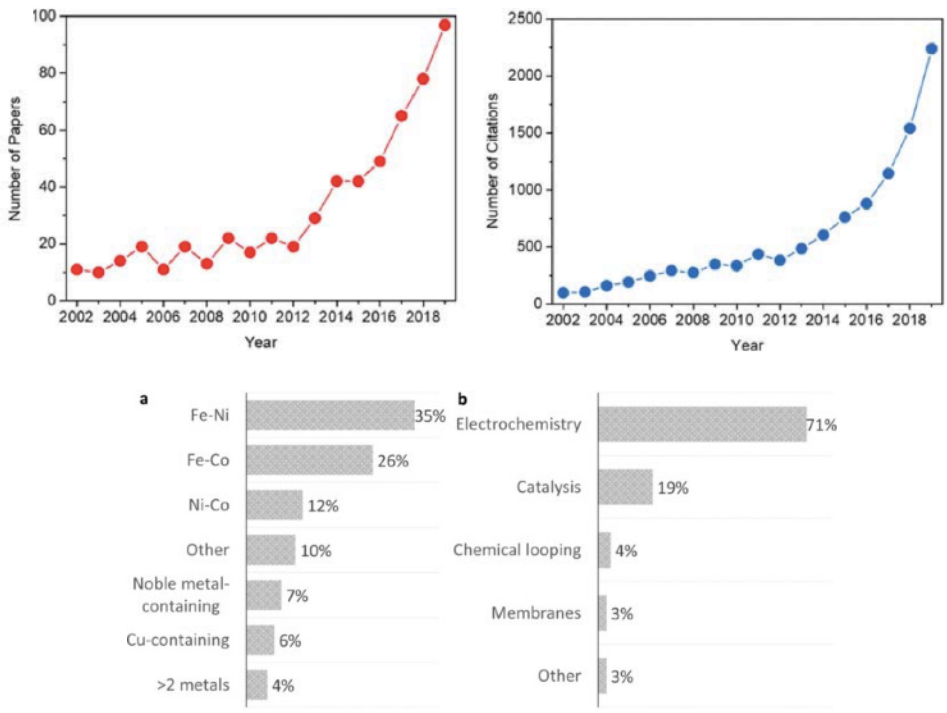

Fig. 1.2.4 (Above) Growing number of papers and citations that were searched in the Web of Science with exsolution-related keywords; (Below) Statistical analysis of the papers published for bimetallic exsolution [22]

2. Theoretical Background

2.1 Mechanism of exsolution

The exsolution mechanism is a very intricate process that involves nucleation, growth, diffusion, and reduction. Till date, significant attempts have been made to understand and describe this process at both the macroscopic and atomic levels. Two generally accepted hypotheses about the process of metal particle formation are that metal particles preferentially form in bulk and then migrate to the surface under the influence of strain in the matrix oxide, and that B-site cations diffuse directly from the bulk to the surface for nucleation [23]. Katz et al. [24] indicated that the reduction-treat process of Pt-doped $CaTiO_3$ films produced by epitaxial growth may be the initial exsolution mechanism. In their research work, the matrix perovskite shows evidence of Pt-rich cluster formation following reduction.

Exsolution often requires the reduction of the metal oxide (or metal ion) to the metallic state. The reason behind the cause for this is, according to thermodynamics, it is only possible to happen when the Gibbs free energy change ΔG (∑G product - ∑G reactant) is negative. Below 900 °C, the majority of metals (such as La, Ba, and Sr) remain stable under any reducing circumstances because the ΔG of their oxides is positive [25]. Whereas most of the 3d transition metals (such as Fe, Co, and Ni) have a negative value for ΔG, and therefore they may be reduced and exsolved more readily at temperatures over 600 °C. Notably, a greater temperature is needed for exsolving Fe from the matrix oxide compared to the reduction temperatures of Ni and Co. The volume-free energy and surface/interface energy (the surface energy of the newly created metal NPs and the interface energy between them and the matrix) are two factors that affect the change in Gibbs free energy throughout this process. The exsolved particle with the critical radius r' will arise when the critical free energy ΔG_n' is overcome [25]. The Gibbs free energy begins to decline as the particle radius exceeds r', which is advantageous for particle development. The free energy is impacted by the exsolution's volume change. The elastic energy diminishes and the particle's surface energy grows during the whole process of exsolving the particle from the matrix [23].

2.2 Strategies for highly efficient exsolution

Both the exterior environment (such as temperature and the reduction atmosphere) and the interior circumstances (such as A-site deficiency, B-site cation dopants, etc.) have been found to be effective ways to speed up the exsolution process.

2.2.1 External Environment

The exsolution process and the shape of exsolved NPs are most greatly influenced by the temperature of the external reducing environment. For instance, following reduction at 700 °C and 800 °C, Lai et al. [26] generated Co-Fe NPs on $La_{0.3}Sr_{0.7}Cr_{0.3}Fe_{0.6}Co_{0.1}O_{3-\delta}$ and discovered that the particle growth rate and sample size (700 °C) were both lower than those of the sample (800 °C), whereas the particle density was the reverse. However, Kim et al. [27] produced a thin layer of $Sr_{0.98}Ti_{0.95}Co_{0.05}O_{3-\delta}$ and then subjected it to various reducing conditions, and reported that a greater reduction temperature can exsolve

NPs' of lower particle size. The composition of exsolved NPs is also influenced by temperature. J. Ma et. al. [28] discovered that when $La_{0.95}Fe_{0.8}Co_{0.2}O_3$ is heated to 500 °C, the exsolved particles are made of Co-Fe alloy. Whereas, $La_{0.95}Fe_{0.8}Co_{0.2}O_3$ only exsolved Co NPs as the temperature rose beyond 600 °C. This effect results from cation exchange between Co in the matrix oxide and Fe in the Co-Fe alloy NPs. As previously noted, a cation exchange process took place as the reduction temperature rose higher, and at 900 °C, a single metal, Co, was eventually produced on the surface of the matrix.

Recent studies have looked at the crucial part that different reducing gas atmospheres play in regulating the shape of the exsolved NPs. Under 5% CO atmosphere, exsolved particles typically have a cube-type morphology, and under H_2 atmosphere, the cube-type morphology will change to quasi-spherical or elliptic geometric forms. It's interesting to note that Gao et al. [25] likewise showed the pro-portion association between hydrogen concentration and the size/density of exsolved NPs. According to their research, the density of Ni particles released from $La_{0.4}Sr_{0.4}Sc_{0.9}Ni_{0.1}O_{3-\delta}$ with an A-site deficiency rose as the H_2 partial pressure decreased. Additionally, Kim et al. [27] found that an increase in density and a decrease in NP size can be caused by a drop in oxygen partial pressure. Furthermore, various heating rates and energy sources (such plasma) produce outcomes that vary in size, density, and shape.

2.2.2 Internal Control

A-site deficiency design is more effective and tactic than stoichiometric perovskite for NPs to be exsolved from a matrix and produce a uniform distribution on surfaces. Yu et al. [29] prepared a series of $Sr_xFe_{1.3}Ni_{0.2}Mo_{0.3}O_{6-\delta}$ (x = 1.95, 2.00, and 2.05) catalysts and revealed that the exsolved amount of Fe-Ni alloy increases along with decreasing x. A viable method to encourage exsolution is the fabrication of A-site defective perovskites (A/B < 1).

The species of the metal ions in the B-site and their way of interaction with the perovskite matrix, however determines how they behave during exsolution. According to certain studies, adding the right heterogeneous atoms to B-sites can both efficiently induce exsolution and regulate the compositions that result from it. Y. Jiang et. al. [30] research reported $La_{0.9}FeO_3$ (LFO) exsolution in relation to the impact of B-site doping. It resulted that Co-Fe alloy may be exsolved from $La_{0.9}Fe_{0.9}Co_{0.1}O_3$ (LFCO) after thermal reduction treatment at 500 °C, but exsolution is not possible in LFO without B-site doping. Notably, because the production of Co-Fe bond is simpler than the formation of the Fe-Fe bond under the same conditions, this explains that Co doping has a positive influence on the exsolution of Fe. Additionally, it was discovered that the exsolved Co-Fe alloy and the matrix oxide generated a strong connection, indicating that the composites are extremely stable. However, Co doping, in a similar manner, also encourages the exsolution of other alloys.

Researchers have shown that exsolution factors including particle size and coverage distribution density are greatly influenced by the crystal orientation. The exsolution of NPs in the films from Kim et al. [27] was found to be influenced by the surface orientation of the substrate, which also altered the particle shape and surface coverage area. The exsolved particles show greater catalytic efficacy at the (111) oriented surface because they had the smallest particle size, deepest embedding, most surface coverage, and most uniform particle spacing. The work presented a method for creating extremely effective catalysts by demonstrating how altering the substrate orientation may regulate the exsolution of NPs on heterogeneous epitaxial oxide films.

2.3 Important features associated with metal exsolution

2.3.1 Conductive oxides and exsolution hosts

Many conductive ceramics feature perovskite or perovskite-related structures, making them perfect for use in SOFC electrodes that make use of the exsolution principle. For a simple perovskite ABO_3, where the A-site cations are located in the corners of the unit cell, the B-site cations are located in the middle and are coordinated by six oxygen atoms that form a BO_6 octahedron. Although the perovskite structure permits some mismatch in the lengths of the A-O and B-O bonds, this mismatch is restricted in that the Goldschmidt tolerance factor, t must be between 1 and 0.75. The total of the charges on the A and B cations must equal six. Equation 2.3.1 demonstrates that this tolerance factor depends on the radii of the component ions.

$$t = \frac{r_O + r_A}{\sqrt{2}(r_O + r_B)} \qquad \text{.....} \qquad \text{Eq. 2.3.1}$$

Here, the ionic radii of the oxygen anions, the B-site cation, and the A-site cation are designated by the letters r_A, r_B, and r_O, respectively. As long as the guest cation satisfies the criteria for crystal stability, other metal cations can be swapped into the lattice. It is possible to induce electrical or ionic conductivity as well as create oxygen vacancies in the lattice by substituting cations with various or changing charges.

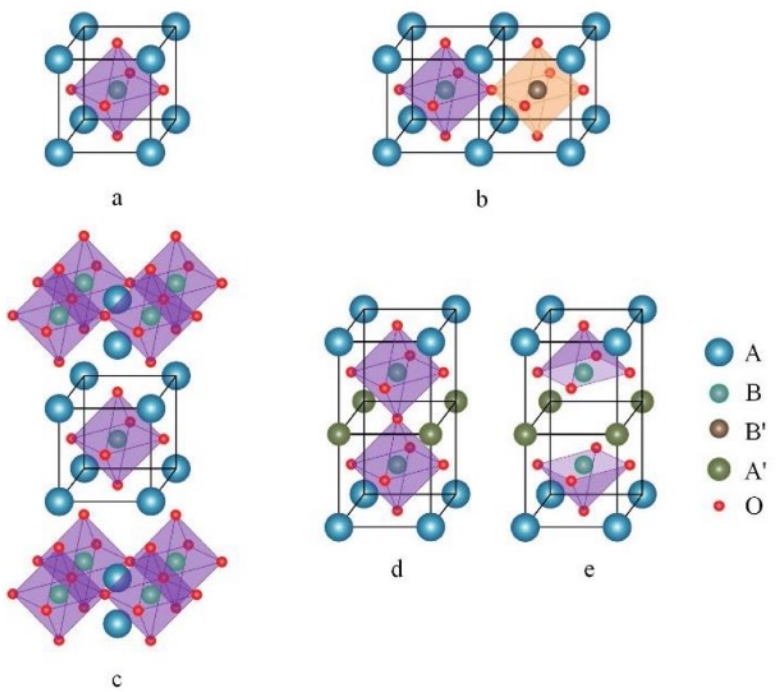

Fig. 2.3.1 Unit cells of perovskites (a) ABO_3 structure of simple perovskite; (b) $A_2BB'O_6$ of double perovskite, volume of its unit cell is twice as that of the simple perovskite; (c) Ruddlesden–Popper (RP) perovskite, with one layer of ABO_3 cells sandwiched in the middle; $AA'B_2O_{5+\delta}$ layered double perovskite, (d) oxidised; (e) reduced (δ~0). Spheres of different colours denotes different sites. Black frame in the ABO_3 unit cell is a guide for the eyes; [11]

When the B site contains multivalent cations as $Cr^{3+/4+}$, $Ti^{3+/4+}$, $Fe^{2+/3+}$, $Mn^{2+/3+/4+}$, etc., perovskites become electronic conductors after suitable treatment, e.g. high temperature reduction. [31]. Charge can travel along the lattice because these atoms can change their valence. By creating oxygen vacancies and stabilising the reduction of B-site cations, doping the A sites with divalent cations significantly improves the ionic conductivity. Because conductivities are often a strong function of $p(O_2)$, which under reducing circumstances is governed by the H_2:H_2O ratio and temperature, this presents a challenge. The n-type conductivity is favoured for SOFC anodes since it tends to increase in more reducing environments. SOFCs can also use more intricate structures that comprise BO_6 octahedra in addition to straightforward perovskites. Double perovskites are a straightforward version in which the B sites alternately contain two distinct metal cations, B and B'. Due to the Ruddlesden-Popper perovskite's (RP-perovskite) frequent occurrence of materials with relatively high ionic conductivities, this version is another popular one that is frequently utilised in electrode applications. The BO_6 octahedral slabs that make up the RP-perovskite structure have A-site cations wedged between two of the adjacent slabs. This arrangement increases ionic conductivity by lowering the activation energy required for oxygen anions to travel along these [AO] layers. High temperatures are often needed for the direct synthesis of the RP-perovskite phase. If the initial material, either a simple or double perovskite, includes reducible cations at the B sites that may be removed from the lattice, this phase can occasionally be produced using reductive treatments. The reducible cations subsequently depart the lattice, which induces the RP-perovskite phase. A material with too many A-site cations is formed when the RP-perovskites are created by this phase transition. High ionic conductivities have been reported for the double-perovskite structure. When compared to simple perovskites, this structure may have a lower energy barrier for the exsolution of metal cations.

2.3.2 Manner of lattice substitution

The occurrence of lattice replacement of the metal cations in the host oxide is frequently ambiguous. excluding scenarios where the host oxide and the oxidised metal catalyst just mix physically and only taking into account situations where the metal cations can enter the host oxide's lattice. A change in the host lattice parameter or spectroscopic evidence for lattice substitution are often required to show that the dopant catalytic metal cations penetrate the host lattice. Not all metal cations can be integrated into all ceramics, even those with perovskite structures. Substitution of cations into the lattice of a host oxide is also unique to the composition of both the metal cations and the host oxide. Additionally, there is proof that metal cations can act as lattice site A or B substitutes and that exsolution is possible in both stoichiometric and A site-deficient perovskites. The B sites of simple perovskites like $LaFeO_3$ are often thought to be occupied by the majority of reducible cations, such as Ni^{2+}, $Co^{2+/3+}$, etc. However, when the radius of the A-site cation is comparable in size to that of the dopant cations and some metals appear to occupy both types of sites, A-site replacement is conceivable.

2.3.3 Mechanisms and energetics of the exsolution process

Depending on the particular system, the exsolution procedure's specifics may change. Metal clusters are generated during reduction in at least some instances, and the particles are then pushed to the surface by strain in the host oxide [32]. Other times, metal cations may interact with one another to form particles, diffuse to the surface, and be reduced. Each of these mechanisms will be covered separately. Exsolution is thought to be triggered by the system's greater energy while the particles are in bulk because of the host's

strain field, which causes exsolution to reduce the system's overall energy. The strain-field calculation revealed an intriguing result: only particles that are near to the free surface—roughly three times the particle radius away—can achieve relaxation and emerge from the host. The energetics of Ni particles developing in the bulk of the $La_{0.2}Sr_{0.7}Ti_{0.9}Ni_{0.1}O_3$ host were also studied by Kim et al. [27]. They took into account Ni particles that, after reduction, were only partially exposed to the gas phase and were partially embedded in the oxide host. Their simulation showed that the Young's modulus and Poisson's ratio of both the metal and the oxide play significant roles in the exsolution process. Differences in the mechanical qualities result in variations in the quantity, radius, and depth of the attached particles by altering the strain field. The second potential exsolution process includes the reduction of metal cations that diffuse to the host's surface. For instance, Neagu et al. [33] proposed that the Ni^{2+} cations must migrate to the surface of the host oxide before being reduced by H_2 in their STEM analysis of Ni particles developing on $La_{0.43}Ca_{0.37}Ti_{0.94}Ni_{0.06}O_3$. They used the fact that Ni particles only developed on the sample's surface and stayed fixed in place at their original nucleation sites as support for their claim. The surface reduction process for the similarly comparable $La_{0.4}Sr_{0.4}Sc_{0.9}Ni_{0.1}O_3$ exsolution system was assessed by Gao et al. [25]. They came to the conclusion that the mass transport of Ni^{2+} from the bulk, the reduction kinetics of Ni^{2+}, and the strain between the particle and its host could all affect how quickly exsolved Ni^0 particles grew. They also concluded that the reduction of surface Ni^{2+} cations nucleated further growth through migration and reduction of additional Ni^{2+} from the bulk.

The layered double perovskites have also been linked to the surface reduction process. In this process, the oxygen vacancy and the metal cations that make up the majority of the material exsolve to the surface. By generating nearby oxygen vacancies as part of the reduction process, the metal cations on the surface are further stabilised. Due to the high concentration of lattice oxygen vacancies in layered double perovskites, this process may be favoured in these materials. It is crucial to understand that, regardless of the mechanism at play, lattice reconfiguration will occur in the host oxide when metal cations undergo exsolution. When metal cations are removed from the lattice, vacancies are created. These vacancies can cause distortions in the crystal structure or even a general loss of crystallinity in the oxide. For instance, surplus A-site cations remain in the oxide after B-site cations have been exsolved. As was previously mentioned, this can cause a perovskite phase to change into an RP phase [34]. Other times, structural alterations could be much more drastic.

The provision of an external source of metal cations to replace the vacancies is one approach to this issue, known as topotactic ion exchange. The fact that the exsolved metal particles create a distinctive interface with the surface of the oxide host, where the particle seems to be partially implanted or socketed, is a defining feature of many exsolution systems. The socketed structure results from the balancing of the lattice strain due to the metal particle and the surface free energy. In cases where the surface reduction mechanism is operative, particle embedding could still occur as a consequence of particle growth. According to Neagu et al. [33], Ni particles on the surface grow epitaxially and push the adjacent oxide laterally apart to make room for growth. Hence, stress in the surrounding oxide lifts the surface to form a volcano-shaped socket.

2.3.4 Mechanical analysis of exsolution process

Although the exact mechanism underpinning exsolution is still unknown, earlier experiments and theoretical analysis have suggested a number of plausible early steps in the exsolution process. Neagu et al.

[33] suggested that one mechanism can be the defect-mediated exsolution, where they studied that the amount of exsolved metal NPs on LSNiT (A-site deficient) surface was increased with an A-site defect concentration. Their hypothesis was that, the main reason for this boosted Ni exsolved NPs, was due to the fact that the A-site deficiency changes the oxygen vacancy number so as to maintain the perovskite stoichiometry, and then the reducing environment increases the number of oxygen vacancies in the system. As a result, the metal atoms gets reduced from their oxide phase to their metallic phase, which is the B-site metal exsolution, or the reduction of metal oxide followed by the exsolution of Schottky defects. However, in this hypothesis of mechanism, the degree of exsolution depends on a certain threshold of oxygen vacancies that is required to maintain the uniformity of the perovskite structure. Another set of hypothesis regarding the mechanism was suggested by Sun et al. [35] that the oxygen vacancy formation destabilises the lattice structure under the presence of reducing environment, which induces the B-site cations exsolution. Also the oxygen vacancy and the B-site cations defects, such as Schottky defects results to this exsolution of metal NPs from B-site. G. Jiang et al. [36] worked with phase field modelling to study kinetically the exsolution phenomenon on a perovskite system with non-equilibrium thermodynamics. Their result suggested that spinodal decompositions depending on the reduction contain, A-site deficiency system and segregation energy triggers this exsolution process. Their theory was that the dopant segregation, i.e the B-site metal segregation towards the material surface and the reduction of this segregated dopant which breaks the bond between oxygen and B-site metal, can be considered as a key factor for the exsolution process.

Using the density functional theory (DFT) method, the co-segregation energies for a layered perovskite system with B-site metals Co, Ni and Fe, was calculated. Where, the segregation of a dopant's atom with an oxygen vacancy is defined as a co-segregation energy, that was used to describe the dopants segregation under a reducing environment, where the oxygen vacancies are more easily formed. The result showed higher co-segregation energies for Co and Ni, whereas it was lower for Fe. This implied that Co and Ni exsolution from the host perovskite is more favourable than Fe. As this segregation takes place, the segregated dopant should get decomposed or reduced to its metallic phase, from the oxide phase. This can be preceded by the creation of oxygen vacancies close to the gated metals, and the energy required for these vacancies to occur on the surface can be calculated using DFT. Co and Ni form oxygen vacancies more readily than the host Mn or Fe dopant, according to the energy of oxygen vacancy production. More readily than the host Mn or Fe dopant, oxygen vacancies. As a result, the exsolved NP-containing synthetic electrode materials displayed a greater power density together with long-term stability. These findings demonstrate that computational methods may effectively capture the key features of B-metal exsolution, which is useful for designing exsolution materials and for explaining the mechanism at the atomic level. Nucleation and growth start to occur close to the surface once the dopant atoms segregate toward the surface. In general, the equilibrium between the two competitive components of volume (bulk) free energy and inter-facial (surface) free energy determines the Gibbs free energy for a certain size of particle.

Due to the limitations of the measurable scale, the complexity of the reaction, and the high cost of experiments, even though the exsolution phenomenon has many benefits in the fields of catalysis and electrode materials, the underlying mechanism and the source of the high catalytic activity produced are still unknown. In this way, we can deepen our understanding of the atomic and electrical structures of the materials thanks to the high accuracy of computational tools. The effective integration of computational and experimental approaches is a beneficial strategy that compensates for the inherent limits of each approach

through continuous feedback between them, even if it is still difficult to cover every aspect of exsolution using simply computational simulations.

2.4 Properties of exsolved particles

The original intent behind the creation of "intelligent" catalysts was to revive catalysts that had been rendered inactive due to loss of dispersion brought on by metal sintering [33]. The idea was that under oxidising circumstances, metal cations may be reinserted into the lattice and, following reduction, exsolved back as well-dispersed metals. Metal cation insertion into the lattice appears to happen too slowly for this process to function under real-world circumstances. The dispersion of perovskite-supported metals does seem to be maintained far more effectively than that of their conventional counterparts, though. The support contained pits where the particles had been, which were visible when the particles were removed by etching. There are, however, some circumstances in which stability can only be accounted for by powerful interactions between the metal and the support.

2.4.1 Catalytic properties

Metals that have been exsolved can also have altered adsorption and reactivity characteristics. For instance, although having a very high catalytic activity for CO oxidation, the chemisorption of CO on Pt released from $LaFeO_3$ has been reported to be quite low at ambient temperature [37]. This indicates that the CO oxidation process on the exsolved catalysts is very different from the reaction that occurs on catalysts made using traditional techniques. On a variety of perovskite-supported metals, CO chemisorption has been found to be suppressed. Strong metal-support bonding interactions that affect the chemisorption capabilities of the metal and partial coverage of the metal with an oxide layer are two potential reasons for the changes in chemisorption and reaction properties. Additionally, there are hints that exsolved metals could have increased sulphur tolerance. Because chemisorbed sulphur is extremely persistent on the Ni surface, conventional Ni-based SOFC electrodes deactivate in the presence of H_2S or other sulphur-containing chemicals [38]. There are signs that exsolved Ni suppresses sulphur adsorption, enabling steady SOFC performance at greater sulphur levels. The use of additional metals for the catalytic sites is also permitted by the use of conductive ceramics in SOFC anodes, paired with the introduction of catalytic sites by exsolution, and some of these metals may be sulphur-tolerant [35]. The major distinction between NPs created using traditional deposition techniques and exsolved NPs is the degree to which the NPs are partially incorporated into the host perovskite. Finding the contact between exsolved NPs and the host perovskite structure is crucial for modelling these NPs at the atomic level. Exsolved NPs' unknown atomic structure has led to the usage of a number of potential models to characterise them. These include the surface doping model, the tiny metal cluster inclusion model, and the non-socketed NP model (deposition model).

2.4.2 Typical materials for catalytic electrodes

The electrodes in SOFCs are perhaps the most important and demanding parts that determine cell performance. Their main job is to efficiently and at high turnover rates catalyse the fuel oxidation reaction at the anode and the oxygen reduction reaction at the cathode. They must also have strong electronic conductivity in addition to catalytic activity to effectively move electrons to and from the external circuit. They must be able to operate at high temperatures while maintaining chemical, structural, and thermal stability in

the very reducing environment of the fuel at the anode and the highly oxidising environment, which is commonly air at the cathode. The interfaces between the electrolyte and composite electrode components must be stable and nonreactive, as they play significant roles in the charge transfer process that normally occurs at the triple phase borders (TPB). To prevent thermal mismatch, which can cause mechanical failure during the SOFC's thermal cycling, functional cell components must have closely matched thermal expansion coefficients. Finding and creating excellent electrode materials that satisfy these strict standards is so difficult. Precious metals are understandably too expensive to be used as catalytic electrode materials in practical applications. Ni is the most extensively used active catalyst in SOFC anodes along with YSZ or ceria to form the composite cermet structure because of its low cost and high catalytic activity. Similar to this, the active cathode material in SOFCs has traditionally been mixed with conducting doped perovskites. Reducing the significant activation loss linked to the sluggish oxygen reduction reaction at the cathode is a key obstacle to efficient SOFC operation. High activity, high electronic and ionic conductivity, mechanical robustness, chemical, structural, and thermal stability are all necessary, as well as resistance to inter-diffusion or solid state reactions with the electrolyte that can lead to electrolysis. Unfortunately, the development of high performance catalytic cathodes for SOFCs has been slow, in part because of these requirements. Only a select few materials could be able to achieve these demanding specifications. In particular, LSM and LSCF compositions have received the most research attention and are now used in cutting-edge SOFC cathode designs. It is unfortunate that the development of high performance catalytic cathodes for SOFCs has been slow in part because it calls for the right combination of material properties, such as high catalytic activity, high electronic and ionic conductivity, mechanical robustness, chemical, structural, and thermal stability both in the oxidising gaseous environment at the cathode component as well as against inter diffusion or solid state reaction with the electrolyte that can lead to electrolysis. Few materials could be able to achieve these strict specifications. LSM and LSCF compositions in particular have been among the most investigated, and they are now used in cutting-edge SOFC cathode designs.

Anodes are an essential part of SOFCs because they provide versatility and flexibility in the use of various fuels for oxidation. Anode must, among other things, have a high catalytic activity to oxidise the fuel, provide enough electronic conductivity to capture the released electrons, and have mechanical, thermal, and chemical stability to withstand the highly reducing anode environment. Ni/YSZ ceramic has been the most popular SOFC anode material since it was discovered and introduced more than 40 years ago. Undoubtedly, a variety of additional anode materials have been investigated for use in actual applications, but still there is difficulties that remain today for the efficient and direct use of hydrocarbon fuels in SOFCs. The structural stability of $SrTiO_3$-based doped perovskites over a broad oxygen partial pressure range and their reasonably high electronic conductivity under reducing atmospheres drew interest as potential catalytic anodes for SOFCs. However, in order to achieve high catalytic activity and cell performance, it is necessary to optimise micro-structural factors like porosity, and particle size, as well as the spatial distribution and relative loadings of the active metal or catalyst with the ionically conducting solid electrolyte component of the composite anode. This will ensure that there is good electronic percolation to ensure electrical connectivity in the 3-dimensional porous structure, as well as chemical and thermal stability.

3. Experimental

3.1 Synthesis of Powders

An LSCFeT compound with a defective A-site was synthesised to accelerate the Fe exsolution process, thus for enhancing the catalytic activity of LSCFeT material. Three different compositions of LSCFeT was prepared with 10%, 18% and 25% mol. of Fe content. The synthesis of the powders was done using the Pechini method. The precursors were taken in an appropriate amount during the preparation of the materials, which were metal nitrates: $La(NO_3)_3.6H_2O$ (Sigma-Aldrich/Merck, 99.99%), $Sr(NO_3)_2$ (Pol-Aura, 99%), $Ce(NO_3)_3.6H_2O$ (Sigma-Aldrich/Merck, 99%), and $Fe(NO_3)_2.6H_2O$ (Sigma-Aldrich/Merck, 99%), and were weighed and dissolved in DI water to create a water salt solution. A stoichiometric amount of titanium (IV) butoxide ($Ti(OBu)_4$, Merck, 97%) was mixed together separately with reagent-grade ethylene glycol (EG) of density 1.114 g/cm^3, and citric acid (CA) in a molar ratio equal to 2:1 until a white slurry mix was obtained, i.e it acts as a chelating agent in the solution. The water-based solution was then mixed with the titanium precursor mixture and stirred, until it was completely dissolved. The solution was then heated to 150 °C, till the time it took the formation of a wet gel. 6g of powders were prepared for each material for the sintering, and the stoichiometric details(+/- 0.005 gm) of the compositions are presented in Table 3.1.1.

Table 3.1.1 Stoichiometric composition of $La_{0.27}Sr_{0.54}Ce_{0.09}Fe_xT_{1-x}O_{3-\delta}$ ($LSCFe_xT_{1-x}O_{3-\delta}$)

	$LSCFe_{0.1}T_{0.9}O_{3-\delta}$	$LSCFe_{0.18}T_{0.82}O_{3-\delta}$	$LSCFe_{0.25}T_{0.75}O_{3-\delta}$
La(NO3)3x6H2O	1.1313	1.0621	1.0009
Sr(NO)3	1.1058	1.0382	0.9783
Ce(NO3)3x6H2O	0.3781	0.355	0.3345
Fe(NO3)2x6H2O	0.3909	0.734	1.0376
C16H36O4Ti	2.9936	2.8104	2.6484
CA	7.7222	7.6314	7.5511
EG	8.1863	8.0901	8.0049

*all units are in grams

This gel was then transferred in to an alumina crucible and was put into the furnace for calcination. There the materials or the gels were calcined in air atmosphere environment for 1 hour at 400 °C at a rate of 3 °C/min, then for another 1 hour at 600 °C at the same rate. Finally the materials are heated to 1200 °C for 12 hours, and lastly cooled down to room temperature 25 °C. The temperature profile for the calcination process is presented in Fig. 3.1.1, and the mechanism of Pechini type sol-gel method is presented in Fig 3.1.2. After temperature treatment, these materials takes a form of a solid network like structure (presented in Fig. 3.1.3), which is then ground to a mixture of homogenous powders (presented in Fig. 3.1.4). The sintered powders were weighed to be 1.6080 g, 1.2449 g and 1.6192 g for Fe_x content, (x = 0.1, 0.18, 0.25) respectively. The exsolution of Fe NPs was then performed, with the prepared powders which were heat-treated again under the stream of dry H_2 at 900 °C for 10 hours with a with of 50ml/min.

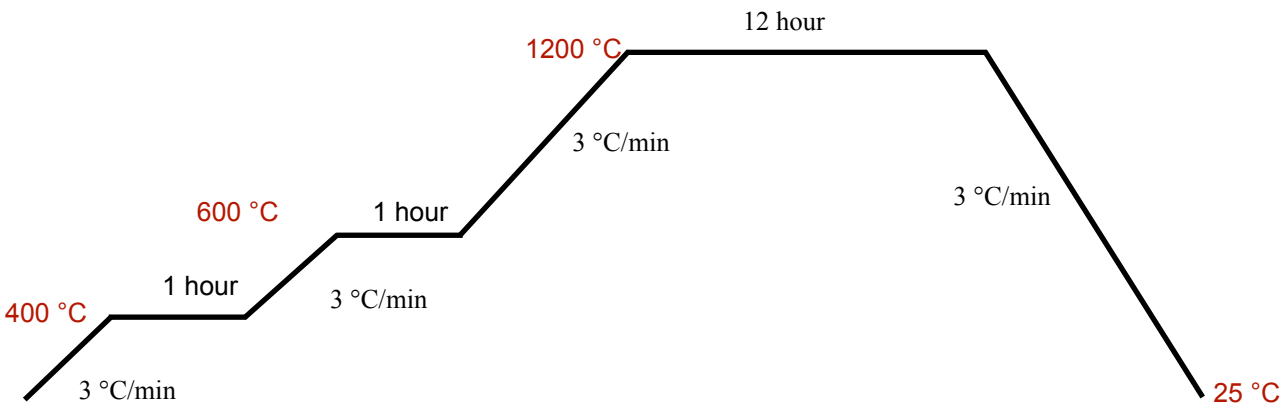

Fig. 3.1.1 Schematic plot of calcination temperature profile

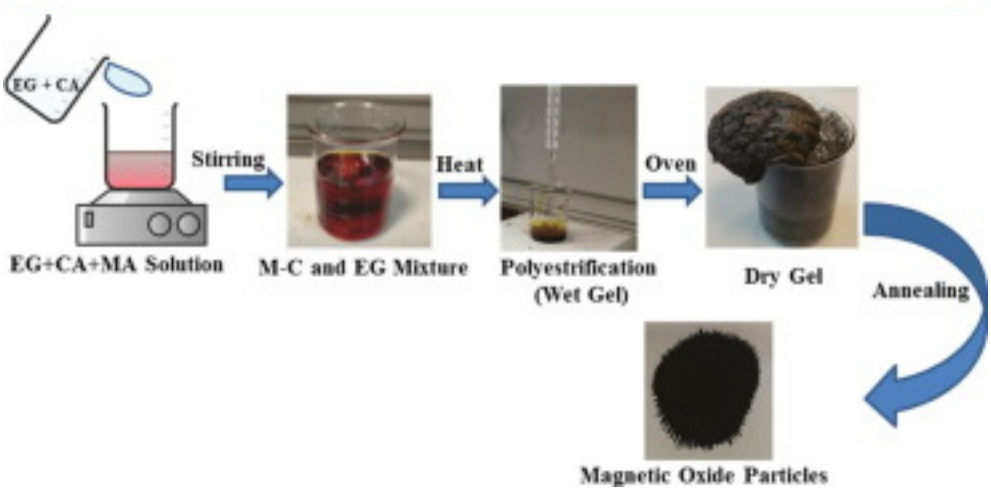

Fig. 3.1.2 Schematic of Pechini type sol-gel method of material preparation [39]

Fig. 3.1.3 Material after calcination (solid network like structure)

Fig. 3.1.4 $LSCFe_xT_{1-x}O_{3-\delta}$ powders after sintering, (Left) x=0.1 (Middle) x=0.18 (Right) x=0.25

3.2 Materials Characterisation

The structure of fabricated compounds were analysed with X'Pert Pro MPD Philips diffractometer using $Cu_{K\alpha}$ (ƛ = 1.542 Å) radiation at room temperature, and the results were analysed using Malvern Panalytical HighScore Plus program. The structural refinement was carried out with Rietveld method of profile analysis using the same program, and the unit cell parameters were recorded. The size of the crystallites and their strain were calculated using the Scherrer Equation. The size and uniformity of the exsolved NPs, as well as the morphology of the powders were verified after the reduction process via the Scanning Electron Microscopy (SEM) using the instrument FEI Quanta FEG 250.

3.3 Experimental Characterisation Techniques

3.3.1 X-Ray Diffraction (XRD)

A common method for examining the crystal structure of materials is X-ray diffraction (XRD). It gives important knowledge on how atoms or ions are arranged within a substance and can be used to identify a number of structural characteristics, including phase identification, lattice parameters, crystal symmetry, crystal orientation, and the presence of structural flaws. High-energy electromagnetic waves with a wavelength of between 10^{-3} and 10^{1} nm are referred to as X-rays. Typically, sealed tubes, spinning anodes, or synchrotron radiation sources are used to generate X-rays. The same technique is employed by laboratory equipment that uses revolving anodes and sealed tubes to produce X-rays. A strong potential field accelerates electrons produced by heating a tungsten filament in a vacuum before they are directed at a target, which then produces X-rays. Therefore, the radiation emanating from a spinning anode or a sealed tube is a superimposition of distinct radiations with a continuous spectrum. The majority of residual radiation is often eliminated by employing suitable filters or monochromator using XRD methods, which typically only

use the characteristic radiation with the highest intensity, the Kα radiation. A distinct theory governs the creation of X-ray radiation in synchrotrons, where it is produced by clusters of electrons or positrons moving at relativistic energies very close to the speed of light. A high power electron gun generates high energy electrons that are then pumped into a booster ring for acceleration. Typically, magnets are arranged in a periodic fashion to create undulatory. The emission of photons results from the electrons being made to follow a sinusoidal route in the ring's orbital plane. X-ray photons can interact with matter in a variety of ways, which can result in a variety of absorption and scattering effects. Between the photons and the electrons around the atomic nuclei, there is an elastic (coherent) scattering that is also known as Rayleigh scattering. The X-ray diffraction by periodic atomic planes and the angle- or energy-resolved detection of the diffracted signal are the foundation of the approaches. W.L. Bragg (Bragg, 1913) provided the geometrical explanation of the XRD phenomena (constructive interferences). Details regarding the geometry required for diffraction and the discovery of Bragg's law are provided in Fig. 3.3.1. Bragg's law is presented in Eq. [3.3.1].

$$n\lambda = 2d_{hkl}sin(\theta) \qquad \text{..... Eq. [3.3.1]}$$

Where, n is the order of diffraction, ƛ is the wavelength of the incident beam in nanometers, d_{hkl} is the lattice spacing in nanometers, and **θ** is the angle of the diffracted beam in degrees. When using the XRD technique, a sample is exposed to an X-ray beam, and the diffraction pattern that is produced as a result of the X-rays' interaction with the crystal lattice is measured. Constructive interference occurs when X-rays interact with the atoms in a crystal, creating different diffraction peaks. Intensity distribution as a function of the 2**θ** angle is the typical representation of diffraction data. Fig 3.3.2 illustrates the extractable information content.

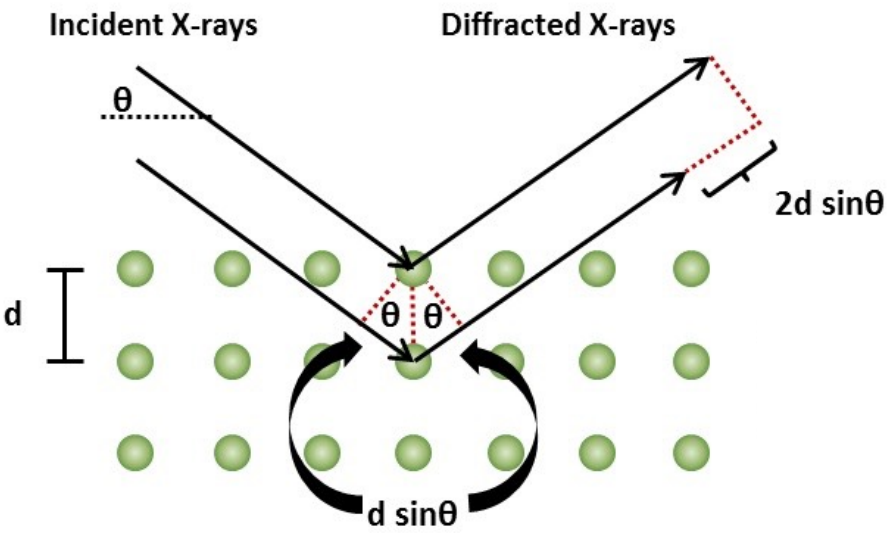

Fig. 3.3.1 Geometrical condition for diffraction from lattice planes [40]

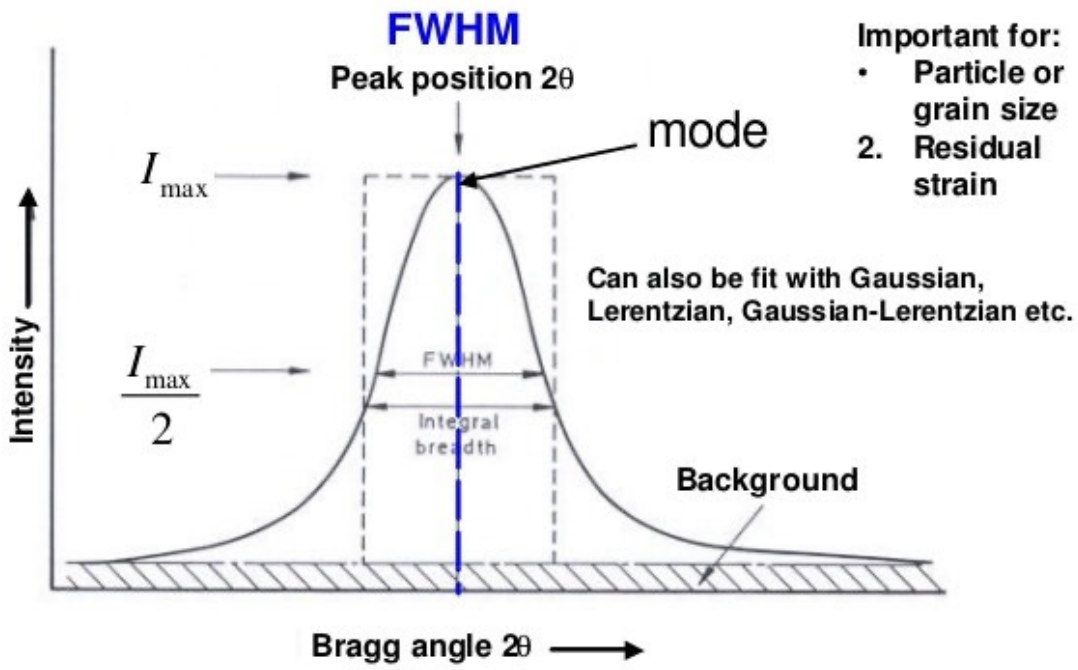

Fig 3.3.2 Diffraction peak and information content that can be extracted [41]

a) Rietveld Refinement

In order to ascertain the crystal structure and improve the structural characteristics of a material, the Rietveld refinement method is a technique of data analysis utilised in X-ray and neutron diffraction investigation. Hugo Rietveld, a Dutch physicist, is honoured as the technique's namesake. A sample is exposed to an X-ray or neutron beam in X-ray or neutron diffraction studies, and the resulting diffraction pattern is noted. The Rietveld refinement method can be used to evaluate this pattern, which provides details regarding the crystal structure. This method involves convolution of the emission profile (W), all instrumental contributions (G), and sample contribution (P) to calculate the profile. An alternative method for measuring the instrumental function is to use a standard without sample broadening. Because the huge crystallites of around 2 mm do not significantly expand the peaks, the standard SRM660a (LaB6) is typically employed. It is important to verify the reliability of the results and that they adhere to predetermined standards at the conclusion of a refinement. Different plots between observed and calculated data are generally the best criterion for refinement. The various criteria that are taken into consideration for the refinement must be verified when there are significant disparities. The derived criterion Residuals weighted profile (Rwp), which measures the fit quality, provides accurate information. Therefore, the best refining is represented by the smallest Rwp number. In relation to the quantity of refined parameters (Q) and the number of experimental points (N), the parameter Rexp denotes the lowest predicted Rwp. The goodness of fit (GOF), which can also be employed as a metric of refinement quality, is determined by the ratio of the two parameters. The powder diffraction approach could only develop the crystal structures of inorganic salts and tiny organic molecules, which were quite simple. The Rietveld method is one of several techniques that must be used in concert to solve and refine difficult and complex crystal structures. An idealised crystal lattice in nature is decorated by imperfections and defects; perfect crystals only exist in theory. These departures from the ideal order can be better understood with the aid of Rietveld refinement.

b) Scherrer Equation

The Scherrer equation, which assumes that the crystallites are roughly spherical in shape, provides an estimate of the average crystallite size in a material. It is crucial to remember that the equation has its limitations and is only an approximation. The material's potential complexities, such as the polydispersity of crystallite sizes, impacts of preferred orientation, and others, are not taken into account. When characterising materials, the Scherrer equation is frequently used to quickly determine the size of the crystallites based on X-ray or neutron diffraction data. It offers a helpful beginning point for comprehending the structural characteristics of crystalline materials, but for a thorough analysis of the size distribution or other structural traits, more advanced analysis approaches could be needed. In order to determine the average crystallite size in a material based on the broadening of X-ray or neutron diffraction peaks, one can apply the Scherrer equation, which bears the name of the Swiss physicist Paul Scherrer. For the size of the coherent scattering domains (crystallites) within a material, it offers a straightforward approximation. Scherrer equation is presented in Eq. [3.3.2]. The size of the crystallites (D) and the widening of the diffraction peak (β) are related by the equation. It ignores additional considerations like strain or flaws and instead argues that the broadening is solely brought on by the crystallites' finite size.

$$D = \frac{K\lambda}{\beta cos\theta} \qquad \text{..... Eq. [3.3.2]}$$

3.3.2 Scanning Electron Microscope (SEM)

The concept of SEM dates back to the thirteenth century, when a first electron microscope was built using research done in 1933 by two physicists named Ruska and Knoll. Von Ardenne then added a scan coil to a TEM in 1938 and created a scanning transmission electron microscope (STEM) with a voltage of 23 kV, an 8000x magnification, and a resolution of 50–100 nm. SEM (Fig. 3.3.3) is a tool that allows for the observation of the microscopic and nanoscale worlds. SEM can show details and intricacy that are hidden from view by optical microscopy. This can all be accomplished by using the procedure below, which Goldstein et al. [43] described in detail. The mechanism is that, a beam of electrons with high energy in the region of (100-30,000 eV) is used to conduct the analysis of the surfaces's morphology. For electron emission, a heat source is typically employed. The SEM is outfitted with lenses to compress the spot size and to direct the focused electron on the specimen because the gun's spot size is too large to provide a sharp image. The majority of SEMs have a spot size of less than 10 nm, and the signals needed to create a picture are produced when the electrons that were captured from the final lens interact with the specimen and penetrate to a depth of 1 μm (micro-meter). The electron beam is moved to discrete locations in the form of straight lines until a rectangular raster is established on the specimen's surface, at that time the electron beam moves point by point to create the image of the specimen. The required magnification determines the entire operation. The scan coils cause the beam to deflect across a smaller area in the event that the user desires a greater magnified image. It is important to note that the working distance, or the distance between the last lens and the specimen's surface, affects the magnification. In the current SEM, this problem is resolved automatically.

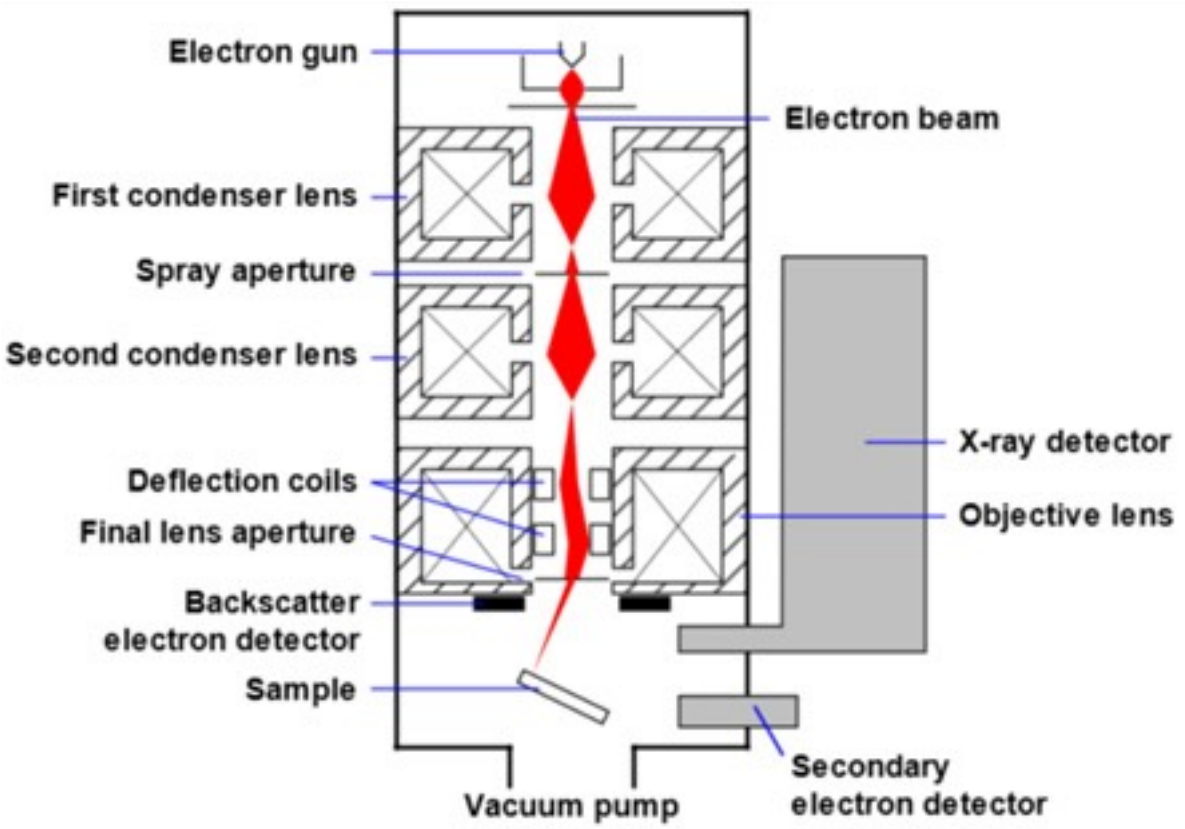

Fig. 3.3.3 Schematic of Scanning Electron Microscope (SEM) [42]

The purpose of an electron detector is to pick up signals that the scanned material has emitted as electrons. In the creation of SEM images, both secondary electrons (SE) and backscattered electrons (BSE) are employed. Both SE and BSE will be collected when a positive voltage is applied to the collector screen. In the event that a negative voltage is provided to the collector screen, only BSE will be collected. The operator will then manage the brightness and intensity until a reasonable clear image is obtained after the signals are presented on the viewing screen. Magnification over (10,000x) should be used when the specimen has to have small details. The offered details are influenced by the electron voltage mode (emitted by the gun). If modest accelerating voltages less than (5 kV) are utilised, the scanned image will be rich in surface information. On the other hand, the high acceleration voltages (15–30 kV), which penetrate beneath the surface, will cause the reflected signal from the surface to transmit information about the sample's interior. Fig. 3.3.4 displays various electron penetration levels through the sample and reflected signals. The visualisation of the sample's topography in terms of shape, size, and surface roughness is necessary to get a partially three-dimensional image from a scanning electron microscope (SEM). And this is based on the BSE and SE numbers. Surprisingly, the topographic difference is directly impacted by the angle of inclination of the sample surface, which increases both of the aforementioned figures. A tilt angle greater than 50° up to 70° causes the quantity of BSE and SE signals to reach their peak. The physicochemical, optical, and electronic properties of nanoparticles are dependent on their size and surface properties. A 2-nm particle may have different electronic and surface properties than a 10-nm particle. Surface functionalised nanoparticles may exhibit different properties than the corresponding bare particles. Therefore, their size measurement is essential to ensure reproducible beneficial and/or toxic effects [45].

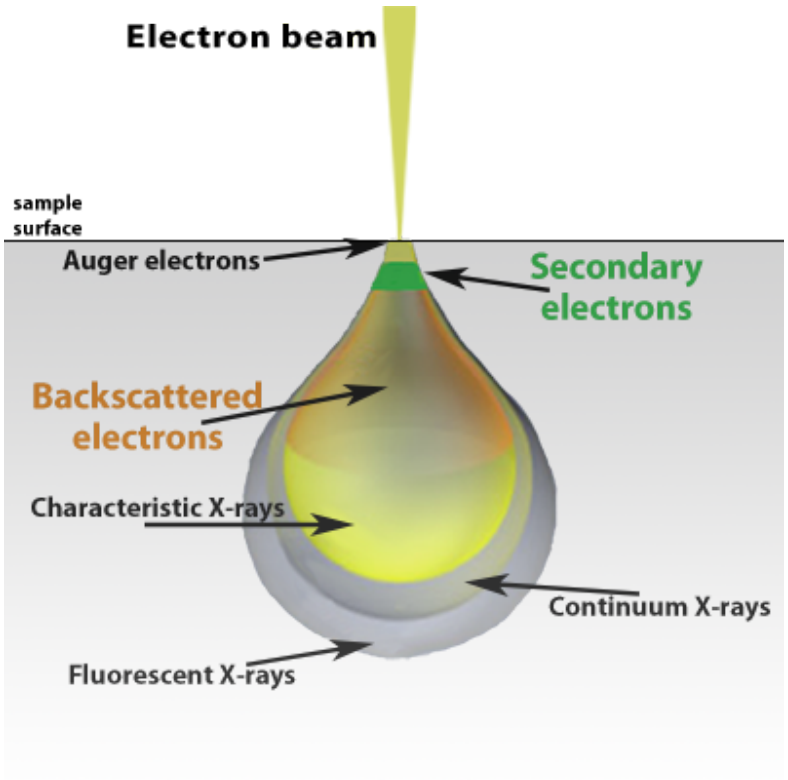

Fig. 3.3.4 Different types of signals generated depending on the electrons' penetration depth [44]

As per Lee et. al. [46], SEM with a secondary electron detector can visualise crystal shape, surface morphology, dispersed and agglomerated secondary electron detector can visualise crystal shape, surface morphology, dispersed and agglomerated nanoparticles, and surface functionalisation. SEM is regarded as a method that provides an absolute measurement of particle size since it can inspect each particle, including the aggregate particles, separately. Depending on the shape of the particle, the difficulty of measuring particle size varies. For instance, the diameter of spherical particles can be used to completely define them. The size distribution of the materials is crucial and must also be decided because the majority of material formulations come in a variety of sizes. The mean particle size and standard deviation can be used to characterise the particle size distribution (PSD), which can be represented as a bell-shaped curve that resembles a normal distribution. The distribution of many medicinal powders, however, does not resemble a bell. Some have a bias toward the largest particles in the range. These powders are frequently best represented by a log-normal distribution, which resembles a normal distribution curve when the data are shown using a log scale for the size axis. The geometric mean standard deviation and geometric median particle size are used to explain the distribution when employing a log-normal representation. For in situ SEM imaging, the sample should be tilted so that both the electron beam and depositing fluxes impinge on the sample surface [47]. The benefit of in situ SEM is that it can image surfaces without halting the growth along a variety of ranges.

4. Results and Discussion

4.1 Exsolution of Fe metallic NPs

4.1.1 X-Ray Diffraction (XRD)

The measurement was done for two sets of materials, one for the materials before undergoing reduction in dry H_2, and the other after the reduction under the flow of dry H_2. The obtained XRD patterns of as-prepared materials are shown in Fig. 4.1.1, whereas the XRD patterns of these powders, but after reduction in H_2 at 900 °C are presented in Fig. 4.1.4. In the first set of XRD patterns, for materials before reduction (as-prepared), the primary peak can be attributed to $SrTiO_3$ or $SrTiO_3$ - like phase with space group Pm-3m having a cubic crystal system structure (presented in Fig. 4.1.3). Different amount of dopants led to some structural changes, resulting in a slight shift of main peak. Therefore different phases were recognised, but of a very similar structure: $Sr_{0.9}La_{0.1}TiO_3$ and $(La_{0.6}Sr_{0.4})FeO_3$. Although the peak positions of these phases seem to be almost the same. Only Rietveld refinement analysis allowed to differentiate the phase composition of individual samples.

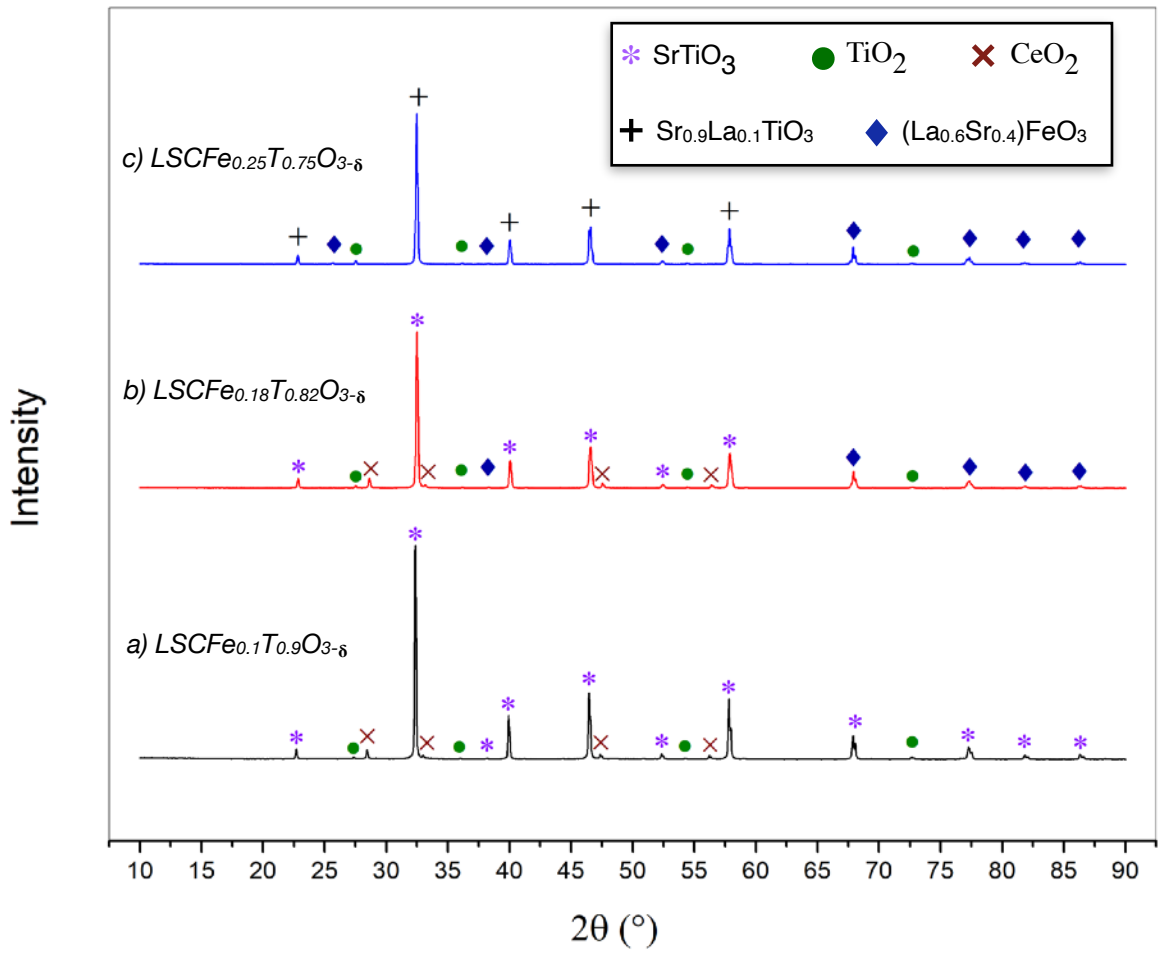

Fig. 4.1.1 XRD patterns of the as-prepared LSCFeT powders

The additional phases that were found for materials containing 10 and 18 mol.% of Fe were CeO_2 with space group Fm-3m having a cubic crystal system structure, with a phase content of 0.9% and 3% respectively and TiO_2 with space group P42/mnm having a tetragonal crystal system structure, with a phase content of 8.1% and 2% respectively. All recognised phases and their content in particular compound determined by the Rietveld refinement method are shown in diagrams in Fig. 4.1.2. As the Fe content is increased in the material, i.e for $LSCFe_{0.25}T_{0.75}O_{3-\delta}$, it resulted to have a very different phase composition from the other two materials. The primary phase resulted to be of perovskite Strontium Lanthanum Titanium Oxide - $Sr_{0.9}La_{0.1}TiO_3$, with space group Pm-3m having a cubic crystal structure (presented in Fig. 4.1.3) with a phase composition of about 76%. The secondary phases were of Iron Titanium Oxide - Fe_2TiO_5 of space group Bbmm with orthorhombic crystal structure, Lanthanum Strontium Iron Oxide - $(La_{0.6}Sr_{0.4})FeO_3$ of space group R-3c with rhombohedral crystal structure, and Titanium oxide - TiO_2 of space group P42/mnm with tetragonal crystal structure, with a phase composition of 3%, 17% and 4% respectively.

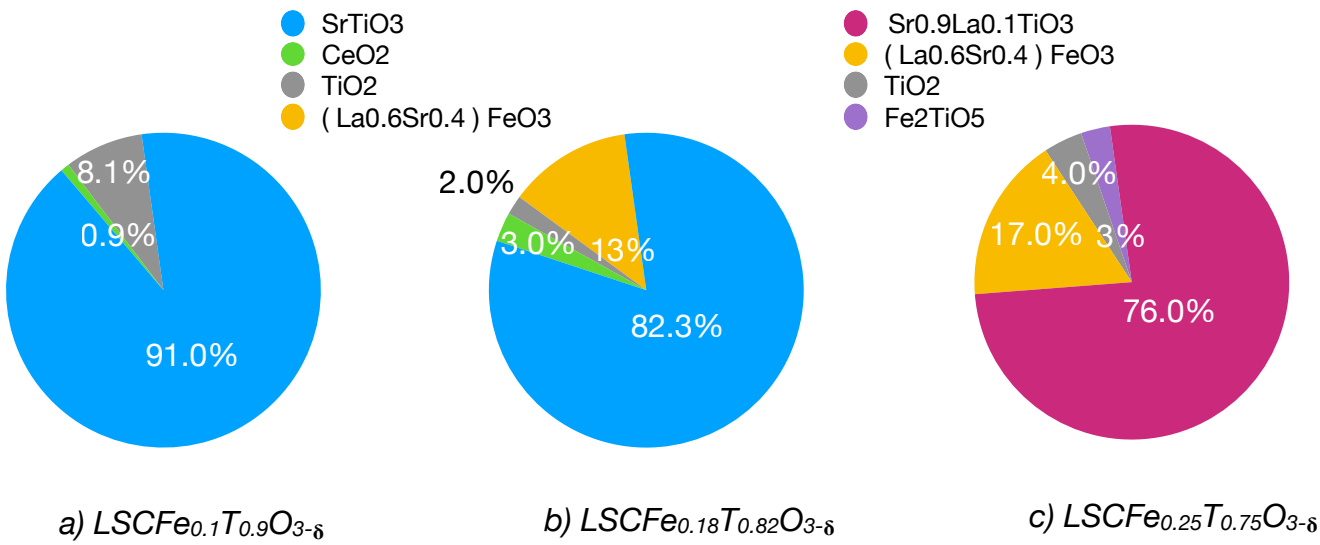

Fig. 4.1.2 Phase composition from XRD measurement before reduction

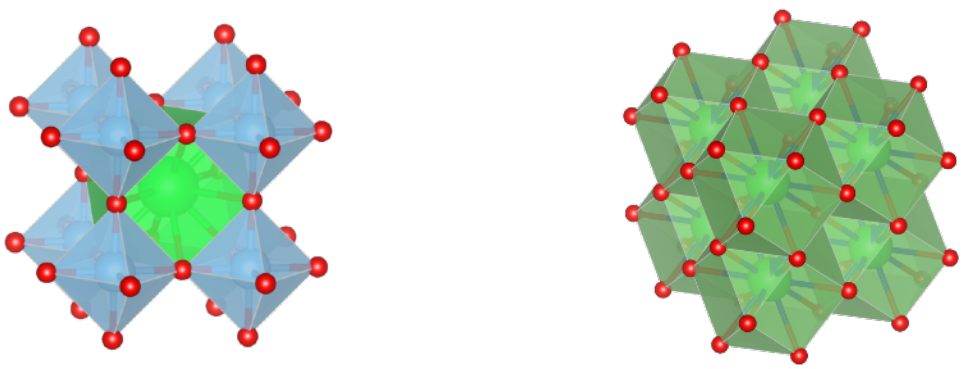

Fig. 4.1.3 Crystal structure of (left) $SrTiO_3$ and (right) $Sr_{0.9}La_{0.1}TiO_3$, - model generated in Vesta software

In the next part of the experiment the materials were then reduced under exposure to dry H_2 at 900 °C for 10 hours at a flow of 50mL/min. The poor chemical stability of Fe-based perovskite materials often leads to phase decomposition in reducing atmosphere. The materials with 10% and 18% mol. of Fe content maintained to have the same phase composition after the reduction though. $LSCFe_{0.1}T_{0.9}O_{3-\delta}$ had the same phase composition before and after the reduction as the Fe content is comparatively lower than the other materials. Whereas, an evident change is observed for the other materials, where for $LSCFe_{0.18}T_{0.82}O_{3-\delta}$ after reduction no phases with Fe content is present, resulting to exsolved Fe NPs. The primary phase for these materials were of $SrTiO_3$ with a phase composition of 95%, which was determined from the Rietveld refinement (presented in Fig. 4.1.5). The additional phases that were found for these materials were CeO_2 with a phase content of 2% and 1% respectively and TiO_2 with a phase content of 3% and 4% respectively. As well for $LSCFe_{0.25}T_{0.75}O_{3-\delta}$, the $Sr_{0.8}La_{0.2}TiO_3$ occupying a phase content of 85% was found. The secondary phases were of Iron Titanium Oxide - Fe_2TiO_5, Titanium oxide - TiO_2, with a phase composition of 11% and 4% respectively.

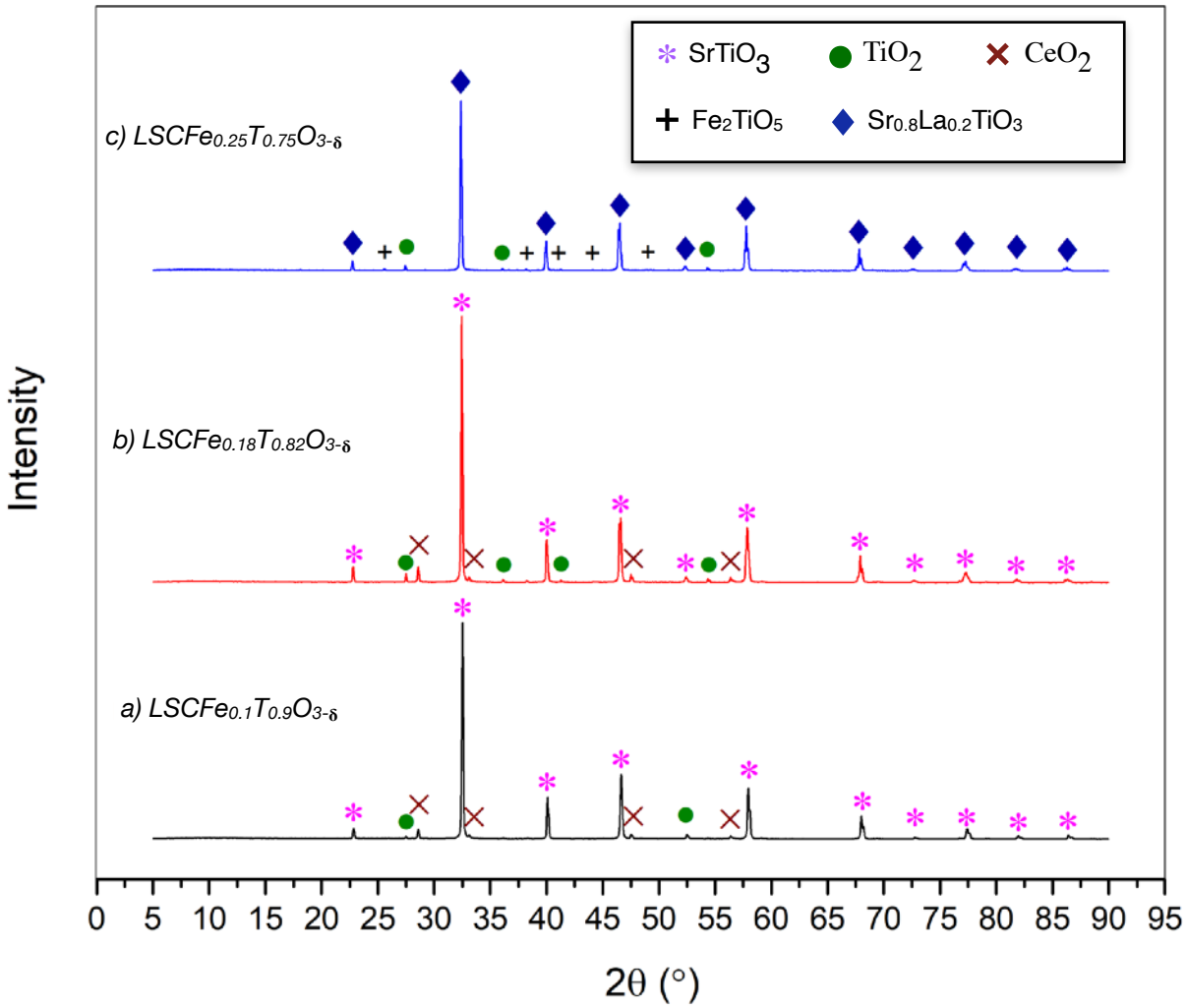

Fig. 4.1.4 XRD patterns of the reduced LSCFeT powders

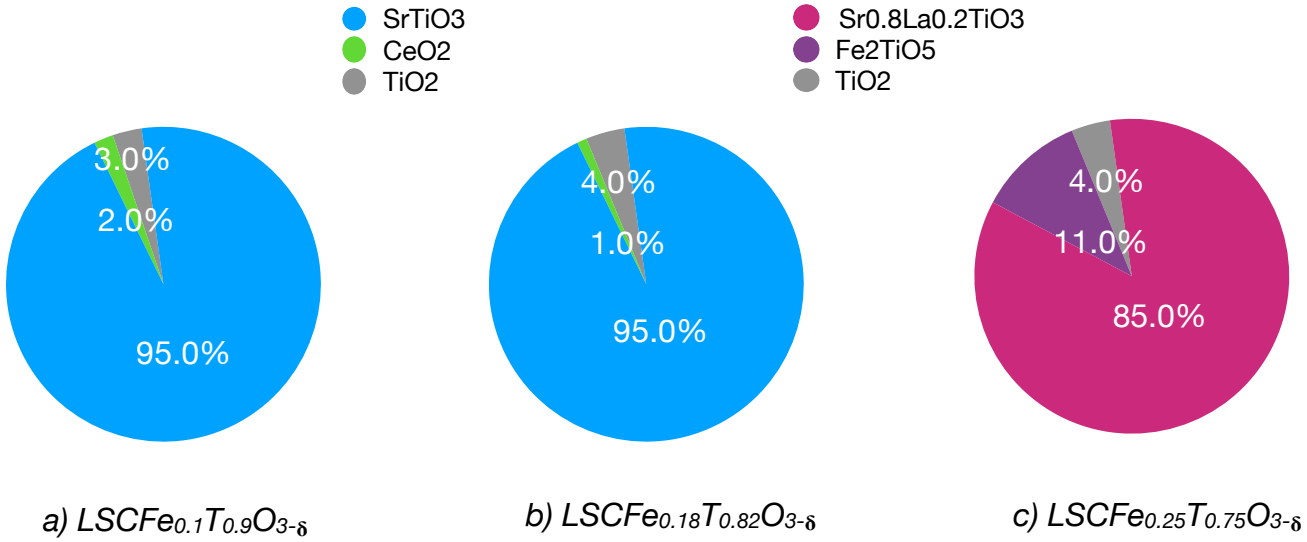

Fig. 4.1.5 Phase composition from XRD measurement after reduction

It is well agreed that strong reduction conditions are required to bring the metal cations to the surface of exsolution catalyst. Therefore, if Fe-doped perovskites are reduced in H_2 at high temperature , the Fe can be reduced to its metallic form and exsolved on the surface of the perovskite. Referring to the paper of Jingcheng Li et al. [48] reported in their research work - in situ growth of Fe-Ni alloy NPs with perovskite precursor $La_{0.4}Sr_{0.6}Fe_{0.75}Ni_{0.1}Nb_{0.15}O_{3-\delta}$ (LSFNNb), performing the reduction with similar conditions, i.e exposure to wet H_2 at 900 °C for 1 hour, resulted to the sample being partially decomposed to a mixture of $LaFeO_3$ type perovskite as main phase, $SrLaFeO_4$ type layered perovskite as as minor phase, and metallic Fe-Ni alloy with Fe-Ni_3 structure. Generally, the introduction of high-valency cations such as Ti^{4+} into the B-site lattice, is proved to be an effective way to improve the structural stability, as in this case materials with the primary phase of $SrTiO_3$, are considered to be structurally more stable.

The shift of XRD peaks in a diffraction pattern to the left (toward smaller angles) denotes a widening of the lattice spacing, which is equivalent to an enlargement or expansion of the crystal lattice. For a given lattice plane, the diffraction angle (θ) decreases as the unit cell size grows since the distance between crystal planes likewise expands. As a result, the diffraction peaks of the main perovskite shifts towards lower angles after treating the anode powders in dry H_2, and a lattice parameter shift is associated with the change is the oxidation state of Fe. The shifting of the main XRD peak in XRD patterns of samples before reduction (Fig 4.1.6) and after reduction (Fig. 4.1.7) is presented below.

These peak positions were recorded as - 32.34°, 32.50° and 32.48° for $LSCFe_xT$ (as-prepared) with (x = 0.1,0.18,0.25) respectively. Whereas, after reduction with the expansion in the unit cell, these intense peaks shifted towards left and their peak positions were recorded as - 32.52°, 32.45° and 32.38° for $LSCFe_xT$ with (x = 0.1,0.18,0.25) respectively. The size and arrangement of the A and B cations within the crystal lattice are the main determinants of the unit cell size in perovskite materials. The unit cell size may change if alternative cations, such as Fe, are used in place of the B-site cations. The normal atomic arrangement is upset and a solid solution is produced when Fe is added as a substitutional dopant to the perovskite structure.

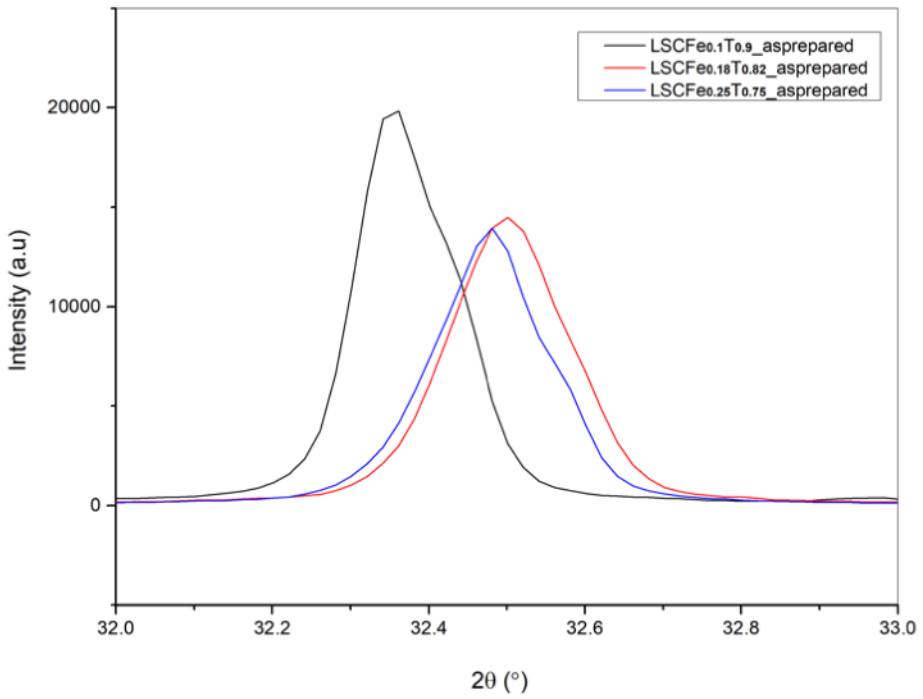

Fig. 4.1.6 Comparison of the most intensive XRD peak in results of as-prepared materials

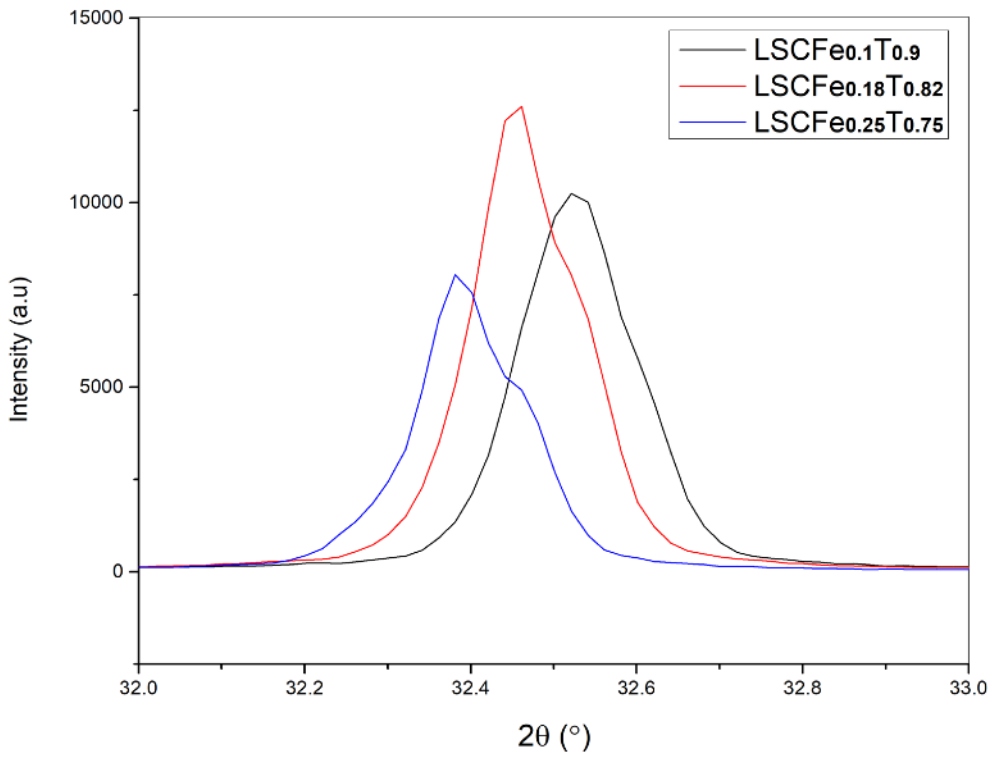

Fig. 4.1.7 Comparison of the most intensive XRD peak in results of materials after reduction

The coordination number and oxidation state of the ions can affect the ionic radii of Fe and Ti. When ionic radii are compared, Fe^{2+} ions with coordination number VI tends to have larger ionic radii than Ti^{4+} ions. Compared to Fe^{2+}, Fe^{3+} ions have a somewhat smaller ionic radius. After reduction, there is a chance of metals getting reduced in their valency state, like Ti^{4+} to Ti^{3+}, Fe^{4+} to Fe^{3+}/Fe^{2+}. Ti^{4+} ions can promote structure stability and can constrain the oxidation state of the other valence variable ions in the B-site lattice. Moreover, the ionic radii of Ti^{4+} (0.0605 nm) is similar to that of Fe^{3+} (0.0645 nm), thus the Fe^{3+} can substitute the B-site lattice easily. Therefore, when Fe is substituted for Ti or vice versa in a material, the lattice parameters and crystal structures may be affected by the difference in ionic radii, which may have ramifications for their assimilation into crystal lattices. The unit cell size may need to be increased to accommodate the bigger Fe ions due to Fe's higher ionic radius when compared to the other cations (La, Sr, Ce, and T).

On the basis of the XRD measurement, the lattice parameters of LSCFeT were calculated using the Rietveld refinement method, and are presented in Table 4.1.1, for the case of before and after reduction process. Lattice parameter of main $SrTiO_3$-like dominant phases present in LSCFeT materials from the XRD measurements, before and after the reduction is presented in Fig 4.1.8. The cubic perovskite phase was maintained by the doped material. Due to the decreased ionic radii of XII-coordinated La^{3+} and Ce^{4+} ions relative to a Sr^{2+} ion, the lattice parameter of the doped $SrTiO_3$ was slightly reduced [49]. The size and arrangement of the cations within the crystal lattice have a significant impact on the lattice constant in perovskite materials. Due to the different ionic radii and electronic characteristics of Fe relative to the original cations, when Fe is replaced for other cations in the perovskite structure, it might result in changes in the lattice constant.

Table 4.1.1. Unit cell parameters of LSCFeT

$LSCFe_{0.1}T_{0.9}O_3$				
Phase	**Unit cell parameter [Å] of as-prepared materials** ($\alpha = \beta = \gamma = 90°$)	**Goodness of Fit (GOF)**	**Unit cell parameter [Å] of reduced materials** ($\alpha = \beta = \gamma = 90°$)	**Goodness of Fit (GOF)**
$SrTiO_3$	a = 3.895 b = 3.895 c = 3.895	2.017	a = 3.895 b = 3.895 c = 3.895	1.507
CeO_2	a = 5.410 b = 5.410 c = 5.410		a = 5.413 b = 5.413 c = 5.413	
TiO_2	a = 3.813 b = 3.813 c = 6.043		a = 3.759 b = 3.759 c = 8.064	
$LSCFe_{0.18}T_{0.82}O_3$				
Phase	**Unit cell parameter [Å] of as-prepared materials** ($\alpha = \beta = \gamma = 90°$)	**Goodness of Fit (GOF)**	**Unit cell parameter [Å] of reduced materials** ($\alpha = \beta = \gamma = 90°$)	**Goodness of Fit (GOF)**
$SrTiO_3$	a = 3.904 b = 3.904 c = 3.904	2.225	a = 3.903 b = 3.903 c = 3.903	2.169
$(La_{0.6}Sr_{0.4})FeO_3$	a = 5.533 b = 5.533 c = 13.516		-	
CeO_2	a = 5.513 b = 5.513 c = 5.513		a = 5.402 b = 5.402 c = 5.402	

Phase	Unit cell parameter [Å] of as-prepared materials (α = β = ɣ = 90°)	Goodness of Fit (GOF)	Unit cell parameter [Å] of reduced materials (α = β = ɣ = 90°)	Goodness of Fit (GOF)
TiO_2	a = 4.593 b = 4.593 c = 2.959		a = 4.592 b = 4.592 c = 2.959	
$LSCFe_{0.25}T_{0.75}O_3$				
Phase	**Unit cell parameter [Å] of as-prepared materials (α = β = ɣ = 90°)**	**Goodness of Fit (GOF)**	**Unit cell parameter [Å] of reduced materials (α = β = ɣ = 90°)**	**Goodness of Fit (GOF)**
$Sr_{0.9}La_{0.1}TiO_3$	a = 3.908 b = 3.908 c = 3.908	2.637	-	2.572
$Sr_{0.8}La_{0.2}TiO_3$	-		a = 3.913 b = 3.913 c = 3.913	
Fe_2TiO_5	a = 3.724 b = 9.786 c = 9.970		a = 9.740 b = 9.890 c = 3.693	
$(La_{0.6}Sr_{0.4})FeO_3$	a = 5.521 b = 5.521 c = 13.483		-	
TiO_2	a = 4.592 b = 4.592 c = 2.960		a = 4.551 b = 4.551 c = 2.928	

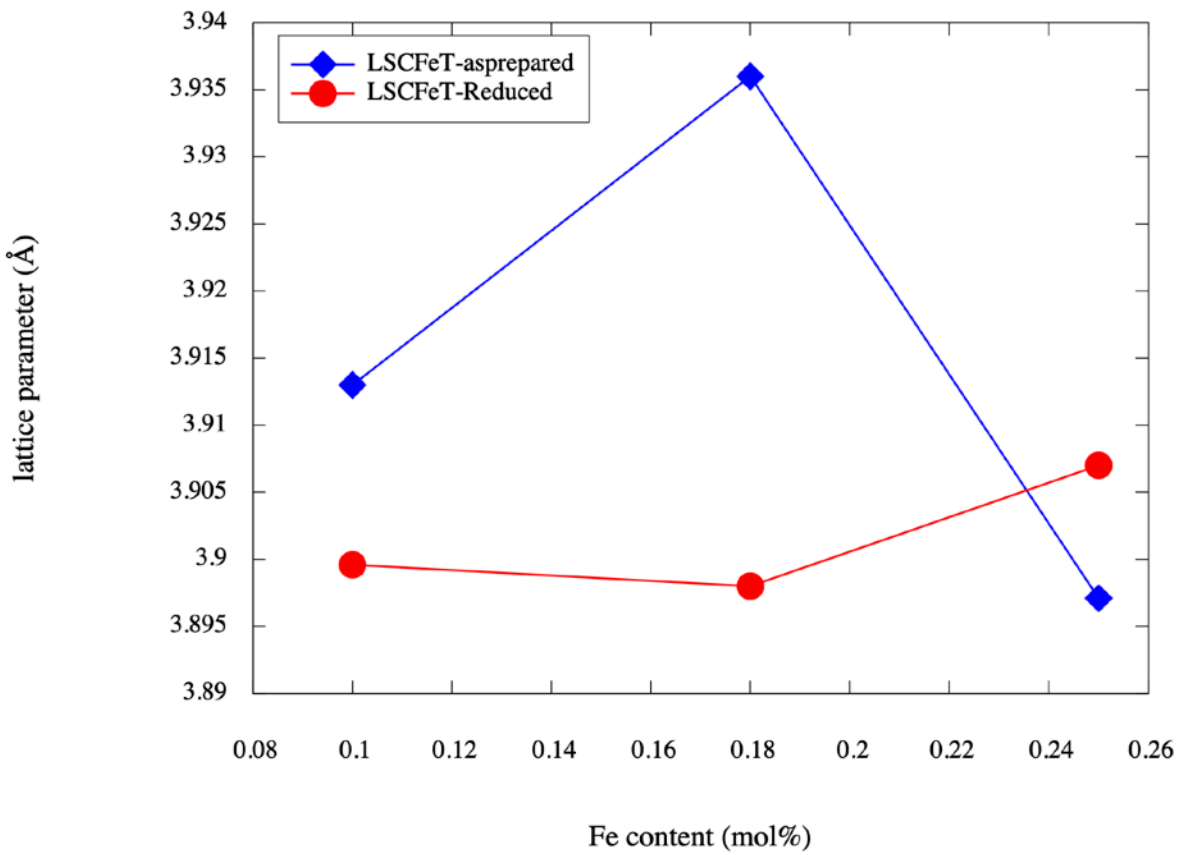

Fig. 4.1.8 Lattice parameter of main $SrTiO_3$-like dominant phases present in LSCFeT materials, before and after the reduction

Hydrogen gas can cause redox reactions with a substance's constituent parts when the material is exposed to the hydrogen molecules. There are some circumstances when this can lead to the reduction of metal ions, changing the oxidation state and impacting the crystal structure and lattice. As it was noticeable that the peaks of the primary phase slightly shifted to the small angle as compared with the XRD results from before reduction, hence indicating cell expansion due to the increase of Fe content. The cell volume for LSCFeT was calculated from the Rietveld refinement lattice parameters, that resulted to a cell volume of 59.5932 $Å^3$ for $LSCFe_{0.25}T_{0.75}O_{3-\delta}$, which is bigger than 59.0957 $Å^3$ for $LSCFe_{0.1}T_{0.9}O_{3-\delta}$. This is due to the introduction of higher amount of Fe in the material, that results to more of Fe^{2+} (0.68 Å) and less of Fe^{3+} (0.0645 Å) in the lattice due to its electronic configuration, which therefore increases the bond length and the cell volume. The bond lengths and cell volume of LSCFeT slightly increases after the reduction, thus owing to partial reduction of Fe^{3+} in oxidised LSCFeT to Fe^{2+}. This formation of higher content Fe^{2+} ions after reduction in the material can be further confirmed by XPS measurements. The XPS is considered as a surface sensitive technique that measures the kinetic energy of the electrons ejected from the surface of the material, when exposed under X-rays or ultraviolet radiations. The kinetic energy of these emitted electrons depends on the binding energy of the electrons in the atomic orbitals of the surface atoms, which is specific to each element and its chemical state. Thus XPS enables the identification of the electronic state of elements present on the surface and their chemical environment. However, this kind of analysis was not possible in a limited time of realisation of Master Thesis project. It may be performed in a future.

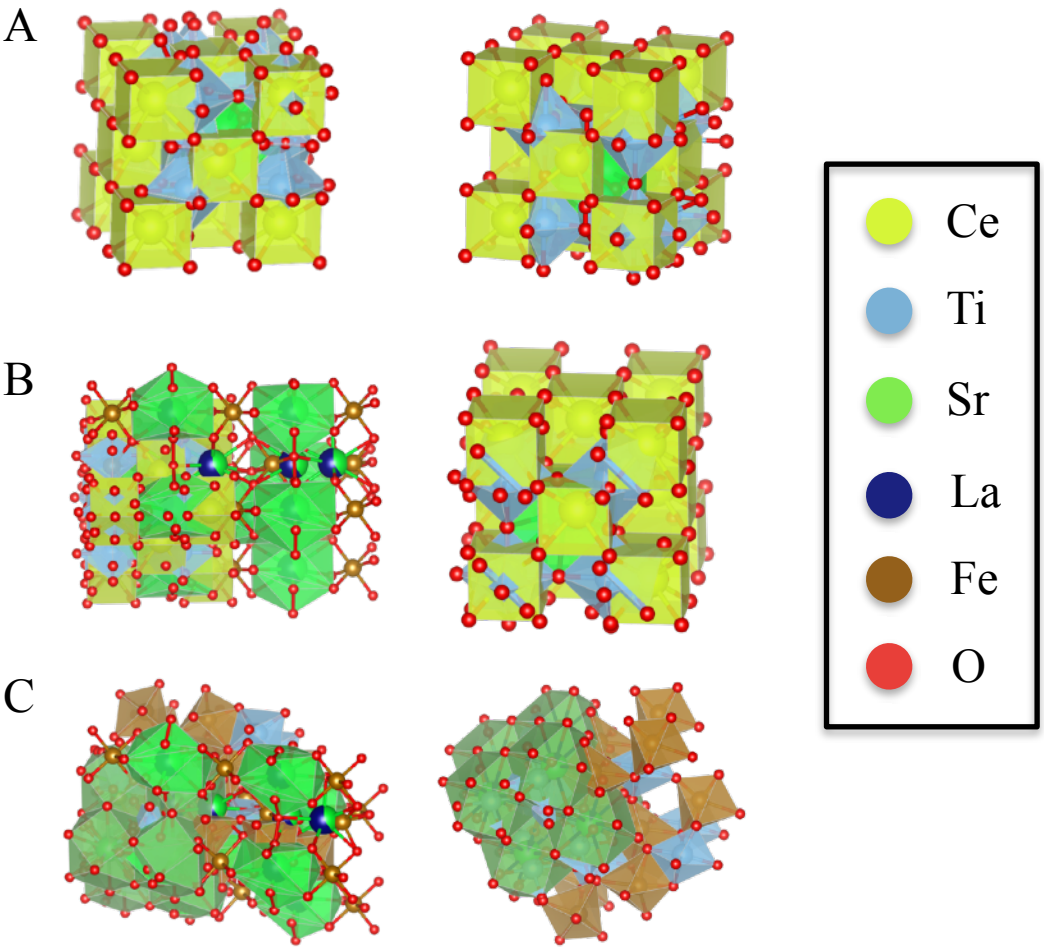

Fig. 4.1.9 Crystallographic structure of $LSCFe_xT_{1-x}O_{3-\delta}$, (left) before reduction, (right) after reduction; A) x = 0.1, B) x = 0.18, C) x = 0.25

The exemplary visualisation of the crystallographic structure of these materials, reconstructed using the VESTA program from the XRD measurement results are presented in Fig. 4.1.9 for visual understanding of the phases present in the materials.

The size of the crystallites and lattice strain from the intense peaks of XRD measurements were calculated with Scherrer equation, as presented in Eq. [3.3.2]. The results are presented in Table 4.1.2. Strain effects between lattice-mismatched over-layers may offer fascinating new possibilities and a useful lever to adjust a material's catalytic characteristics. Elastic strain can be introduced into materials in a variety of methods, such as lattice mismatch at multilayer interfaces, applied stress, or chemical expansion, which is seen in nonstoichiometric and doped oxides. The strain in the over-layer caused by the mismatch in the lattice constants across a layer interface causes the strained surface to have different catalytic characteristics. It is evident that strain can change the catalytic activity and energy barrier profile of surface adsorbates along the reaction coordinate [50]. It has been demonstrated that near-surface alloying is a useful tool to influence and improve catalysis because it changes the host material's surface electronic structure and offers a useful way for creating catalysts with high activity and selectivity [51]. In comparison to the metal over-layer itself, a stretched metal over-layer on top of another metal substrate exhibits noticeably different catalytic activity. To adjust strain and alter surface kinetics and catalysis on these oxides, doped-perovskites' chemical expansion caused by the substantial oxygen non-stoichiometry sustained by these materials can be used as an additional lever [52]. With increased lattice strain, which is typically expected to decrease the oxygen vacancy formation energy by weakening the metal-oxygen bonds, the reaction energies for various surface rate processes are predicted to drop [50].

Table 4.1.2. Crystallite size and lattice strain values calculated using the Scherrer Equation for LSCFeT

	$LSCFe_{0.1}T_{0.9}O_3$		$LSCFe_{0.18}T_{0.82}O_3$		$LSCFe_{0.25}T_{0.75}O_3$	
	Crystallite size [nm]	Lattice Strain %	Crystallite size [nm]	Lattice Strain %	Crystallite size [nm]	Lattice Strain %
Before Reduction	98.2	0.123	93.6	0.147	99.7	0.158
After Reduction	99.8	0.156	99.7	0.161	100.2	0.168

4.1.2 Scanning Electron Microscopy (SEM)

The as-prepared LSCFeT powders were then placed into an alumina crucible and thermally treated under the flow of dry H_2 at 900 °C for 10 hours. The SEM images of the materials after reduction process is presented in Fig. 4.1.10. From the images, it is clearly visible that the reduction temperature has got crucial influence on the exsolved NPs sizes, as well as on the amount of these exsolved NPs in relation with the different material compositions. It is supposed that the formed NPs are of Fe, but to clearly confirm their composition the TEM with EDS analysis should be performed. The EDS detector attached to the SEM microscope can not distinguish objects of such a small size.

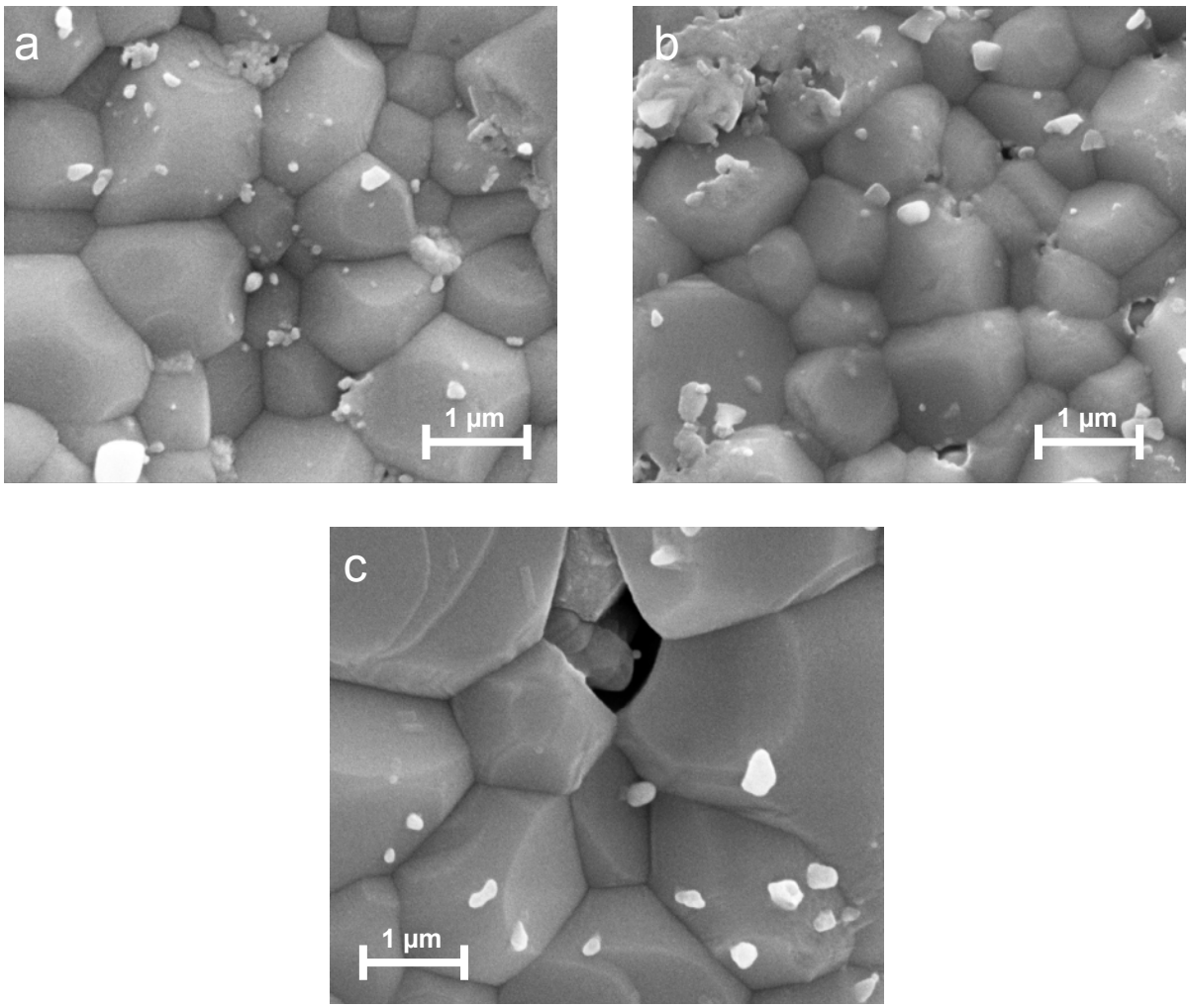

Fig. 4.1.10 SEM images of LSCFeT powders reduced at 900 °C in dry H_2 for 10 hours. Letters refer to different Fe content : a) $Fe_{0.1}$, b) $Fe_{0.18}$, b) $Fe_{0.25}$. Scale bar is 1 µm

On turning to the morphological analyses of the materials after the exsolution treatment, it is observed that the number of exsolved NPs is higher for $LSCFe_{0.1}T_{0.9}O_{3-\delta}$ as compared to $LSCFe_{0.25}T_{0.75}O_{3-\delta}$. As observed from the above SEM images, that all the materials exhibited the presence of well-dispersed NPs covering the surface of the porous perovskite materials, even though through agglomeration of NPs for the case of $LSCFe_{0.25}T_{0.75}O_{3-\delta}$. Based on this result, it seems that it is possible to exsolve Fe NPs from the B-site lattice, upto a limited concentration of 20% mol. The particle sizes of these exsolved NPs for the respective materials are presented in Fig. 4.1.11. The porosity of the samples were though very close to each other, and

the NPs maintained to cover around ~2.5% to ~2% of the area at the surface. The particle sizes for $LSCFe_{0.1}T_{0.9}O_{3-\delta}$ and $LSCFe_{0.18}T_{0.82}O_{3-\delta}$ are also very similar, whereas difference is observed in the case of $LSCFe_{0.25}T_{0.75}O_{3-\delta}$, which is mostly due to agglomeration of Fe NPs. For $LSCFe_{0.25}T_{0.75}O_{3-\delta}$, the exsolved Fe NPs tended to agglomerate, which resulted in their smaller number but much bigger in size particles (200-450 nm), presented in Fig. 4.1.12. There is some disagreement in the literature regarding the potential exsolution of Fe. $Sr_2Fe_{1.5}MoO_{6-\delta}$ was reported to be stable in reductive environments at high temperatures without showing any signs of metallic Fe nanoparticle exsolution by Lv and coauthors [53]. Whereas, from $Sr_2Fe_{1.5+x}Mo_{0.5}O_{6-\delta}$ (x = 0-0.1), a metallic Fe exsolution was obtained by Chen et al. [54]. To encourage the exsolution of Fe NPs of around 95 nm after 3 hours at 850 °C, the authors of that study raised the concentration of Fe on the B-site. It appears that due to thermodynamic un-favourability, which can be changed by compositional changes, Fe exsolution will be unlikely to occur in the absence of Fe excess [54]. A more thorough analysis of the exsolved Fe NPs size and distribution was performed and is presented in Fig. 4.1.13. These morphology of the materials were examined by an electron beam of 10 kV, therefore to reduce surface charging, and a thin layer of Au (10 nm) was deposited at the samples so as to reveal these true morphology of the reduced anode powders.

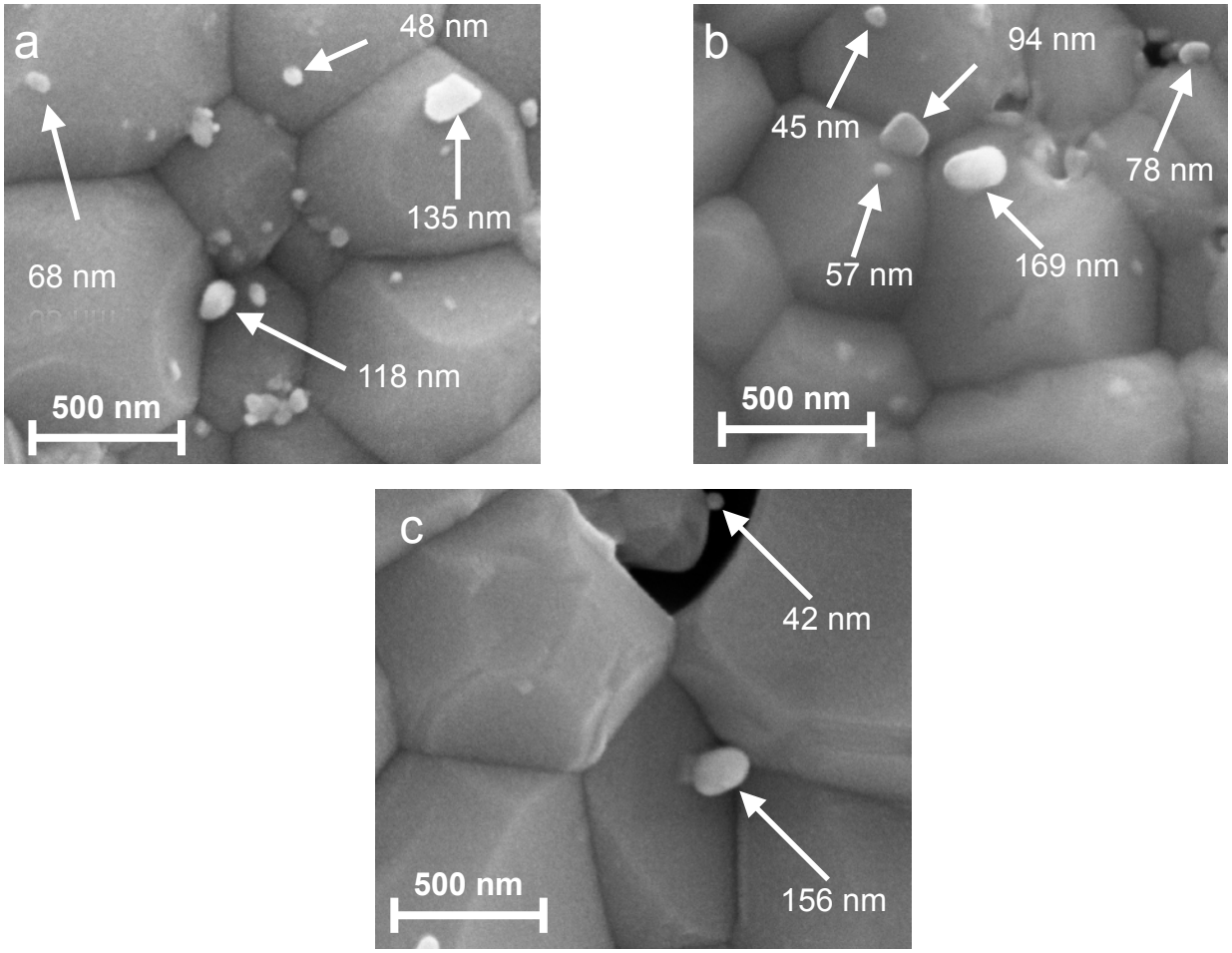

Fig. 4.1.11 Exsolved Fe NPs sizes in LSCFeT powders reduced at 900 °C in dry H_2 for 10 hours; Letters refer to different Fe content : a) $Fe_{0.1}$, b) $Fe_{0.18}$, b) $Fe_{0.25}$. Scale bar is 500 nm, Relative uncertainty of the NPs' size measurement is +/- 5%.

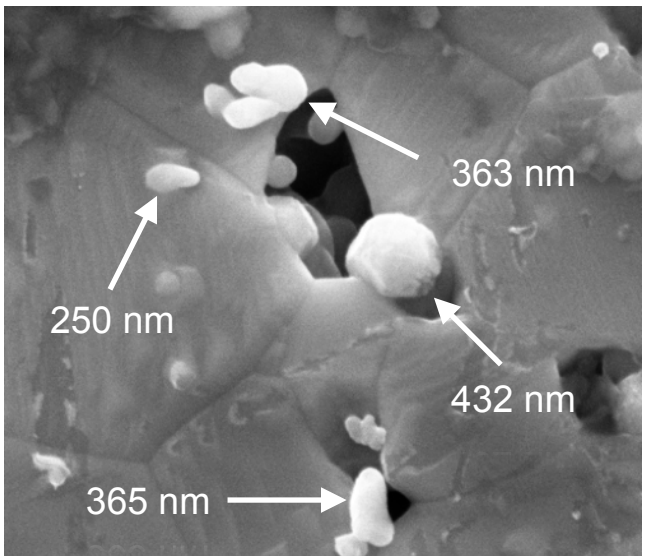

Fig. 4.1.12 Agglomeration of exsolved Fe NPs

in $LSCFe_{0.25}T_{0.75}O_{3-\delta}$

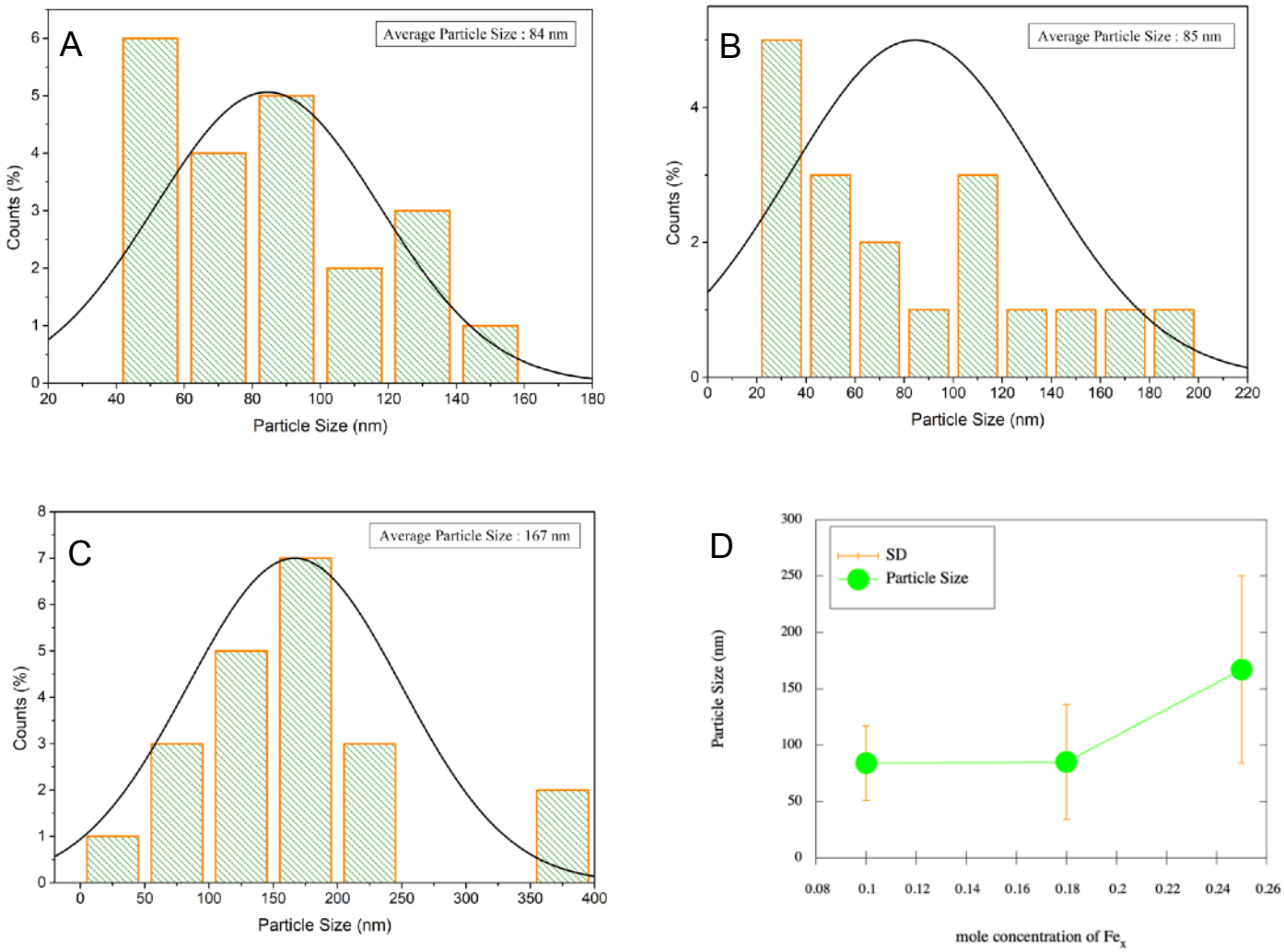

Fig 4.1.13. Particle size distribution of exsolved Fe NPs of $LSCFe_xT_{1-x}O_{3-\delta}$; A) x = 0.1, B) x = 0.18, C) x = 0.25, D) variation of the average particle size as a function of Fe_x content

On analysing the mean and standard deviation (SD) of these results, the average particle size of these exsolved Fe NPs were calculated. The results for $LSCFe_{0.1}T_{0.9}O_{3-\delta}$ and $LSCFe_{0.18}T_{0.82}O_{3-\delta}$ satisfies the findings from literature, e.g. Bochentyn et al. [5] that these exsolved NPs are very small (<50nm) when the reduction is done at temperature below 1000 °C, upon considering the exsolution of Fe NPs were proper. Generally, in reducing atmospheres and/or under specific voltage conditions with an A-site shortage, B-site metallic exsolution is more likely to occur [55]. The reduction process resulted in the production of oxygen vacancies, which may be related to the Fe exsolution, i.e by partial reduction of Fe^{3+} to Fe^{2+} in the perovskite anode powders and then to Fe^{0} as in exsolved nanoparticles. An estimate of this exsolved metal NPs composition can thus be calculated by noting that Fe (considering to be in Fe^{3+} electronic state) was reduced according to :

$$Fe_2O_3 \xrightarrow{H_2} 2Fe + 3/2\ H_2O \qquad \text{..... Eq. [2]}$$

Further reduction would cause the exsolution of B-site Fe when the lattice of LSCFeT could no longer accept any more oxygen vacancies. These oxygen vacancies after reduction will cause change in mass of the materials, which can be recorded with precisely performed Thermogravimetric analysis (TGA) measurement. TGA determines the endothermic and exothermic weight loss that occurs when nanoparticles are heated, cooled, etc. TGAs employ heat to compel chemical and physical alterations in the materials.

The results from SEM measurement compliments with the analysis of the XRD results, and suggests that it is possible to exsolve Fe NPs from the B-site lattice, to a concentration limit of nearly 20% mol. in the system. This results makes our materials $LSCFe_{0.1}T_{0.9}O_{3-\delta}$ and $LSCFe_{0.18}T_{0.82}O_{3-\delta}$, viable for producing electrodes of high catalytic activity with exsolved nanoparticles for SOFC's. The catalytic activity of such electrodes with exsolved nanoparticles, can be further tailored for the alteration of electronic properties with the incorporation of another dopant from the transition metal group, such as Ni or Co, with Fe on the B-site lattice.

Two important points learned from the above results about the exsolution phenomenon is that, (1) it requires a large driving force to bring the targeted element from the host structure to the surface of the material as metallic NPs, (2) Although each respective dopant elements has got a different degree of driving force thermodynamically. Thus, these points are needed to be considered for mastering the exsolution process effectively. Exsolved metal NPs, shows good catalytic activity as well as long term stability for fuel oxidation in SOFC anodes. The overall amount of exsolved NPs can be increased by extrinsic variables like oxygen partial pressure and temperature, but eventually the numbers are constrained by both the dopant concentration and the solubility limit in order to preserve the perovskite structure.

4.2 Exsolution of Alloy nanoparticles

4.2.1 Tailoring the catalytic activity of exsolved Fe NPs with Ni/Co

As anodes in SOFCs, perovskite oxides have a lot of potential because they work well for redox cycling and can operate with fuels other than hydrogen. Oxide anodes with reducible B-site transition metal cations are of great interest because, when exposed to reducing fuel, the reducible cation "exsolves" from the oxide onto the surface, where catalytic metal nanoparticles can improve the catalytic and electrochemical properties of the electrodes. Exsolved metal nanoparticles are frequently made of transition metals like Fe, Co, Ni, Ru, or Pd, or alloys like Ni-Fe and Co-Fe from perovskite oxides [11]. The above results indicated the possibility of exsolving metallic Fe nanoparticles on the surface of the material LSCFeT. A key factor in the design of perovskite oxides, particularly anodes with exsolved nanoparticles, is the stoichiometry. It has been shown that A-site deficiency promotes B-site metal exsolution [34]. Thus considering the composition of LSCFeT, Ni and Co was incorporated into the system separately on the B-site lattice along with the viable amount of Fe_x. Following the compositional stoichiometry, a series of 6 different materials were prepared doped with Ni and Co.

Table 4.2.1 Series of Anode Powders composition

$La_{0.27}Sr_{0.54}Ce_{0.09}Fe_xNi_yTi_{1-x-y}O_{3-\delta}$	Abbreviation $LSCFe_xNi_yT$	$La_{0.27}Sr_{0.54}Ce_{0.09}Fe_xCo_yTi_{1-x-y}O_{3-\delta}$	Abbreviation $LSCFe_xCo_yT$
$La_{0.27}Sr_{0.54}Ce_{0.09}Fe_{0.1}Ni_{0.1}Ti_{0.8}O_{3-\delta}$	$LSCFe_{0.1}Ni_{0.1}T$	$La_{0.27}Sr_{0.54}Ce_{0.09}Fe_{0.1}Co_{0.1}Ti_{0.8}O_{3-\delta}$	$LSCFe_{0.1}Co_{0.1}T$
$La_{0.27}Sr_{0.54}Ce_{0.09}Fe_{0.1}Ni_{0.2}Ti_{0.7}O_{3-\delta}$	$LSCFe_{0.1}Ni_{0.2}T$	$La_{0.27}Sr_{0.54}Ce_{0.09}Fe_{0.1}Co_{0.2}Ti_{0.7}O_{3-\delta}$	$LSCFe_{0.1}Co_{0.2}T$
$La_{0.27}Sr_{0.54}Ce_{0.09}Fe_{0.2}Ni_{0.1}Ti_{0.7}O_{3-\delta}$	$LSCFe_{0.2}Ni_{0.1}T$	$La_{0.27}Sr_{0.54}Ce_{0.09}Fe_{0.2}Co_{0.1}Ti_{0.7}O_{3-\delta}$	$LSCFe_{0.2}Co_{0.1}T$

Co-based perovskites exhibit enhanced oxygen reduction activity and electronic/ionic conductivity. However, Ni-based perovskites are also studied since Co-based perovskites are quite expensive due to a high cost of Co and a larger thermal expansion coefficient than other SOFC components. Ni is typically chosen as the active anode material for most SOFC studies and applications due to its high catalytic activity and low cost. To create a porous cermet microstructure, it is typically used as a sintered composite mixture of fine grain NiO powder in an ionically conducting oxide matrix, such as YSZ. Most studies of exsolution anodes have focused on how exsolved nanoparticles impact electrochemical performance, but the final composition and phase structure of the oxide should also play an important role. The final oxide composition is determined by the initial perovskite stoichiometry and the amount of metal exsolved from the lattice to the surface of the material [56]. The materials employed in each component, i.e cathode and anode, play a key role in determining the performance of any SOFC. Electrodes are significant active areas in which electrochemical

processes take place. The level of electronic and ionic conductivity, as well as catalytic activity, are elements that affect the SOFC's performance in terms of metrics like power density and energy conversion efficiency.

4.2.2 Synthesis of Powders

The perovskite materials of $LSCFe_xT$ (x = 0.1, 0.2), doped with Ni_y and Co_y (y = 0.1, 0.2) respectively were prepared in the similar Pechini method sol-gel process. During the preparation of the materials, the same precursors were considered as before, along with metal nitrates of Ni and Co, for the respective materials, which were - $Ni(NO_3)_2.6H_2O$ (Sigma-Aldrich) and $Co(NO_3)_2.6H_2O$. The respective solutions with combined precursors were continuously stirred with a rotational speed of 250 rpm and were heated up to 100 °C, until the organic resin is formed with homogeneously distributed cations, because of the slow evaporation of the solvent, turning it up to a wet-gel. The stoichiometry of these series of samples are presented in Table 4.2.1. The prepared gels were then calcined under an atmospheric environment with the similar temperature profile, as earlier.

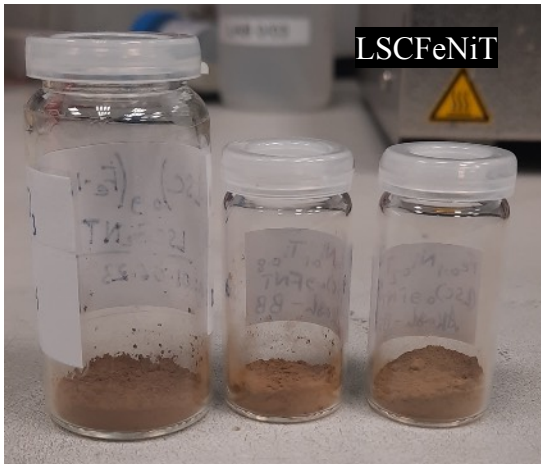

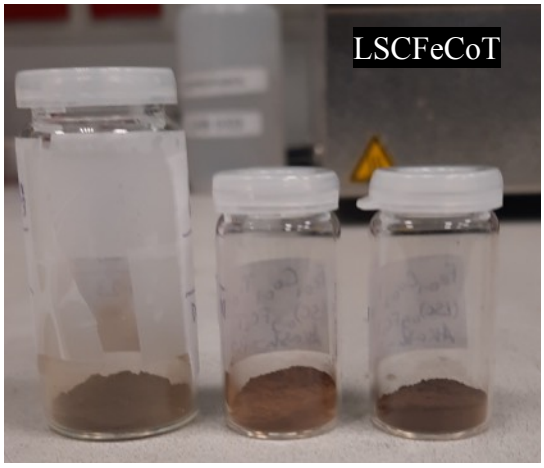

Fig. 4.2.1 Photos of as-prepared LSCFeT-based powders containing Ni (left) and Co (right) as a second metal dopant

These calcined anode powders were then grinned in a mortar for having homogenous materials for further steps of the experiment. XRD was performed for two sets of powders: as-prepared and after reduction in dry H_2 at 900 °C for 10 hours. The morphology of the samples was observed using the same SEM instrument. All SEM samples were examined with an acceleration voltage of 20 kV electron beam in a high vacuum mode. To prevent surface charging a thin layer of Au was deposited at the materials surfaces so as to reveal the true morphology.

4.2.3 Phase evolution of perovskite oxides

The as-prepared anode powders were analysed by XRD in order to examine the evolution in the phase formation after reduction of the materials. The results are presented in Fig.4.2.2. The strong sharp diffraction peaks in the XRD pattern relate to cubic perovskite structure of $SrTiO_3$. In the LSCFeNiT, a presence of two dopants in the B-sublattice (Ni and Fe) resulted in the formation of secondary phase $NiFe_2O_4$. Whereas, Fe_3O_4 was present in the XRD pattern of LSCFeCoT. Other secondary phases present in the powders were CeO_2 and $La_{0.6}Sr_{0.4}FeO_3$.

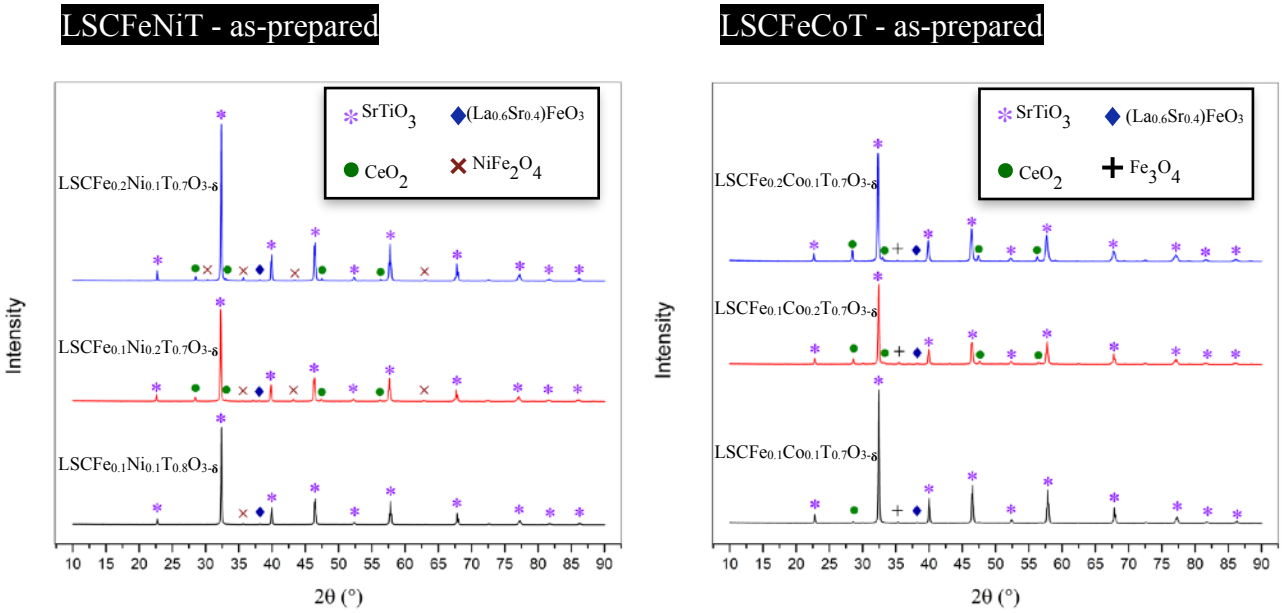

Fig. 4.2.2 XRD patterns of the as-prepared LSCFeT-based powders with additional metal dopants

After reduction in dry H_2 at 900 °C for 10hrs, some evolution of phases was observed in the materials as compared to the phases present before reduction. The results are presented in Fig. 4.2.3. All the strong diffraction peaks, for the materials remained to maintain the perovskite structure of $SrTiO_3$ as primary phase, with a cubic crystal structure. The presence of this phase in the structure is strongly related to the non-stoichiometry of strontium (Sr/Ti < 1 in $SrTiO_3$), what was previously reported in the literature [57]. This indicates the presence of strontium vacancies in the materials. Mixed valence Fe cations partially substitute Ti^{4+} ions in the centre of oxygen octahedra. It is evident that two types of bimetallic dopants does not have any significant effect on the chemical structure of the samples. After reduction, a $Ni_{1-x}Fe_x$ alloy, is formed via exsolution from the LSCFeNiT perovskite. Given that Fe and Ni are next to one another in the periodic table, it is easy for them to combine in different ratios to form a solid solution phase. Considering the theoretical phase diagram of Ni-Fe, at least one common alloy with the chemical formula Ni_3Fe was capable of forming under these experimental conditions. However, under the same circumstances, alloys made of NiFe, Ni_3Fe_2, and Ni_2Fe have also been produced [58]. An earlier study showed that once H_2 was treated, a large portion of iron on supported catalysts may be alloyed with nickel. Therefore, it can be concluded that the alloy production under the conditions of this experiment is advantageous.

A similar phase characteristic of alloy structure was observed for LSCFeCoT reduced anode powders. The main identified phase was a $SrTiO_3$ perovskite structure. Moreover, some traces of CeO_2 were noticed, the

same as for the LSCFeNiT sample after reduction. In the case of sample containing 10 mol.% of Fe, also some peaks recognised as Co-Fe cubic crystal structure were identified. For sample containing 20 mol.% of Fe, small peaks attributed to Fe-Ti phase were found. Having the almost same diffraction peaks after calcination in air, and reduced in dry H_2 at 900°C, it indicates that the anode powders of LSCFeNiT and LSCFeCoT perovskite structures have good stability. The diffraction peaks of Ni-Fe and Co-Fe reflects the in-situ exsolved NPs from the backbone of these perovskite anode powders.

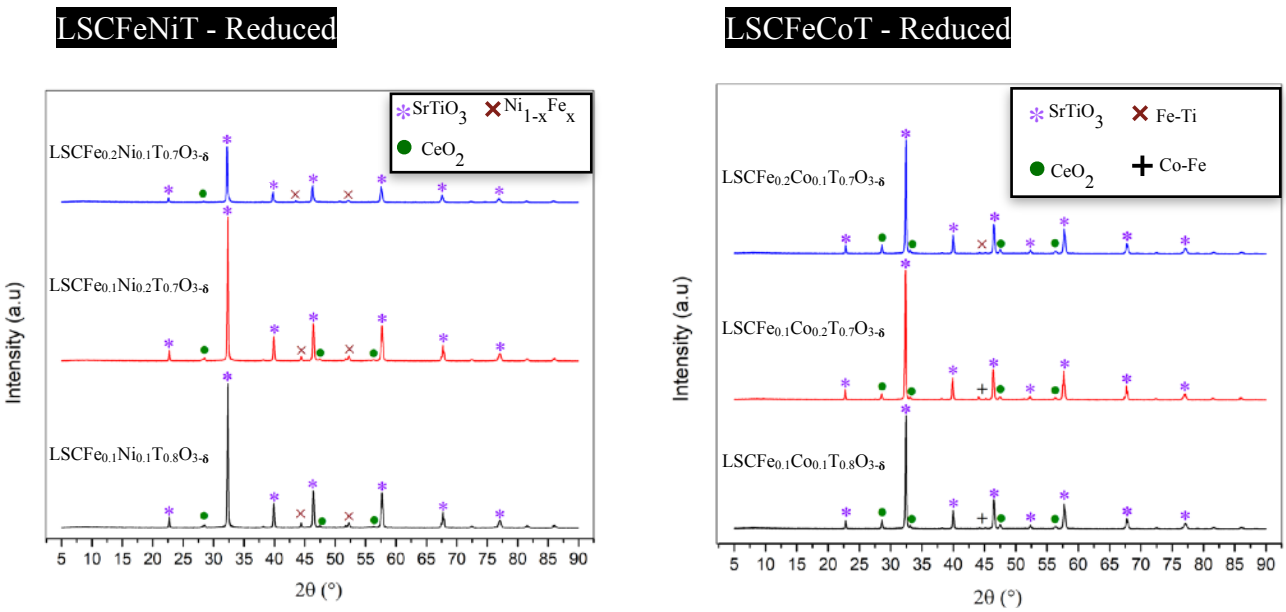

Fig. 4.2.3 XRD patterns of the reduced LSCFeT-based powders with additional metal dopants

An evolution in the phase from Fe_3O_4 to Co-Fe was seen in LSCFeCoT after being reduced. This crystal structure of Fe_3O_4 can be explained by dense planes of oxygen anions with iron cations in octahedral or tetrahedral interstitial locations. The oxygen ions in magnetite (Fe_3O_4) are arranged in a close-packed cubic configuration, with Fe^{3+} randomly distributed between octahedral and tetrahedral sites, and Fe^{2+} in octahedral sites, magnetite possesses an inverted spinel structure [59]. There was an absence of crystalline cobalt containing phase after calcination, which might be due to its low concentration in the lattice. But with reduction, it enters into the existing crystalline phase of magnetite, by forming an independent crystalline phase of Co. The phase of Co-Fe is isostructural with magnetite and crystallises in the space group Fd-3m cubic typical spinel structure, which comprises cobalt ions in the oxidation states Co^{2+} and Co^{3+} [60]. There is evidence in the literature, nevertheless, that Fe can be exsolved in LSCF-based material, where Fe^0 is reduced from Fe-oxide phases, even though having a low phase fraction.

Even the intense peak of $SrTiO_3$ shifted towards the lower **2θ** angles for these anode powders after reduction, highlighting the increase in the unit cell size and a bit of lattice distortion. In LSCFeNiT, the shift of this XRD diffraction peak was seen to be depending on the concentration of Fe, as Ni was easily exsolved from the backbone to surface of the material, and these exsolved NPs will be seen while studying the morphology of the surface with SEM measurements, whereas the concentration of Co was being responsible for the shift for LSCFeCoT. In addition to this, the observation with the peak shift in Ni-based material satisfies the hypothesis from literature, that when Ni doping is increased, the reflections shows a gradual shift to higher **2θ** angles [61], which have been the case for $LSCFe_{0.1}Ni_{0.2}T_{0.7}O_{3-\delta}$.

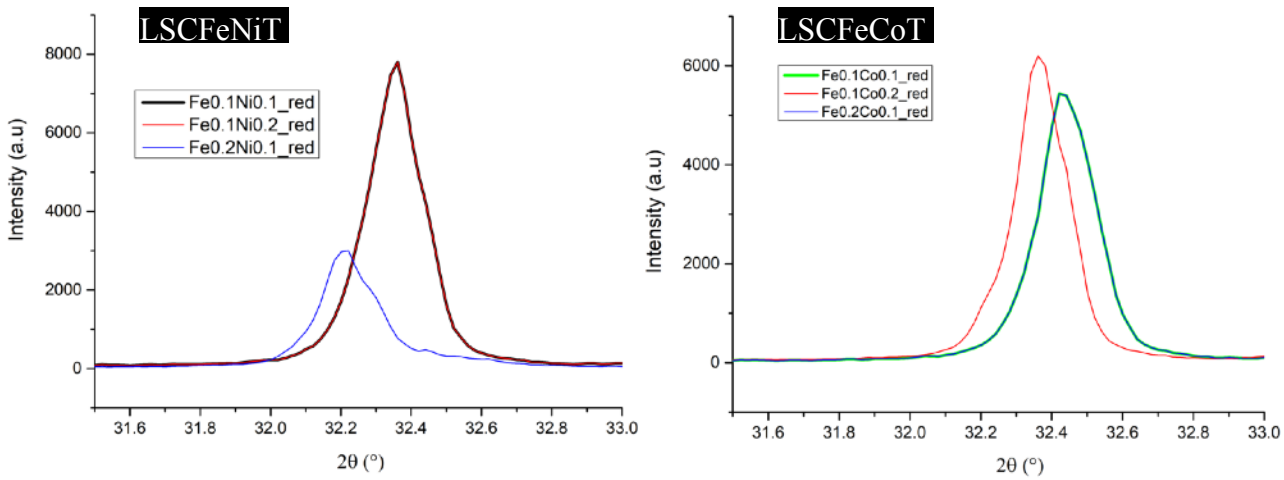

Fig. 4.2.4 Comparison of the most intensive XRD peak in results of materials after reduction, (left) LSCFeNiT, (right) LSCFeCoT

Table 4.2.2 Unit cell parameters of LSCFeT-based powders with additional metal dopants with Rietveld refinement parameters

B-site cations	Peak Position of as-prepared materials 2θ (°)	Unit cell Parameter (a=b=c)	Unit cell Volume [Å³]	Peak Position of reduced materials 2θ (°)	Unit cell Parameter (a=b=c)	Unit cell Volume [Å³]	Goodness of Fit (GoF)
$Fe_{0.1}Ni_{0.1}$	32.37	3.906	59.593	32.34	3.913	59.905	2.902
$Fe_{0.1}Ni_{0.2}$	32.26	3.907	59.648	32.35	3.913	59.916	3.659
$Fe_{0.2}Ni_{0.1}$	32.35	3.909	59.719	32.20	3.912	59.883	2.352
$Fe_{0.1}Co_{0.1}$	32.42	3.905	59.562	32.45	3.916	60.063	2.236
$Fe_{0.1}Co_{0.2}$	32.39	3.914	59.965	32.36	3.920	60.236	3.853
$Fe_{0.2}Co_{0.1}$	32.29	3.907	59.648	32.42	3.910	59.777	3.635

Generally, the substitution of Ni/Co with Fe on the B-site, will lead to increase the unit cell size because both has larger atomic radius than Fe. The addition of Ni^{2+} (0.69 Å) having larger ionic radius than Fe^{3+} (0.645 Å), will increase the unit cell size, hereby causing the diffraction peaks to shift towards left. On doping LSCFeT with lower valence cations of Ni may transform Fe^{3+} into Fe^{4+} (0.585 Å) and hence forming oxygen vacancies so as to maintain being electrically neutral. These large amount of oxygen vacancies are beneficial for oxygen ion conductivity and catalytic activity [62]. A detailed summary on the peak positions and their shift, thus causing the change in the unit cell parameters is presented in Table 4.2.2. The unit cell parameters for the samples before and after reduction were studied with Rietveld refinement method. Also a distinctive change was seen for the crystallite sizes calculated with Scherrer equation. The Ni-based material and Co-based material had the crystallites of average sizes 100 nm and 110 nm respectively, which dropped down to

88 nm after reduction. Since there will also be lattice distortion after reduction due to the shift of the peak, therefore even a change on the lattice strain was witnessed to increase from 0.165% to 0.209% for Ni-based anode powders, and 0.131% to 0.188% for the Co-based anode powders.

The samples that were treated in a reducing environment in situ, shows a tendency to form metallic nanoparticles via exsolution process. According to the theory, the Ni^{2+} and Fe^{3+} or Fe^{2+} are synchronously reduced to Ni^0 and Fe^0, which are then, respectively, anchored to the surface of the perovskite. The presence of Fe in the bimetallic A-LSC (A-site deficiency Lanthanum Strontium Cerium) perovskite material, enhances its reducibility property. During the production of the alloy, metallic Ni and metallic Fe aggregate concurrently. However, the XRD measurements of reduced powders revealed a few notable diffraction peaks that may be attributable to Ni and Fe. Based on the literature reports, when increasing the Ni doping on the B-site lattice of LSCF-based material, the ratio of Fe^{4+}/Fe^{3+} is increased, since Fe tends to obtain the +4 oxidation state, in order to attain the electronically neutral state. From literature it was studied, that in case of reduction in LSCF-based materials Fe^{3+} and Fe^{4+} reduces to lower valency cations. On incorporating Ni into the B-site lattice of LSCF-based materials, Ni^{2+} can get reduced to Ni^0. The amount of oxygen, that the perovskite had lost increases with the amount of Ni integrated into the lattice, due to further reduction of the Ni^{2+} species. This explains why the perovskite had a greater oxygen shortage when the Ni doping in LSCF-based materials is increased, which in turn increases the exsolution of Fe-Ni nanoparticles. Exsolved Fe–Ni alloys are often used as cathodes for CO_2 or steam electrolysis due to their high catalytic activity, good stability under cell operation conditions, and resistance to carbon deposition and nanoparticle sintering. This is because of the exsolved particles' well-known strong anchorage on the support.

In the LSCFeCoT reduced at 900 °C, the impurity $(Co, Fe)_3O_4$ spinel phase (Fd3m), arises with low phase fraction, which might be the result of a slow rate of cation reincorporation into the perovskite lattice. No other secondary phase is found following the reducing procedure, with the exception of the Co-Fe alloy in FCC structure and the Fe metal/Co-Fe alloy in BCC structure as the exsolved species. The difference in the unit cell volumes for these series of materials before and after reduction, is although not very large, and that could be attributed to differences in the charge-balance compensation and minor perturbations of the unit cell through the formation of oxygen vacancies or valence compensation by the B-site metals [63]. Similar to the Fe-Ni bimetallic exsolved NPs, exsolution of Fe-Co nanoparticles has also been extensively explored. Typically used as anode materials for SOFCs, they exhibit a variety of promising qualities including high activity, stability, coking resistance, and sulphur tolerance. The performance of the initial perovskite gets improved by the exsolution of Fe–Co alloy nanoparticles, which improves the kinetics of the electrode reactions and enables charge separation and ionic conduction [64]. Notably, a phase change of the perovskite substrate can occasionally accompany the exsolution of metallic or bimetallic nano-particles. Both factors are crucial for defining the SOFCs' anode performance since the oxide substrate affects the channel for electron/ion conduction while the exsolved nanoparticles typically contributes to its high catalytic activity. In literature, it was revealed that co-doping with Fe and Co probably enhances the hybridisation of orbits of transition metal and oxygen, thus giving rise to an increased conductivity of the material [65]. Although, it was also depicted that extreme reduction conditions, which encourages the exsolution of Fe-Co bimetallic NPs and the phase transition of the perovskite substrates, can also lead to lower down its catalytic performance, hence a phase transition of the substrate is not always advantageous [66].

4.2.4 Morphology of the exsolved nanoparticles

The morphology of LSCFeT-based powders with additional metal dopants was analysed with SEM measurements. The measurement was conducted on the materials after reduction, as obviously no metallics NPs could have been found deposited at the surface for the materials before reduction (as-prepared). On examining the images, it was seen that probably Fe-Ni alloy NPs and Fe-Co alloy NPs were exsolved and socketed uniformly at the surfaces of these series of materials. Exsolved alloy NPs were very well dispersed around the surface and were clearly distinguishable between Fe and Ni/Co NPs, as compared to the exsolution of LSCFeT, exsolved Fe NPs were of irregular shape. Ni/Co were all in perfect spherical shapes and very well distributed on the edges as well.

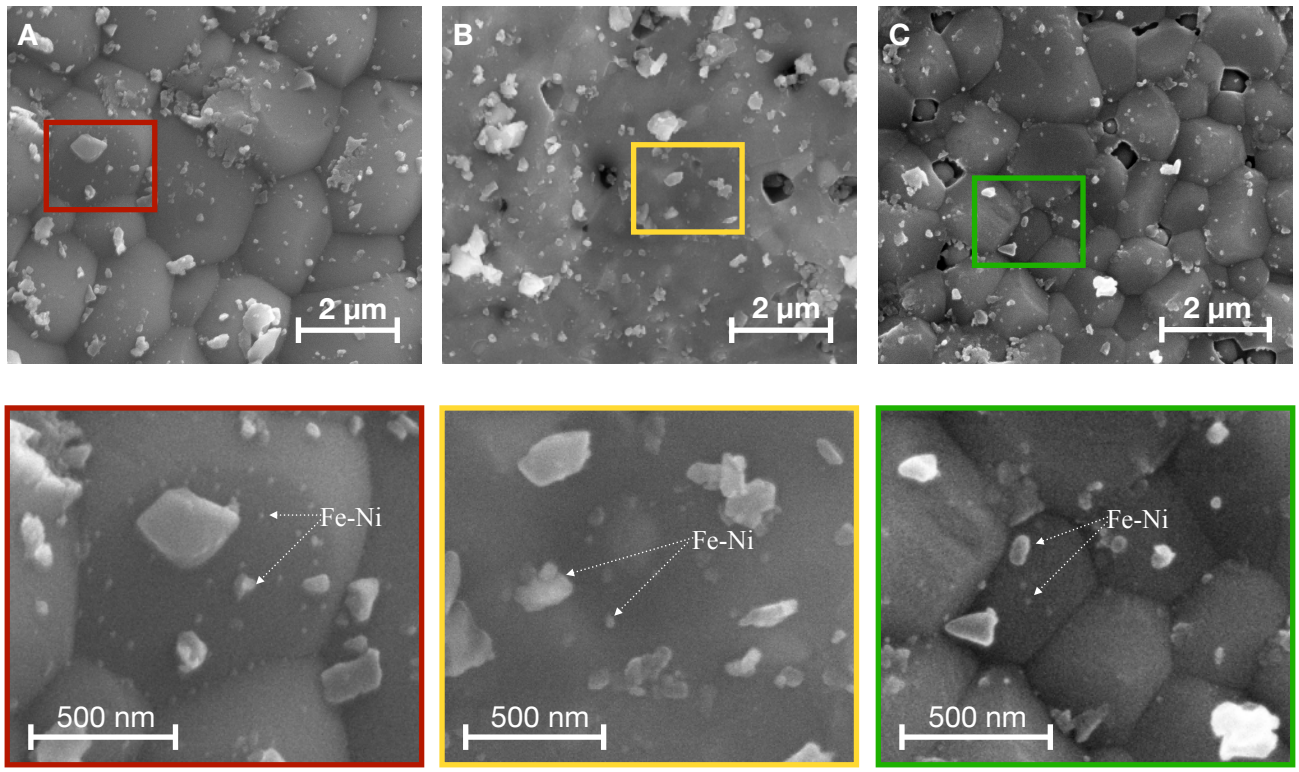

Fig. 4.2.5 SEM images of LSCFeNiT anode powders reduced at 900 °C in dry H_2 for 10 hours. a) $Fe_{0.1}Ni_{0.1}$, b) $Fe_{0.1}Ni_{0.2}$, b) $Fe_{0.2}Ni_{0.1}$. Scale bar is 2 µm, and 500 nm. Relative uncertainty of the NPs' size measurement is +/- 5%.

Powder samples often have inclined and uneven surfaces, whereas bulk sample provides more precise observation of the morphology evolution of NPs [67]. The size of the NPs from exsolution strongly depends on the annealing temperature. Larger NPs size on the reduced samples suggests higher particle growth rate is induced by the annealing temperature [67], which was seen to happen with Fe NPs in case of alloy exsolution. The particle size of the NPs was calculated separately, for irregular shape particles, and spherical shape particles for the different set of samples. In case of LSCFeNiT, the size of the spherical shaped particles were found to be around 35+/-6 nm uniformly distributed on the oxide surface, and the size of the irregular shaped particles were around 110+/-20 nm.

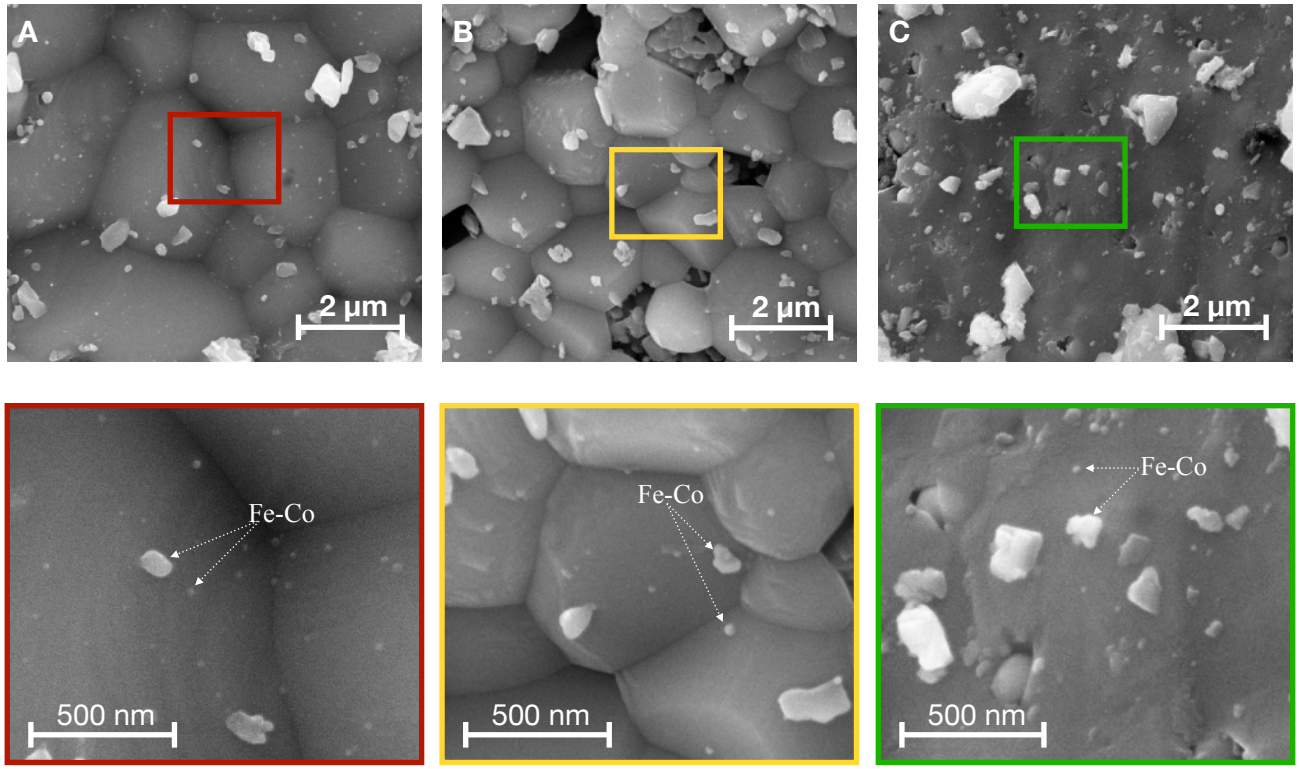

Fig. 4.2.6 SEM images of LSCFeCoT anode powders reduced at 900 °C in dry H_2 for 10 hours. a) $Fe_{0.1}Co_{0.1}$, b) $Fe_{0.1}Co_{0.2}$, b) $Fe_{0.2}Co_{0.1}$. Scale bar is 2 µm, and 500 nm. Relative uncertainty of the NPs' size measurement is +/- 5%.

Whereas for LSCFeCoT, these particle sizes were around 29+/-2 nm and 97+/-5 nm respectively. As this irregular shape particles are larger in size than those of uniform spherical particles, it can be concluded that it is because of the agglomeration tendency which Fe has got. A dispersion of nanoparticles strongly anchored to grain surface is produced by the exsolution process. The increased connection with the support reduces the aggregation of nanoparticles [68]. The presence of spherical shape NPs with wide distribution over the oxide surface is readily because of Ni and Co respectively in the different set of materials, as Ni and Co are more readily reducible than Fe. Kobsiriphat et al. [69] reported that an amorphous surface layer surrounds the particle, which has a roughly spherical free surface. A similar observation for exsolved Ni nanoparticles was explained by the production of a native oxide following exposure of the anode to air. The amount of Fe in the exsolved NPs seems to increase for the material $LSCFe_{0.1}Ni_{0.2}T_{0.7}O_{3-\delta}$, and decrease for the material $LSCFe_{0.2}Ni_{0.1}T_{0.7}O_{3-\delta}$, as compared with $LSCFe_{0.1}Ni_{0.1}T_{0.8}O_{3-\delta}$. The porosity of the anode powders was estimated using the ImageJ program, and it indicated $LSCFe_{0.1}Ni_{0.1}T_{0.8}O_{3-\delta}$ being more porous with exsolved alloy NPs as compared to $LSCFe_{0.2}Ni_{0.1}T_{0.7}O_{3-\delta}$. These exsolved alloy NPs covers ~7% of area for $LSCFe_{0.1}Ni_{0.1}T_{0.8}O_{3-\delta}$, ~5.5% for $LSCFe_{0.1}Ni_{0.2}T_{0.7}O_{3-\delta}$, and ~4% for $LSCFe_{0.2}Ni_{0.1}T_{0.7}O_{3-\delta}$. However, for Co-based materials it was ~3.5% for $LSCFe_{0.1}Co_{0.1}T_{0.8}O_{3-\delta}$, ~5% for $LSCFe_{0.1}Co_{0.2}T_{0.7}O_{3-\delta}$, and ~7.5% for $LSCFe_{0.2}Co_{0.1}T_{0.7}O_{3-\delta}$.

The Co-Fe alloy are thermodynamically favourable to be generated under the anode operation condition, i.e. in H_2 containing atmosphere and at temperatures between ~600-1000 °C, which is similar as Ni-Fe [70]. The morphology of these anode powders shows these irregular shaped agglomerates with sizes around ~100 nm which were formed during the sintering of the powders due to high reactivity. Particle agglomeration is a frequent characteristic of materials made using the Pechini method. In the Pechini process, the thermal decomposition step (calcination) is occurred when a significant amount of weight is lost and strong agglomerates develop. The production of partially sintered agglomerates is caused by the decomposition of organic material during calcination, which might supply extra combustion heat. Therefore, the morphologies of their resin intermediate play a major role in determining the form and particle size of oxide powders produced by a Pechini-type process [71]. The basic prerequisite for creating fine-grained and nano-agglomerated powder is always a soft and porous resin intermediate, although it is not always sufficient. The following processing parameters must be properly controlled. These include the water content in the combination, the pulverisation before sintering, the sintering conditions, and the mass ratio of the polymeric gel (CA:EG) to chlorides [72]. The exsolved Fe-Ni/Co alloy NPs with various range of ratios from this different perovskite structured materials is being reported here. A discrepancy was noticed between the results in this study with the literature, which confirmed that two elements exsolve as an alloy and not as two separate type of particles. The same was noticed in the SEM images from literature. Whereas, the SEM images for this study has been completely different from that of the literature, showing two different particle types were exsolved, (1) regular nano spheres, and (2) irregular shape particles. From the SEM measurements of LSCFeT material, it was seen how the exsolved NPs (probably Fe) look like on the surface, and that similarity was seen with the irregular shape particles for these series of LSCFeT-based powders with additional metal dopants. Although the size of these exsolved NPs satisfies the results from the literature. Based on that the hypothesis can be put that probably two elements were exsolved as two separate metals and not together as an alloy composition. This discrepancy of the result with the literature, may be because of the difference in the reduction temperature and time. In literature, such studies were mostly conducted at ~700-800 °C. However, the accuracy of the composition of these exsolved NPs, whether they are two separate metals or bimetallic NPs, that can be confirmed with the help of EDS analysis. Overall, the exsolved alloy nanoparticles were richer in Ni than Fe for all of the LSCFeNiT compounds. This was due to the fact that, according to Neagu et al.'s [33] calculation, the Gibbs free energy of reduction of NiO to Ni is smaller than that of Fe_2O_3 to Fe. As a result, the reduction of Ni^{2+} to Ni^0 occurred more readily than the reduction of Fe^{3+} to Fe^0.

However, in light of the Ti-based perovskite oxides' favourable structural stability in the SOFC's anodic state was observed for these series of LSCFeT-based powders with additional metal dopants. XRD results demonstrated that the modest doping of Ni/Co and Fe at the B-site of A-site deficient LSCT, did not change the original crystal structure of $SrTiO_3$. SEM resulted to, impressively produced nanoparticles socketed at the surface, which can raise the concentration of active sites, promoting the electrochemical reactions that take place on the surface of LSCFeNiT/LSCFeCoT during operation, hence improving the catalytic property of these anodes for SOFCs.

5. Current challenges faced today in research of exsolution

Exsolution along with the generation of different metal/alloy NPs on the perovskite surface opens up new possibilities for controlling the electrochemical properties for different electro-catalytic reactions and creating functional nano-composite oxides with tailored functionalities to satisfy various requirements in a variety of energy-related applications. Despite these unmatched benefits, there are still four significant problems with the metal exsolution engineering of perovskites.

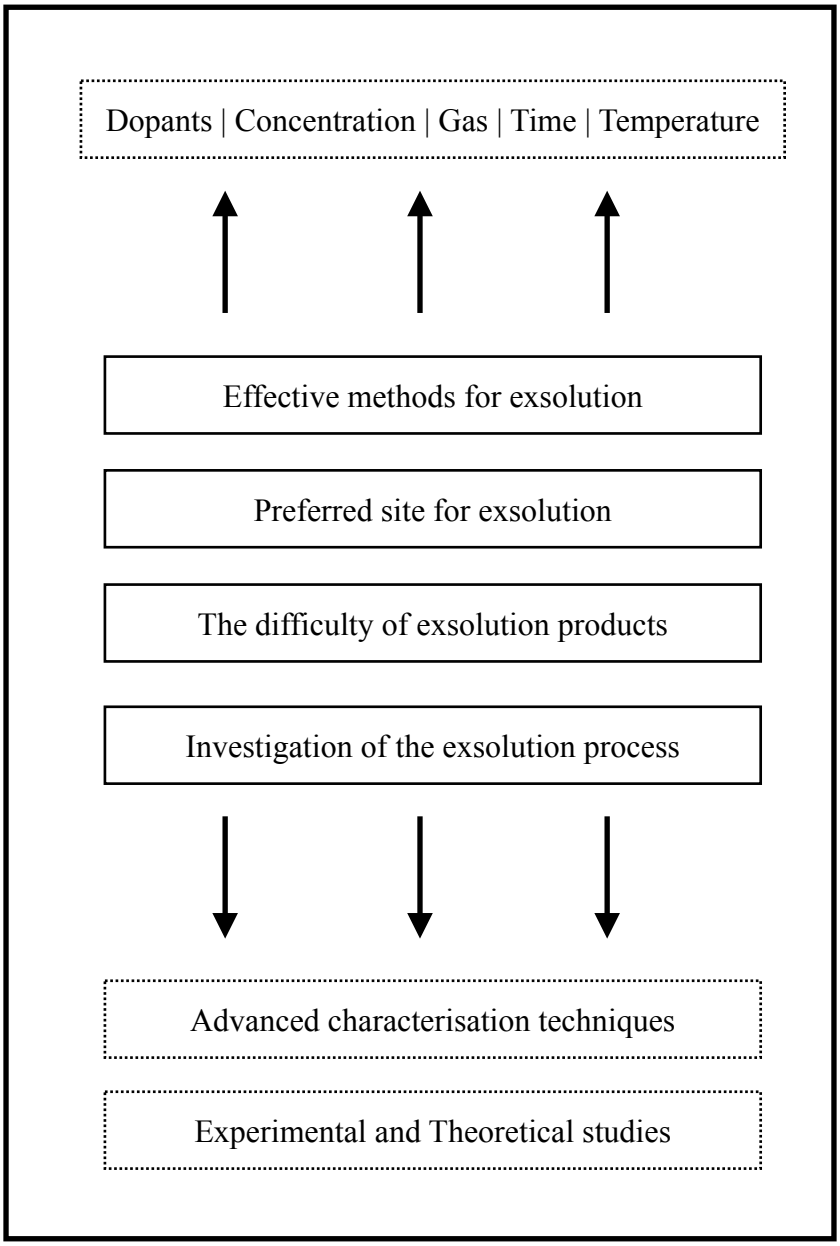

Fig. 5.0.1 Current challenges for exsolution

5.1 Effective methods for exsolution

High temperature (>700 °C) is necessary for effective exsolution in order to break through the thermal activation barrier and enable effective ion transport inside perovskites and effective catalysis. Additionally,

the traditional gas-based reducing methods for exsolution require a lot of energy and time (a few to tens of hours), which may lead to the exsolved NPs being very large in size and the host materials being destroyed during the lengthy thermal annealing process. Therefore, it is crucial to create novel exsolution processes that either use lower temperatures or require shorter reaction times. Additionally, a modest quantity of B-site dopant (10 mol.%) is used in the synthesis of the majority of parent perovskites for metal exsolution [73]. It has been established that the morphology and crystal structure of the exsolved NPs are clearly influenced by the doping concentration of the exsolved elements in the parent perovskites, which has an impact on the catalytic activity. Low metal usage ratios are a result of the limited exsolution of doping cations and the majority of the cations remaining in the parent perovskite lattices. In contrast, a high rate of ion loss during exsolution can result in host materials becoming structurally unstable.

5.2 Preferred site for exsolution

Metal NPs may be exsolved from the parent perovskites' A-site in addition to the frequently studied exsolution from B-site species [74]. Unfortunately, the ideal exsolution site and the underlying motivation remain unknown. As grain boundaries and stacking defects are thought to be much easier to form than these defect-free sites, it has been postulated that the exsolution of NPs occurred preferentially at these defective sites [75]. Some reversible spots may be created when the exsolved NPs migrate back into the parent perovskite as a result of oxidation. In order to give preferred exsolution locations for boosting exsolution and at the same time inhibit the deleterious A-site cations segregation, the reaction conditions should be thoroughly researched.

5.3 Exsolution product complexity

Co, Fe, and Ni have all been exsolved from the perovskites in order to greatly improve the catalytic property of the underlying perovskite catalysts. A reduction transition between the metal (or alloy) and the metal oxide (or ions), which is driven by the thermodynamic Gibbs free energy shift (ΔG) , is typically necessary to accomplish predicted exsolution. Some metals are stable below 900 °C ($\Delta G>0$), including La, Ba, and Sr. Over 600 °C, the majority of transition metals, including Co, Fe, and Ni, are easily reduced ($\Delta G<0$). The exsolution of Fe typically demands a higher temperature than that of Ni and Co. It should be noted that under certain reducing conditions, not all metal exsolution processes are thermodynamically advantageous.

5.4 Investigation of the exsolution process

Clarifying the physical and chemical alterations of both the exsolved NPs and the parent perovskites during exsolution, under external manipulation conditions, is the primary objective of the exsolution process investigation. For the purpose of elucidating the underlying exsolution mechanism, some in situ characterisation techniques, such as XRD, SEM, TEM, EDS, XPS, can provide direct and useful information regarding the structural changes of the exsolved NPs and the parent perovskites at various temperatures, potentials, concentrations, strains. In addition to experimental methods, theoretical simulations and calculations methods, such as the newly developed machine learning method, DFT are effective resources for gaining in-depth understanding and interpreting experiment results on exsolution.

6. Conclusion

In this thesis report, a novel anode candidate of Fe-based perovskite material for SOFCs was developed. as $La_{0.27}Sr_{0.54}Ce_{0.09}Fe_xTi_{1-x}O_{3-\delta}$ (LSCFeT). In this ceramic material, in-situ metal exsolution of the cation from the B-site lattice was investigated. Previous studies from literature has indicated, that it is difficult to exsolve Fe NPs as compared to other transition metals such as Ni, Co, Cu, Pt, Pd. Theoretical studies and calculations has explained that the mechanism of metal exsolution depends on the co-segregation energy of the metal, which drives it to exsolve out from the lattice structure upon reduction and gets socketed at the surface of the material as NPs. Through different research works, it was studied how this mechanism enhances the catalytic property of the anode materials for their performance in electrochemical work. Well, not only enhances the performance of the anode in SOFCs, but also increases its power density and long term stability. Ni and Co has contributed very promising results for this mechanism, but considering the cost of Fe, it will be feasible to use it over other metals. Therefore, it makes the challenge of this work to exsolve Fe nanoparticles or Fe-containing alloys a valid research problem to be studied.

In the master thesis' project the $LSCFe_xT$ was synthesised, where x was equal to 0.1, 0.18 and 0.25. Before studying the electrochemical performance and electrical conductivity of such materials for operation in SOFCs, it is important to consider that the anode materials maintain a stable perovskite structure even after reduction. Therefore, in this work the structural stability of such anode materials with Fe as the B-site cation to be exsolve was explored. The answer for this research problem was based mostly on XRD and SEM measurements. After successfully determining the best concentration of Fe, that can possibly be exsolved from the B-site of LSCFeT perovskite after reduction in dry H_2 at 900 °C for 10 hours, new materials with Ni and Co as the added dopants into the B - sub lattice with Fe_x respectively were prepared. The following materials were - $La_{0.27}Sr_{0.54}Ce_{0.09}Fe_xNi_yTi_{1-x-y}O_{3-\delta}$ (LSCFeNiT), and $La_{0.27}Sr_{0.54}Ce_{0.09}Fe_xCo_yTi_{1-x-y}O_{3-\delta}$ (LSCFeCoT). The possibility and efficiency of nanoparticle exsolution, both in the form of single metal as well as in the form of alloys were investigated based on these ceramic materials.

The XRD measurements indicated, that the materials maintained a stable and reliable perovskite structure of $SrTiO_3$, after reduction. Meanwhile, excellent results of the exsolved NPs were observed from SEM measurements. Fe exsolved from B-site of an A-site deficient perovskite, with NPs of sizes ~50 nm. The SEM measurements of LSCFeT-based materials doped with second metal (Ni or Co) shown the formation of two different structures on the grain surface: (1) uniform nano-spheres, (2) irregular shaped particles. However, the composition of these structures were not recognised, as the size of precipitates was below the resolution of EDX method accessible on site. In order to determine if the formed particles are single metals or alloys (i.e inter-metallic compounds) the TEM with EDX method may be useful. Finally, studying the catalytic property of these materials with the exsolved NPs, using the catalytic reactor or EIS measurements when used in electrochemical cells will add a valuable knowledge about the application potential of the synthesised materials.

References

1. N. (n.d.). *Annual 2001 Global Climate Report | National Centers for Environmental Information (NCEI)*. Annual 2001 Global Climate Report | National Centers for Environmental Information (NCEI). https://www.ncei.noaa.gov/access/monitoring/monthly-report/global/200113
2. Graves, C., Ebbesen, S. D., Mogensen, M., & Lackner, K. S. (2011, January). Sustainable hydrocarbon fuels by recycling CO 2 and H 2 O with renewable or nuclear energy. *Renewable and Sustainable Energy Reviews*, *15*(1), 1–23. https://doi.org/10.1016/j.rser.2010.07.014
3. Jacobs, M. (2016, March). High pressure for low emissions: How civil society created the Paris climate agreement. *Juncture*, *22*(4), 314–323. https://doi.org/10.1111/j.2050-5876.2016.00881.x
4. *How bad is 415 ppm of global atmospheric CO2 concentration? — Niklas Rosenberg*. (2021, August 10). How Bad Is 415 Ppm of Global Atmospheric CO2 Concentration? &Mdash; Niklas Rosenberg. https://niklasrosenberg.com/blog/2021/8/10/how-bad-is-415-ppm-of-global-atmospheric-co2-concentration; Date of access : 14th May 2023
5. Błaszczak, P., Łapiński, M., Wang, S. F., Jasiński, P., & Bochentyn, B. (2020, October). Exsolution of Ni nanoparticles on the surface of cerium and nickel co-doped lanthanum strontium titanate as a new anodic layer for DIR-SOFC. Anti-coking potential and H2S poisoning resistance of the prepared material. *International Journal of Hydrogen Energy*, *45*(53), 29186–29200. https://doi.org/10.1016/j.ijhydene.2020.07.162
6. De, S., Zhang, J., Luque, R., & Yan, N. (2016). Ni-based bimetallic heterogeneous catalysts for energy and environmental applications. *Energy & Environmental Science*, *9*(11), 3314–3347. https://doi.org/10.1039/c6ee02002j
7. Choudhury, A., Chandra, H., & Arora, A. (2013, April). Application of solid oxide fuel cell technology for power generation—A review. *Renewable and Sustainable Energy Reviews*, *20*, 430–442. https://doi.org/10.1016/j.rser.2012.11.031
8. McLarty, D., Brouwer, J., & Samuelsen, S. (2013, June 17). Hybrid Fuel Cell Gas Turbine System Design and Optimization. *Journal of Fuel Cell Science and Technology*, *10*(4). https://doi.org/10.1115/1.4024569
9. McIntosh, S., & Gorte, R. J. (2004, July 21). Direct Hydrocarbon Solid Oxide Fuel Cells. *Chemical Reviews*, *104*(10), 4845–4866. https://doi.org/10.1021/cr020725g
10. Stambouli, A., & Traversa, E. (2002, October). Solid oxide fuel cells (SOFCs): a review of an environmentally clean and efficient source of energy. *Renewable and Sustainable Energy Reviews*, *6*(5), 433–455. https://doi.org/10.1016/s1364-0321(02)00014-x
11. Cao, T., Kwon, O., Gorte, R. J., & Vohs, J. M. (2020, December 7). Metal Exsolution to Enhance the Catalytic Activity of Electrodes in Solid Oxide Fuel Cells. *Nanomaterials*, *10*(12), 2445. https://doi.org/10.3390/nano10122445
12. van Deelen, T. W., Hernández Mejía, C., & de Jong, K. P. (2019, November 4). Control of metal-support interactions in heterogeneous catalysts to enhance activity and selectivity. *Nature Catalysis*, *2*(11), 955–970. https://doi.org/10.1038/s41929-019-0364-x
13. Neagu, D., Oh, T. S., Miller, D. N., Ménard, H., Bukhari, S. M., Gamble, S. R., Gorte, R. J., Vohs, J. M., & Irvine, J. T. (2015, September 11). Nano-socketed nickel particles with enhanced coking resistance grown in situ by redox exsolution. *Nature Communications*, *6*(1). https://doi.org/10.1038/ncomms9120
14. Madsen, B., Kobsiriphat, W., Wang, Y., Marks, L., & Barnett, S. (2007, March). Nucleation of nanometer-scale electrocatalyst particles in solid oxide fuel cell anodes. *Journal of Power Sources*, *166*(1), 64–67. https://doi.org/10.1016/j.jpowsour.2006.12.080

15. Adijanto, L., Balaji Padmanabhan, V., Küngas, R., Gorte, R. J., & Vohs, J. M. (2012). Transition metal-doped rare earth vanadates: a regenerable catalytic material for SOFC anodes. *Journal of Materials Chemistry*, *22*(22), 11396. https://doi.org/10.1039/c2jm31774e
16. Adijanto, L., Sampath, A., Yu, A. S., Cargnello, M., Fornasiero, P., Gorte, R. J., & Vohs, J. M. (2013, July 18). Synthesis and Stability of Pd@CeO2 Core–Shell Catalyst Films in Solid Oxide Fuel Cell Anodes. *ACS Catalysis*, *3*(8), 1801–1809. https://doi.org/10.1021/cs4004112
17. Burnat, D., Kontic, R., Holzer, L., Steiger, P., Ferri, D., & Heel, A. (2016). Smart material concept: reversible microstructural self-regeneration for catalytic applications. *Journal of Materials Chemistry A*, *4*(30), 11939–11948. https://doi.org/10.1039/c6ta03417a
18. Zhang, J., Gao, M. R., & Luo, J. L. (2020, June 5). In Situ Exsolved Metal Nanoparticles: A Smart Approach for Optimization of Catalysts. *Chemistry of Materials*, *32*(13), 5424–5441. https://doi.org/10.1021/acs.chemmater.0c00721
19. Opitz, A. K., Nenning, A., Vonk, V., Volkov, S., Bertram, F., Summerer, H., Schwarz, S., Steiger-Thirsfeld, A., Bernardi, J., Stierle, A., & Fleig, J. (2020, September 23). Understanding electrochemical switchability of perovskite-type exsolution catalysts. *Nature Communications*, *11*(1). https://doi.org/10.1038/s41467-020-18563-w
20. Kan, W. H., & Thangadurai, V. (2014, December 18). Challenges and prospects of anodes for solid oxide fuel cells (SOFCs). *Ionics*, *21*(2), 301–318. https://doi.org/10.1007/s11581-014-1334-6
21. Kuo PJ, Lee CL, Wang JH, Hsieh SY, Huang SC, Lam CF. Inhalation of volatile anesthetics via a laryngeal mask is associated with lower incidence of intraoperative awareness in non-critically ill patients. PLoS One. 2017;12(10):e0186337. https://doi. org/10.1371/journal.pone.0186337. (2019, January 29). *AORN Journal*, *109*(2), 256–261. https://doi.org/10.1002/aorn.12603
22. Tang, C., Kousi, K., Neagu, D., & Metcalfe, I. S. (2021, February 24). Trends and Prospects of Bimetallic Exsolution. *Chemistry – a European Journal*, *27*(22), 6666–6675. https://doi.org/10.1002/chem.202004950
23. Oh, T. S., Rahani, E. K., Neagu, D., Irvine, J. T. S., Shenoy, V. B., Gorte, R. J., & Vohs, J. M. (2015, December 9). Evidence and Model for Strain-Driven Release of Metal Nanocatalysts from Perovskites during Exsolution. *The Journal of Physical Chemistry Letters*, *6*(24), 5106–5110. https://doi.org/10.1021/acs.jpclett.5b02292
24. Katz, M. B., Zhang, S., Duan, Y., Wang, H., Fang, M., Zhang, K., Li, B., Graham, G. W., & Pan, X. (2012, September). Reversible precipitation/dissolution of precious-metal clusters in perovskite-based catalyst materials: Bulk versus surface re-dispersion. *Journal of Catalysis*, *293*, 145–148. https://doi.org/10.1016/j.jcat.2012.06.017
25. Gao, Y., Chen, D., Saccoccio, M., Lu, Z., & Ciucci, F. (2016, September). From material design to mechanism study: Nanoscale Ni exsolution on a highly active A-site deficient anode material for solid oxide fuel cells. *Nano Energy*, *27*, 499–508. https://doi.org/10.1016/j.nanoen.2016.07.013
26. Lai, K. Y., & Manthiram, A. (2018, March 29). Evolution of Exsolved Nanoparticles on a Perovskite Oxide Surface during a Redox Process. *Chemistry of Materials*, *30*(8), 2838–2847. https://doi.org/10.1021/acs.chemmater.8b01029
27. Kim, J. K., Jo, Y. R., Kim, S., Koo, B., Kim, J. H., Kim, B. J., & Jung, W. (2020, April 28). Exceptional Tunability over Size and Density of Spontaneously Formed Nanoparticles via Nucleation Dynamics. *ACS Applied Materials & Interfaces*, *12*(21), 24039–24047. https://doi.org/10.1021/acsami.0c05215
28. Ma, J., Geng, Z., Jiang, Y., Hou, X., Ge, X., Wang, Z., Huang, K., Zhang, W., & Feng, S. (2021, February). Exsolution manipulated local surface cobalt/iron alloying and dealloying conversion in La0·95Fe0·8Co0·2O3 perovskite for oxygen evolution reaction. *Journal of Alloys and Compounds*, *854*, 157154. https://doi.org/10.1016/j.jallcom.2020.157154
29. Yu, N., Jiang, G., Liu, T., Chen, X., Miao, M., Zhang, Y., & Wang, Y. (2021). Understanding the A-site non-stoichiometry in perovskites: promotion of exsolution of metallic nanoparticles and the hydrogen oxidation reaction in solid oxide fuel cells. *Sustainable Energy & Fuels*, *5*(2), 401–411. https://doi.org/10.1039/d0se01280g

30. Jiang, Y., Geng, Z., Sun, Y., Wang, X., Huang, K., Cong, Y., Shi, F., Wang, Y., Zhang, W., & Feng, S. (2019, November 25). Highly Efficient B-Site Exsolution Assisted by Co Doping in Lanthanum Ferrite toward High-Performance Electrocatalysts for Oxygen Evolution and Oxygen Reduction. *ACS Sustainable Chemistry & Engineering*, *8*(1), 302–310. https://doi.org/10.1021/acssuschemeng.9b05344
31. Ge, X., Chan, S., Liu, Q., & Sun, Q. (2012, August 24). Solid Oxide Fuel Cell Anode Materials for Direct Hydrocarbon Utilization. *Advanced Energy Materials*, *2*(10), 1156–1181. https://doi.org/10.1002/aenm.201200342
32. Han, H., Park, J., Nam, S. Y., Kim, K. J., Choi, G. M., Parkin, S. S. P., Jang, H. M., & Irvine, J. T. S. (2019, April 1). Lattice strain-enhanced exsolution of nanoparticles in thin films. *Nature Communications*, *10*(1). https://doi.org/10.1038/s41467-019-09395-4
33. Neagu, D., Kyriakou, V., Roiban, I. L., Aouine, M., Tang, C., Caravaca, A., Kousi, K., Schreur-Piet, I., Metcalfe, I. S., Vernoux, P., van de Sanden, M. C. M., & Tsampas, M. N. (2019, October 21). In Situ Observation of Nanoparticle Exsolution from Perovskite Oxides: From Atomic Scale Mechanistic Insight to Nanostructure Tailoring. *ACS Nano*, *13*(11), 12996–13005. https://doi.org/10.1021/acsnano.9b05652
34. Neagu, D., Tsekouras, G., Miller, D. N., Ménard, H., & Irvine, J. T. S. (2013, October 6). In situ growth of nanoparticles through control of non-stoichiometry. *Nature Chemistry*, *5*(11), 916–923. https://doi.org/10.1038/nchem.1773
35. Sun, Y., Li, J., Zeng, Y., Amirkhiz, B. S., Wang, M., Behnamian, Y., & Luo, J. (2015). A-site deficient perovskite: the parent for in situ exsolution of highly active, regenerable nano-particles as SOFC anodes. *Journal of Materials Chemistry A*, *3*(20), 11048–11056. https://doi.org/10.1039/c5ta01733e
36. Jiang, G., Yan, F., Wan, S., Zhang, Y., & Yan, M. (2019). Microstructure evolution and kinetics of B-site nanoparticle exsolution from an A-site-deficient perovskite surface: a phase-field modeling and simulation study. *Physical Chemistry Chemical Physics*, *21*(21), 10902–10907. https://doi.org/10.1039/c8cp07883a
37. Mao, X., Foucher, A. C., Montini, T., Stach, E. A., Fornasiero, P., & Gorte, R. J. (2020, May 19). Epitaxial and Strong Support Interactions between Pt and LaFeO3 Films Stabilize Pt Dispersion. *Journal of the American Chemical Society*, *142*(23), 10373–10382. https://doi.org/10.1021/jacs.0c00138
38. Kishimoto, H., Horita, T., Yamaji, K., Brito, M. E., Xiong, Y. P., & Yokokawa, H. (2010). Sulfur Poisoning on SOFC Ni Anodes: Thermodynamic Analyses within Local Equilibrium Anode Reaction Model. *Journal of the Electrochemical Society*, *157*(6), B802. https://doi.org/10.1149/1.3362896
39. Ahmadpour, G., Samardak, A., Korochentsev, V., Osmushko, I., Samardak, V., Komissarov, A., Shtarev, D., Samardak, A., Ognev, A., & Nasirpouri, F. (2021, November). Microstructure, composition and magnetic properties of Nd-(Fe1-xCox)-B oxide magnetic particles synthesized by Pechini-type chemical method. *Advanced Powder Technology*, *32*(11), 3964–3979. https://doi.org/10.1016/j.apt.2021.08.040
40. *X-ray diffraction (XRD) | Anton Paar Wiki*. (n.d.). Anton Paar. https://wiki.anton-paar.com/en/x-ray-diffraction-xrd/
41. Kamli, K., & Hadef, Z. (2022, February 23). *Binary Semiconductors Thin Films Characterization for Solar Cells Applications*. Binary Semiconductors Thin Films Characterization for Solar Cells Applications | IntechOpen. https://doi.org/10.5772/intechopen.100513
42. *SEM/EDS | SEM/EDX — Electron Microscope — IXRF Systems*. (n.d.). SEM/EDS | SEM/EDX — Electron Microscope — IXRF Systems. https://www.ixrfsystems.com/sem-eds/
43. Burany, S. (2003, September 16). Scanning Electron Microscopy and X-Ray Microanalysis. J. Goldstein, D. Newbury, D. Joy, C, Lyman, P. Echlin, E. Lifshin, L. Sawyer, and J. Michael. Kluwer Academic, Plenum Publishers, New York; 2003, 688 pages (Hardback, $75.00) ISBN 0-306-47292-9. *Microscopy and Microanalysis*, *9*(5), 484–484. https://doi.org/10.1017/s1431927603030617
44. *Scanning Electron Microscopy - Nanoscience Instruments*. (n.d.). Nanoscience Instruments. https://www.nanoscience.com/techniques/scanning-electron-microscopy/

45. Singh, A. K. (2016). Experimental Methodologies for the Characterization of Nanoparticles. *Engineered Nanoparticles*, 125–170. https://doi.org/10.1016/b978-0-12-801406-6.00004-2
46. Lee, S., Rao, S. P., Moon, M. H., & Giddings, J. C. (1996, May 1). Determination of Mean Diameter and Particle Size Distribution of Acrylate Latex Using Flow Field-Flow Fractionation, Photon Correlation Spectroscopy, and Electron Microscopy. *Analytical Chemistry*, *68*(9), 1545–1549. https://doi.org/10.1021/ac9511814
47. Homma, Y. (2001). III–V Growth, In Situ Observation by Scanning Electron Microscopy of. *Encyclopedia of Materials: Science and Technology*, 3678–3681. https://doi.org/10.1016/b0-08-043152-6/00656-2
48. Li, J., Yu, Y., Yin, Y. M., Zhou, N., & Ma, Z. F. (2017, May). A novel high performance composite anode with in situ growth of Fe-Ni alloy nanoparticles for intermediate solid oxide fuel cells. *Electrochimica Acta*, *235*, 317–322. https://doi.org/10.1016/j.electacta.2017.03.103
49. Klein, J. M., Hénault, M., Roux, C., Bultel, Y., & Georges, S. (2009, August). Direct methane solid oxide fuel cell working by gradual internal steam reforming: Analysis of operation. *Journal of Power Sources*, *193*(1), 331–337. https://doi.org/10.1016/j.jpowsour.2008.11.122
50. Gür, T. M. (2016, May). Comprehensive review of methane conversion in solid oxide fuel cells: Prospects for efficient electricity generation from natural gas. *Progress in Energy and Combustion Science*, *54*, 1–64. https://doi.org/10.1016/j.pecs.2015.10.004
51. Greeley, J., & Mavrikakis, M. (2004, October 17). Alloy catalysts designed from first principles. *Nature Materials*, *3*(11), 810–815. https://doi.org/10.1038/nmat1223
52. Chueh, W. C., & Haile, S. M. (2009). Electrochemical studies of capacitance in cerium oxide thin films and its relationship to anionic and electronic defect densities. *Physical Chemistry Chemical Physics*, *11*(37), 8144. https://doi.org/10.1039/b910903j
53. Lv, H., Lin, L., Zhang, X., Song, Y., Matsumoto, H., Zeng, C., Ta, N., Liu, W., Gao, D., Wang, G., & Bao, X. (2020, January). In Situ Investigation of Reversible Exsolution/Dissolution of CoFe Alloy Nanoparticles in a Co-Doped Sr2Fe1.5Mo0.5O6−δ Cathode for CO2 Electrolysis. *Advanced Materials*, *32*(6). https://doi.org/10.1002/adma.201906193
54. Chen, L., Xu, J., Wang, X., & Xie, K. (2020, April). Sr2Fe1.5+xMo0.5O6-δ cathode with exsolved Fe nanoparticles for enhanced CO2 electrolysis. *International Journal of Hydrogen Energy*, *45*(21), 11901–11907. https://doi.org/10.1016/j.ijhydene.2020.02.140
55. Sun, Y., Li, J., Zeng, Y., Amirkhiz, B. S., Wang, M., Behnamian, Y., & Luo, J. (2015). A-site deficient perovskite: the parent for in situ exsolution of highly active, regenerable nano-particles as SOFC anodes. *Journal of Materials Chemistry A*, *3*(20), 11048–11056. https://doi.org/10.1039/c5ta01733e
56. Zhu, T., Troiani, H., Mogni, L. V., Santaya, M., Han, M., & Barnett, S. A. (2019, November). Exsolution and electrochemistry in perovskite solid oxide fuel cell anodes: Role of stoichiometry in Sr(Ti,Fe,Ni)O3. *Journal of Power Sources*, *439*, 227077. https://doi.org/10.1016/j.jpowsour.2019.227077
57. Bäurer, M., Kungl, H., & Hoffmann, M. J. (2009, March). Influence of Sr/Ti Stoichiometry on the Densification Behavior of Strontium Titanate. *Journal of the American Ceramic Society*, *92*(3), 601–606. https://doi.org/10.1111/j.1551-2916.2008.02920.x
58. Yeh, Y. M., Tu, G., & Fang, T. H. (2004, June). Nanomechanical properties of nanocrystalline Ni–Fe mold insert. *Journal of Alloys and Compounds*, *372*(1–2), 224–230. https://doi.org/10.1016/j.jallcom.2003.08.101
59. Poth, P. (2004, September). Corrosion Books: The Iron Oxides– Structure, Properties, Reactions, Occurences and Uses. By: R. M. Cornell, U. Schwertmann. *Materials and Corrosion*, *55*(9), 704–704. https://doi.org/10.1002/maco.200490083
60. Chen, J., Wu, X., & Selloni, A. (2011, June 20). Electronic structure and bonding properties of cobalt oxide in the spinel structure. *Physical Review B*, *83*(24). https://doi.org/10.1103/physrevb.83.245204

61. Papargyriou, D., Miller, D. N., & Sirr Irvine, J. T. (2019). Exsolution of Fe–Ni alloy nanoparticles from (La,Sr)(Cr,Fe,Ni)O3 perovskites as potential oxygen transport membrane catalysts for methane reforming. *Journal of Materials Chemistry A*, *7*(26), 15812–15822. https://doi.org/10.1039/c9ta03711j
62. Tian, Y., Zheng, H., Zhang, L., Chi, B., Pu, J., & Li, J. (2018). Direct Electrolysis of CO2in Symmetrical Solid Oxide Electrolysis Cell Based on La0.6Sr0.4Fe0.8Ni0.2O3-δElectrode. *Journal of the Electrochemical Society*, *165*(2), F17–F23. https://doi.org/10.1149/2.0351802jes
63. Shah, S., Sayono, S., Ynzunza, J., Pan, R., Xu, M., Pan, X., & Gilliard-AbdulAziz, K. L. (2020, October 14). The effects of stoichiometry on the properties of exsolved Ni-Fe alloy nanoparticles for dry methane reforming. *AIChE Journal*, *66*(12). https://doi.org/10.1002/aic.17078
64. Shao, K., Li, F., Zhang, G., Zhang, Q., Maliutina, K., & Fan, L. (2019, July 10). Approaching Durable Single-Layer Fuel Cells: Promotion of Electroactivity and Charge Separation via Nanoalloy Redox Exsolution. *ACS Applied Materials & Interfaces*, *11*(31), 27924–27933. https://doi.org/10.1021/acsami.9b08448
65. Sun, Z., Fan, W., Bai, Y., Wu, K., & Cheng, Y. (2021, June 17). Tailoring Electrochemical Performance of Perovskite Anodes through In Situ Exsolution of Nanocatalysts. *ACS Applied Materials & Interfaces*, *13*(25), 29755–29763. https://doi.org/10.1021/acsami.1c08396
66. Zhu, T., Chen, X., Ni, W., Zhong, Q., & Han, M. (2019, November). Structural and electrochemical property evolutions of perovskite SOFC anodes: Role of fuel atmosphere in (La0.4Sr0.6)1-Co0.2Fe0.7Nb0.1O3-δ. *International Journal of Hydrogen Energy*, *44*(59), 31386–31393. https://doi.org/10.1016/j.ijhydene.2019.09.223
67. Lai, K. Y., & Manthiram, A. (2018, March 29). Self-Regenerating Co–Fe Nanoparticles on Perovskite Oxides as a Hydrocarbon Fuel Oxidation Catalyst in Solid Oxide Fuel Cells. *Chemistry of Materials*, *30*(8), 2515–2525. https://doi.org/10.1021/acs.chemmater.7b04569
68. Thommy, L., Joubert, O., Hamon, J., & Caldes, M. T. (2016, August). Impregnation versus exsolution: Using metal catalysts to improve electrocatalytic properties of LSCM-based anodes operating at 600 °C. *International Journal of Hydrogen Energy*, *41*(32), 14207–14216. https://doi.org/10.1016/j.ijhydene.2016.06.088
69. Kobsiriphat, W., Madsen, B. D., Wang, Y., Shah, M., Marks, L. D., & Barnett, S. A. (2010). Nickel- and Ruthenium-Doped Lanthanum Chromite Anodes: Effects of Nanoscale Metal Precipitation on Solid Oxide Fuel Cell Performance. *Journal of the Electrochemical Society*, *157*(2), B279. https://doi.org/10.1149/1.3269993
70. Ohnuma, I., Enoki, H., Ikeda, O., Kainuma, R., Ohtani, H., Sundman, B., & Ishida, K. (2002, January). Phase equilibria in the Fe–Co binary system. *Acta Materialia*, *50*(2), 379–393. https://doi.org/10.1016/s1359-6454(01)00337-8
71. Tai, L. W., & Lessing, P. A. (1992, February). Modified resin–intermediate processing of perovskite powders: Part I. Optimization of polymeric precursors. *Journal of Materials Research*, *7*(2), 502–510. https://doi.org/10.1557/jmr.1992.0502
72. Quinelato, A., Longo, E., Perazolli, L. A., & Varela, J. A. (2000, July). Effect of ceria content on the sintering of ZrO2 based ceramics synthesized from a polymeric precursor. *Journal of the European Ceramic Society*, *20*(8), 1077–1084. https://doi.org/10.1016/s0955-2219(99)00269-1
73. Horlick, S. A., Huang, Y. L., Robinson, I. A., & Wachsman, E. D. (2021, September). Controlling exsolution with a charge-balanced doping approach. *Nano Energy*, *87*, 106193. https://doi.org/10.1016/j.nanoen.2021.106193
74. Lee, J. G., Myung, J., Naden, A. B., Jeon, O. S., Shul, Y. G., & Irvine, J. T. S. (2020, March). Perovskites: Replacement of Ca by Ni in a Perovskite Titanate to Yield a Novel Perovskite Exsolution Architecture for Oxygen-Evolution Reactions (Adv. Energy Mater. 10/2020). *Advanced Energy Materials*, *10*(10). https://doi.org/10.1002/aenm.202070044
75. Yund, R. A., & McCallister, R. H. (1970). Kinetics and mechanisms of exsolution. *Chemical Geology*, *6*, 5–30. https://doi.org/10.1016/0009-2541(70)90002-1

Appendix - I

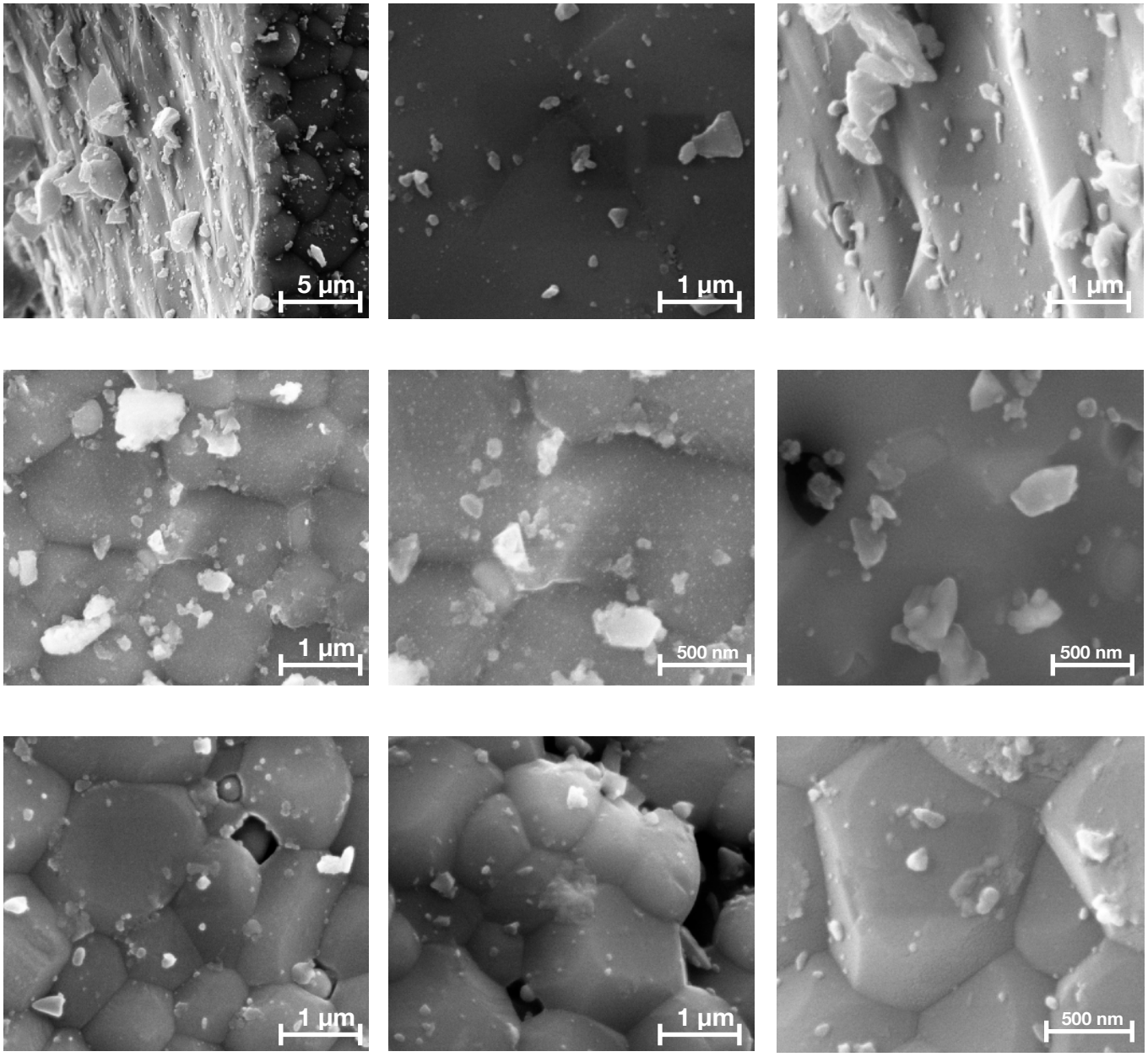

SEM images of LSCFeNiT with the exsolved nanoparticles at the surface after reduction in H_2 at 900 °C for 10 hour; Images were captured with different magnification scale and at different areas

Appendix - II

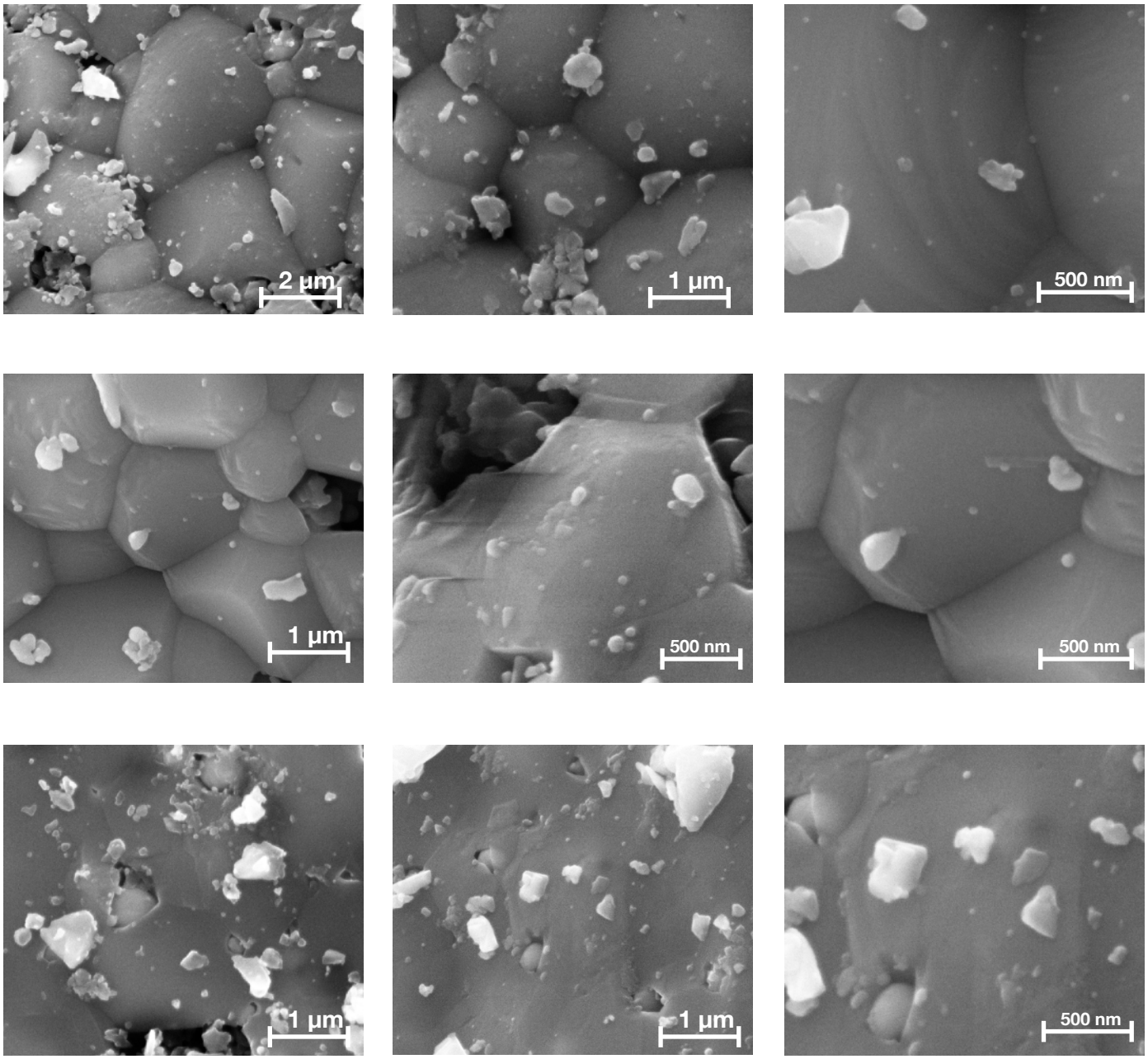

SEM images of LSCFeCoT with the exsolved nanoparticles at the surface after reduction in H_2 at 900 °C for 10 hour; Images were captured with different magnification scale and at different areas